R & D of a High-Aaverage-Power Fabry-Pérot resonator for Thomson scattering experiments

Xing Liu

NNT : 2018SACLS532

Thèse de doctorat

R & D of a High-Average-Power Fabry-Pérot Resonator for Thomson Scattering Experiments

Thèse de doctorat de Tsinghua University et
de l'Université Paris-Saclay
préparée à l'Université Paris-Sud

École doctorale n°576 : particules hadrons énergie et noyau : instrumentation, image, cosmos et simulation (Pheniics)
Spécialité de doctorat : Physique des accélérateurs

Thèse présentée et soutenue à l'Université de Tsinghua
à Pekin, le 5 Decembre 2018, par

Xing LIU

Composition du Jury :

Kexin LIU Professeur, Université de Pekin	Président & Rapporteur
Wenhui HUANG Professeur, Université de Tsinghua	Rapporteur
Guoxi PEI Professeur, Institut de Physique des Hautes Energies, Académie Chinoise des Sciences	Examinateur
David ROS Professeur, Université de Paris-Sud	Examinateur
Wei LU Professeur, Université de Tsinghua	Examinateur
Fabian ZOMER Professeur, Université de Paris-Sud	Directeur de thèse
Chuanxiang TANG Professeur, Université de Tsinghua	Co-Directeur de thèse

用于汤姆逊散射的高平均功率光学增益腔的研究

（申请清华大学和巴黎萨克雷大学
工学博士学位论文）

培 养 单 位 ： 工 程 物 理 系

学　　科 ： 核 科 学 与 核 技 术

研 究 生 ： 柳　　兴

指 导 教 师 ： 唐 传 祥 教 授

联 合 导 师 ： Fabian ZOMER 教 授

二〇一八年十一月

R & D of a High-Average-Power Fabry-Pérot Resonator for Thomson Scattering Experiments

Dissertation Submitted to

Tsinghua University & University of Paris-Saclay

in partial fulfillment of the requirement

for the degree of

Doctor of Philosophy

in

Nuclear Science and Technology

by

LIU Xing

Dissertation Supervisor : Professor TANG Chuanxiang

Joint Supervisor : Professor Fabian ZOMER

November, 2018

摘 要

如今，X射线在固体物理、医学领域以及其他学科中被广泛地使用。激光电子相互作用X射线源，也就是汤姆逊散射源，常常被用于产生高品质高性能的X射线。这种基于电子储存环和光学增益腔的X射线源造价相对低廉、紧凑。光腔的主要作用是放大入射激光的功率和循环激光脉冲，用于和电子碰撞的极小的束腰也可以由光腔来产生。在光腔内的激光脉冲与电子储存环中的高能电子束团碰撞产生准连续的X射线，产额可以达到10^{11} ph/s。

为了深入研究高功率光学增益腔的物理问题，我们主要做了如下工作：首先，建立了一个精确的考虑载波包络相位和时间失谐因素的光腔存储瞬态模型。基于此模型，我们分析了具有相同能量增益系数的光腔：有较高精细度却存在时间失谐的光腔，比起无失谐、较低精细度的光腔，具有更宽的线宽。这说明着把激光器锁到前者光腔上相对更容易。其次，为了解释我们在非平面四镜光腔上观测到的*S*形状光模，我们首次推导出了一般像散光束的非傍轴矫正项的解析解，并定性地解释了实验中的现象。最后，通过利用Winkler的热变形模型，我们发现光腔的能量增益对镜子的形变极其敏感，能量增益因子降低一半所对应的腔镜形变量与其精细度的平方成反比。

基于正在建造的ThomX项目的原型腔，我们提出了一种新的激光稳频方法，该方法利用光腔的极化特性和腔镜对不同极化光的反射相位相异来产生误差信号。比起传统PDH方法，该技术相对简单，无需对激光进行调制解调，并且可以控制腔内激光的极化。同时，我们进行了光腔的高功率实验。实验环境要求极高的洁净度，镜面上任何灰尘会极大地降低光腔的精细度，通过四种不同的方法，我们测得该光腔的精细度高达26,000，能量增益约为10,000。而且我们观测到了高功率光腔的模式不稳定现象，这可能由于光腔模式退化造成。最终存储在光腔的能量稳定在383 kW。

在某些X射线应用中，基于环和光腔的高重频的X射线源更受欢迎，这亦是清华加速器实验室下一步计划，目前原型腔的设计已完成。

总之，由电子储存环和光学增益腔构成的紧凑型汤姆逊散射源可以产生高产额、高质量的X射线，并且是非常有前途的。

关键词：光学增益腔;极化锁;汤姆逊散射;高功率光腔;热效应

Abstract

At present, X-rays are widely applied in solid-state physics, in the life sciences, in medical applications and in other disciplines. An X-ray source based on laser-electron interaction, that is, a Thomson scattering X-ray source, can be used to produce high-quality X-rays at a low cost and with a small-sized apparatus. The construction of compact laser-electron sources, each consisting of an electron storage ring and an optical enhancement cavity, has recently attracted the interest of many institutions. The optical enhancement cavity is mainly used to amplify the injected power, circulate the pulses at a high repetition frequency ($\sim$ tens of megahertz) and produce a beam with a small waist at the interaction point. When introduced into the electron storage ring, the laser pulses produced in the high-average-power cavity scatter off high-energy electrons at a high repetition frequency. Thus, a high X-ray flux of more than 10^{11} ph/s can be obtained.

In order to study the physical process inside a high-power resonator, main work has been done as follows. As a first step, we establish a precise transient model of the laser pulse stacking technique considering the CEP (carrier-envelope phase) effect and time detuning. The results of this model in the time and frequency domains match very well. A cavity with a given finesse and no detuning has a narrower linewidth than a detuned cavity with a higher finesse if both cavities have the same gain; consequently, it is easier to lock a laser to the latter cavity. Next, for the first time, we derived the non-paraxial corrections for general astigmatic beams so as to explain the *S*-shaped cavity mode observed in a non-planar four-mirror cavity. We solved Lax perturbation series of the wave equation for general elliptic Gaussian beams and *S*-shaped beam modes appear as the beam propagates away from the cavity symmetry point. This feature agrees qualitatively with observations made on a highly divergent non-planar four-mirror cavity. In addition, we study the thermal effect by using Winkler's deformation model. The cavity gain is very sensitive to the mirror deformation in open loop. A strong feedback and ultra-low expansion mirrors are indispensable to have a high power stored in the cavity.

Several significative experiments were performed on the prototype cavity for ThomX. Firstly, we proposed a new frequency stabilization method based on the polarization of a folded cavity and tuning of the cavity mirror reflectivity. Sufficient s- and p-wave phase detuning can be obtained by special design of the cavity mirrors' coatings, which give

rise to an error signal that can be used for locking. Compared to the traditional PDH method, this technique is simpler without need for frequency modulation and demodulation. Theoretical calculations and experimental results demonstrate the feasibility of the proposed method. Meanwhile, high-power experiments on the prototype S-Box cavity for ThomX were demonstrated. A cavity finesse of approximately 26,000 is measured using four different methods, and the deposition of dust on the cavity mirrors is found to have an enormous effect on the finesse. We achieve a stable power as high as 383 kW with a cavity gain of 10,000. In addition, modal instabilities which limits this power were observed. We believe that this effect originates from cavity modal frequency degeneracy induced by thermal effect.

Tsinghua University hosts a compact, low-repetition-frequency X-ray source known as TTX, which is based on a linac system and a terawatt femtosecond laser system. The next step is to upgrade TTX to a high-repetition-frequency X-ray machine called TTX2, consisting of an optical cavity and an electron storage ring. We present the complete design of a prototype optical cavity for TTX2.

In summary, a Thomson scattering X-ray source composed of an electron storage ring and an optical cavity can produce a high flux of high-quality X-rays and is very promising as a compact source.

Key words: Optical cavity; Polarization lock; Thomson scattering; High-average-power resonator; Thermal effect

Contents

Chapter 1 Introduction

X-rays were discovered by a German physicist named Wilhelm Röntgen in 1895[1]. At present, X-rays play an extremely important role in various fields. Because of their short wavelengths, X-rays can react directly with atomic nuclei and atomic electrons. For research in the natural sciences, X-rays are often used as probes to study the structures of materials and their dynamic changes. X-ray techniques are becoming increasingly indispensable for characterizing material structures and studying ultra-fast physical processes at the atomic level. X-rays have a wide range of applications not only in solid-state physics but also in the life sciences, in medical applications and in other disciplines. In addition, ultra-short-pulse X-ray sources also have important application prospects in photochemistry, atomic and molecular physics, plasma physics, surface physics, nanomaterials science, tribology, environmental science and other disciplines.

In this chapter, several types of X-ray sources are briefly introduced along with the inverse Compton scattering process. In addition, overviews of the ThomX project and TTX (Tsinghua Thomson Scattering X-ray Source) are presented.

1.1 Background and Motivation

Over the last century, X-ray sources have facilitated countless important scientific discoveries. In particular, more than a dozen of Nobel Prizes have been awarded for work related to X-rays[2,3].

Physicists are constantly searching for diverse X-ray sources of high quality and high brilliance to meet the needs of various applications. To date, several types of high-performance sources have been developed, including synchrotron radiation sources, free-electron lasers and inverse Compton scattering sources. As shown in Figure 1.1[4], the brightness of X-ray sources has been significantly improved—by 13 orders of magnitude—over the past century. The characteristics of these different types of sources will be introduced and compared in the following subsections.

1.1.1 X-ray Tubes

The most widely used conventional X-ray source is an X-ray tube, which can convert electric power into X-rays in vacuum. The electrons emitted from a hot cathode are

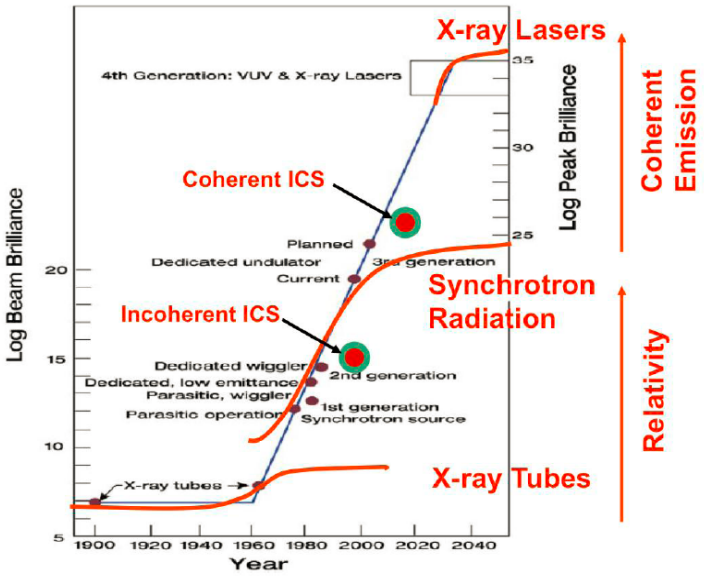

Figure 1.1 The history of X-ray sources[4].

accelerated by a high voltage and impinge on a metal target, resulting in the production of X-rays. However, the conversion efficiency between the kinetic energy of the striking electrons and the resulting X-rays is less than 1%[5]. X-ray tubes generate both characteristic and continuous X-ray radiation.

When a high-speed electron collides with an atom, it results in the dislocation of a bound inner-shell electron. As shown in Figure 1.2(a), another electron from the outer shell fills in the empty space, leading to the emission of a characteristic X-ray[6]. At the same time, when an electron is very close to the nucleus of an atom, it is consequently traveling through a strong electric field, and continuous X-rays are produced, as shown in Figure 1.2(b). To produce more continuous radiation, a heavy target material, such as Cr, Cu, Mo, Ag or W,[7] and a high applied voltage are usually needed.

Although X-ray tubes are cheap, compact and nearly isotropic sources, their drawbacks are very evident. The radiation is not monochromatic, and the flux and conversion efficiency are low. Moreover, these sources offer poor flexibility in manipulating the X-ray spectrum[5].

1.1.2 Synchrotron Radiation (SR) Sources

With the advent of well-known and widely used synchrotron radiation (SR) sources, circa 1960 in Figure 1.1, an enormous jump in brightness was achieved. In a third-generation SR source, the electron energy in the storage ring can reach as high as several

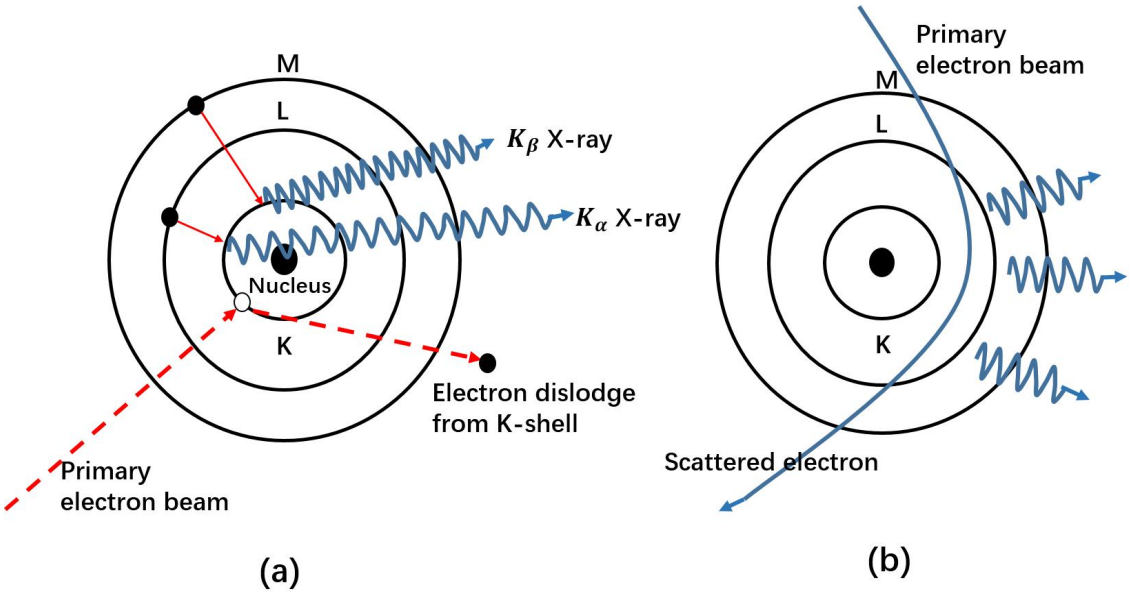

Figure 1.2 (a) Characteristic X-rays. (b) Continuous X-rays.

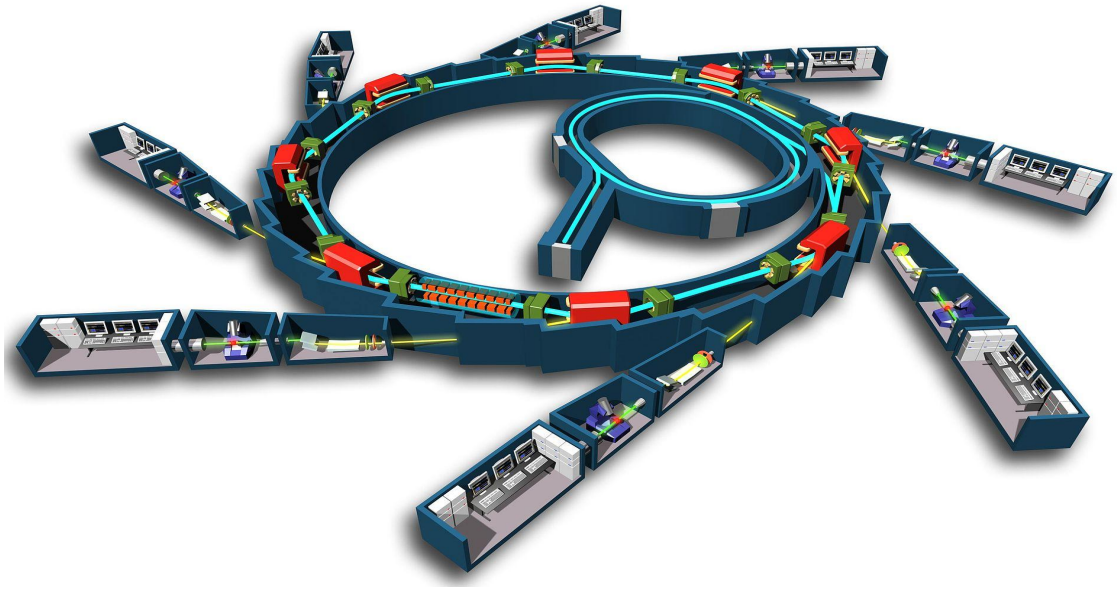

Figure 1.3 Diagram of the SOLEIL synchrotron facility[8].

gigaelectronvolts (GeV). The storage ring consists of bending magnets and straight sections serving as insertion devices (undulators or wigglers). The parameters of the generated radiation are determined by the electron beam energy and the insertion device parameters. The X-ray pulses generated by SR sources are usually hundreds of picoseconds in length, the same as the travel time of the electron beam in the storage ring. Table 1.1 lists the parameters of several typical SR sources. The SOLEIL synchrotron facility, located near Paris, France, is depicted in Figure 1.3[8].

Table 1.1 Parameters of several SR sources[13]

	Electron Energy	Pulse Duration	X-ray Energy
ALS	1.9 GeV	35-70 ps	0.23-1.8 keV
APS	7.0 GeV	100 ps	3.5-38 keV
ESRF	6.04 GeV	70 ps	2.6-22 keV
SPring-8	8.0 GeV	120 ps	4.7-51 keV

At present, there are approximately 50 operating SR sources in the world, including ALS (Advanced Light Source)[9], APS (Advanced Photon Source)[10], ESRF (European Synchrotron Radiation Facility)[11], and SPring-8 (Super Photon Ring 8 GeV)[12]. A single SR source is enormous and costly to construct; at the same time, the X-ray energies generated via SR are somewhat low, with a typical upper limit of approximately 10-50 keV, which somewhat limits the application of such SR sources.

1.1.3 Free-Electron Lasers (FELs)

The X-ray free-electron laser (FEL), which is based on a linear accelerator, is recognized as the fourth generation of X-ray sources. It was invented by John Madey[14] and soon afterward was successfully demonstrated in practice at Stanford University in 1977[15]. This type of X-ray source uses a linac to accelerate high-quality electron beams to above 10 GeV. Ultra-short femtosecond X-ray pulses can be generated by an FEL operating in SASE (self-amplified spontaneous emission) mode[16]. The electron beams interact with the undulator, as shown in Figure 1.4, to produce high-intensity X-ray pulses with a peak brightness that is 10 orders of magnitude higher than that of third-generation SR sources. To realize the implementation of fourth-generation X-ray sources, great progress has been made in FEL and accelerator technologies over the past ten years[17–19]. Due to these advances, several FEL projects have been proposed or are under construction, such as LCLS (Linac Coherent Light Source)[20], TESLA XFEL[21], the SPring-8 Compact SASE Source[22], and the European XFEL[23]. The parameters of the FLASH apparatus at DESY and the European XFEL, which is under construction, are given in Table 1.2[5].

However, similar to third-generation SR sources, devices of this type require enormous capital to construct and have high infrastructure costs, thus limiting the number of facilities that can be constructed and their applications.

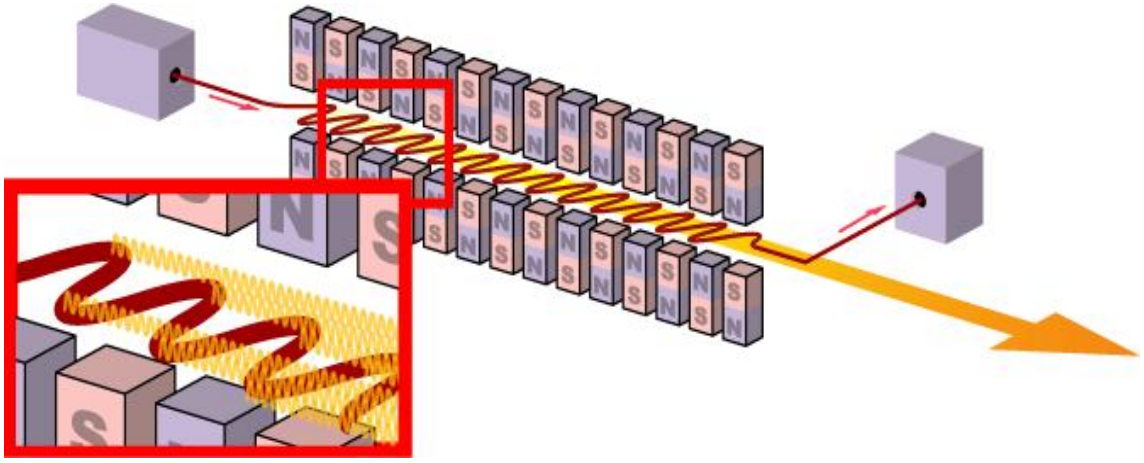

Figure 1.4 Schematic illustration of an undulator, the core of an FEL.

Table 1.2 Parameters of existing FLASH and XFEL installations

Facility	FLASH	European XFEL
X-ray range	50-6.5 nm	0.1 nm
Electron energy	730 MeV	17.5 GeV
Bunch charge	1 nC	1 nC
Bunch duration	400 fs	88 fs
Repetition rate	10 Hz	10 Hz
Emittance	2 mm*mrad	1.4 mm*mrad
Beam pulse current	5 mA	5 mA

1.1.4 Inverse Compton Scattering (ICS) Sources

Even great improvements in X-ray quality and brightness do not necessarily translate into greater access or productivity for individual researchers. X-rays are essential tools in many fields of fundamental applied research at universities and in both industrial and academic laboratories. However, even the cost of a single conventional synchrotron far exceeds the typical budget of a mid-size university or laboratory. The European Commission is aware of this problem and the consequent necessity to *develop bright but small and (relatively) cheap X-ray sources, not to replace synchrotrons but to complement them*[24]. A compact, room-sized apparatus based on laser-electron interaction, which is the main research subject of this doctoral dissertation, has the most potential to bridge the gap between conventional X-ray sources and synchrotrons or FELs and thus to lower the barrier to entry for X-ray-based research.

The study of inverse or backward Compton scattering (ICS) between relativistic

electrons and photons began in the 1940s. During his studies on the energy attenuation of interstellar high-energy electrons[25], Feenberg found that high-energy electrons exhibit a strong capability to shift the frequency of scattered photons. With the advent of lasers in 1960, Milburn proposed a conceptual model for the production of high-energy photons based on collisions between a laser beam and relativistic electrons[26], and in the same year, his idea was experimentally verified[27].

Compared with conventional X-ray sources, ICS sources are expected to produce X-rays of better quality and higher brightness, but these sources are more compact and lower in cost than SR sources and FELs. Many advantages can be realized through laser-electron interaction, such as more compact and lower-cost machines, quasi-monochromatic X-rays (with proper selection of the scattering angles), good beam directionality and energy tunability.

1.1.5 Applications of X-rays

Currently, X-rays are widely used in various fields. X-rays of different energies are used for different purposes. High-energy X-rays (above 10 MeV) can be used in Compton polarimeters[28], γ-γ colliders[29], laser wires[30] and polarized positron sources[31]. X-rays of approximately 1 MeV are mainly used in nuclear waste management and nuclear surveys. Low-energy X-rays (10-100 keV) play a crucial role in medicine, cultural heritage preservation, crystallography, and materials science, among other fields. Here, a brief summary of X-ray applications will be presented, with a focus on medical imaging and therapeutic technologies.

X-rays showed great potential for use in medicine immediately upon their discovery by Wilhelm Röntgen in 1895. Soon after the image of Mrs. Röntgen's hand acquired using X-rays was widely covered by media outlets in many developed Western countries, the first clinical X-ray images were produced in 1896[32]. From that moment on, X-rays were ranked among the most important tools in medical imaging and therapy.

First, we must emphasize the difference between standard X-rays and monochromatic X-rays. Standard X-ray tubes emit all "colors" of X-rays. Low-energy photons contribute to the received dose, whereas high-energy photons contribute to scattering. The goal of sources with tunable energy is to eliminate both the lowest- and highest-energy photons, such that the remaining photons are within the most useful range of energies. Within that range, we can then further tune the X-rays to the energies best suited to the imaging or

therapeutic task at hand. In the following, several typical methods of medical imaging are discussed.

The traditional imaging method is called absorption contrast imaging[33]. The ways in which X-rays interact with different materials depend on the chemical compositions of those materials. The X-ray absorption and transmission characteristics differ for different substances. When an X-ray passes through a sample, the absorption effect causes the intensity to be attenuated. The absorption contrast imaging method relies on the disparate absorption capabilities of different materials to differentiate distinct components of the internal structure of a sample. Since the discovery of X-rays, this method has dominated the X-ray imaging field for more than 100 years, during which time it has been widely used in biomedical imaging and clinical diagnosis[34]. Today, absorption imaging technology is still highly developed and widely used, especially in angiography and in studies of bone and other high-density biological structures. This indispensable technology provides a reliable basis for research, clinical diagnosis, and biomedical imaging.

Through the collimation of SR, FEL or ICS light, researchers can easily generate suitable monochromatic X-rays with a high flux either at a single energy or within a very narrow wavelength band. The optimal X-ray energy, which is determined by the composition and size of the object of interest, can be selected, and beam hardening effects can be largely avoided[32]. The image contrast and quality achievable at a constant X-ray dose can be effectively improved. However, the inherent fuzziness of the imaging of soft tissue structures, such as blood vessels and tumors, has limited the development of this approach[35].

In addition to absorption contrast imaging, X-ray phase contrast imaging[36] is another important method. When X-rays pass through a sample, a phase variation is induced by the different X-ray propagation velocities in different media, resulting in a distribution of transmission intensity. The phase contrast imaging method relies on this phenomenon. It overcomes several disadvantages of the absorption contrast method and can be used to identify and clearly image the internal structures of samples consisting of soft biological tissues. For soft biological tissues, the cross section for phase transition is approximately 1000 times larger than that for absorption. However, with increasing atomic number, the difference between the phase shift and absorption cross sections gradually decreases, resulting in a weakening of the phase contrast effect. Imaging a biological sample using the X-ray phase contrast method not only greatly reduces the radiation damage to the

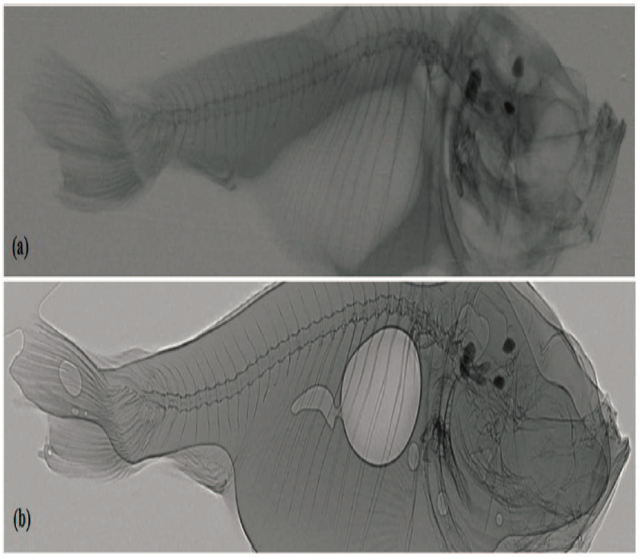

Figure 1.5 (a) Absorption contrast imaging. (b) Phase contrast imaging.[34]

sample[37] but also offers high sensitivity.

Figure 1.5[34] provides an intuitive illustration of the differences between the two methods. Compared with Figure 1.5(a), the phase contrast image in Figure 1.5(b) clearly reveals the internal structure of the small fish, even features of the soft tissue, such as bubbles.

Novel contrast mechanisms are emerging that are important for samples with very narrow angular acceptance[32]. A new method called diffraction-enhanced imaging has been proposed, in which image contrast is produced by means of the change in the direction of X-rays as they pass through an interface between different types of tissue within an object[38,39]. This method offers several advantages over absorption contrast imaging. The greatest is its ability to visualize miniature structures that lack sufficient mass to attenuate X-rays but can produce a refraction contrast at their interfaces. Unfortunately, because of the strict constraints on the wavelengths and angles of the X-rays, this method cannot be feasibly applied using conventional X-ray sources. When the density gradient of the sample is normal to the beam, the deviation of the beam will be the strongest. Hence, the refraction contrast imaging method is suitable for the study of soft tissues. There is hope that the contrast provided by the refraction information can enable the imaging of malignant tumors based on their morphological features.

In fact, diffraction-enhanced imaging is only one of many methods exploiting the possible sources of contrast offered by refraction or phase diffraction information[40].

Another important application of X-rays is radiation therapy. To date, many different kinds of ionizing radiation have played an important role in cancer therapy. For all techniques, the goal is to achieve the least possible absorbed dose in order to minimize the damage caused to the surrounding tissue when eliminating a tumor. Here, we will briefly introduce several approaches for enhancing the effectiveness of radiation therapy.

In 1995, an experimental radiosurgery technique called microbeam radiation therapy (MRT) was developed at NSLS (National Synchrotron Light Source) in the USA[41], and this method is now widely applied at ESRF (European Synchrotron Radiation Facility)[42,43]. In this method, multiple microscopically planar, parallel X-ray beams with energies of 50-150 keV are used to deliver the necessary radiation doses to irradiate tumors, especially brain tumors. There have been hundreds of cases of this technique in Europe. In another technique, called photon activation therapy, a cascade of photoelectrons and Auger electrons is generated in a tumor under irradiation with a monochromatic X-ray beam. This method consists of two steps. By tuning the X-ray energy, the photoabsorption in high-Z compounds in the tumor can be greatly enhanced to the K-absorption edge, followed by Auger de-excitation processes[44]. Recently, scientists have proposed a new radiation therapy technique in which an optimal dose can be delivered to a brain tumor with the help of a computerized tomographic scanner[45].

1.2 Inverse Compton Scattering

As discussed above in Section 1.1, ICS sources, namely, sources based on laser-electron interaction, are the most promising candidates to bridge the gap between conventional X-ray sources and advanced light sources (SR sources and FELs). In this section, the theoretical characteristics of ICS will be introduced.

1.2.1 Scattered Photon Energy

The collision between an electron and a photon is often described using the quantum theory of a two-particle elastic collision depicted in Figure 1.6. Figure 1.6 shows a schematic illustration of ICS in the electron rest frame. E_1^* is the energy of the incident photon, E_2^* is the energy of the scattered photon, θ^* is the collision angle, and the scattering angle is denoted by ϕ^*. In the following, the momenta of the electron and photon are denoted by P_{e1}^*, P_{e2}^*, $P_{\gamma 1}^*$, and $P_{\gamma 2}^*$, where the subscript 1 represents the initial state and the subscript 2 indicates the state after the collision. The four-momenta are expressed as

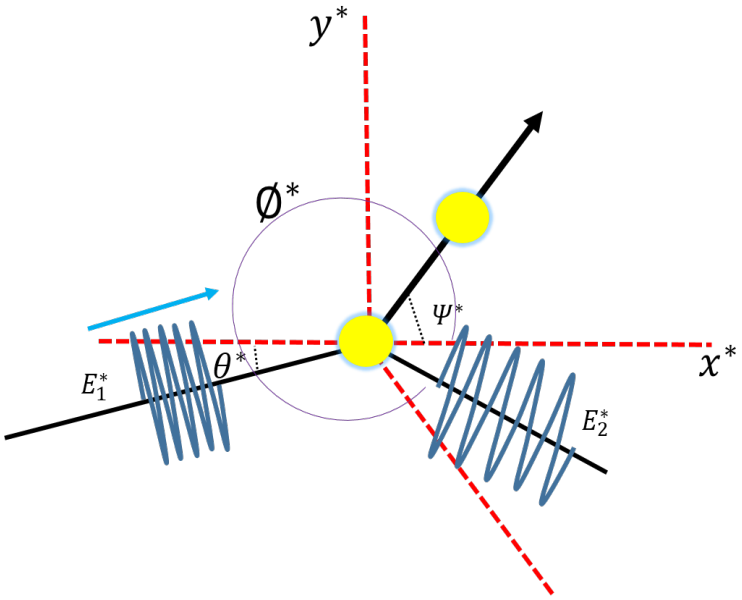

Figure 1.6 Schematic illustration of inverse Compton scattering in the electron rest frame.

follows:

$$
\begin{aligned}
P^*_{\gamma 1} &= \frac{E^*_1}{c}\begin{pmatrix} c \\ \cos\theta^* \\ \sin\theta^* \\ 0 \end{pmatrix} \qquad P^*_{e1} = \frac{mc^2}{c}\begin{pmatrix} c \\ 0 \\ 0 \\ 0 \end{pmatrix} \\
P^*_{\gamma 2} &= \frac{E^*_2}{c}\begin{pmatrix} c \\ \cos\theta^* \\ \sin\theta^* \\ 0 \end{pmatrix} \qquad P^*_{e1} = \frac{mc^2\gamma^*}{c}\begin{pmatrix} c \\ \beta^*\cos\psi^* \\ \beta^*\sin\psi^* \\ 0 \end{pmatrix}
\end{aligned}
\tag{1-1}
$$

On the basis of the momentum conservation law $P^*_{e1} + P^*_{\gamma 1} = P^*_{e2} + P^*_{\gamma 2}$, it is easy to obtain the energy of the scattered photon in the initial electron rest frame:

$$
E^*_2 = \frac{mc^2 E^*_1}{mc^2 + E^*_1[1 - \cos(\theta^* - \psi^*)]} \tag{1-2}
$$

Then, by applying the Lorentz transformation, the kinematic variables in the laboratory frame can be obtained from those in the electron rest frame. The Lorentz transfor-

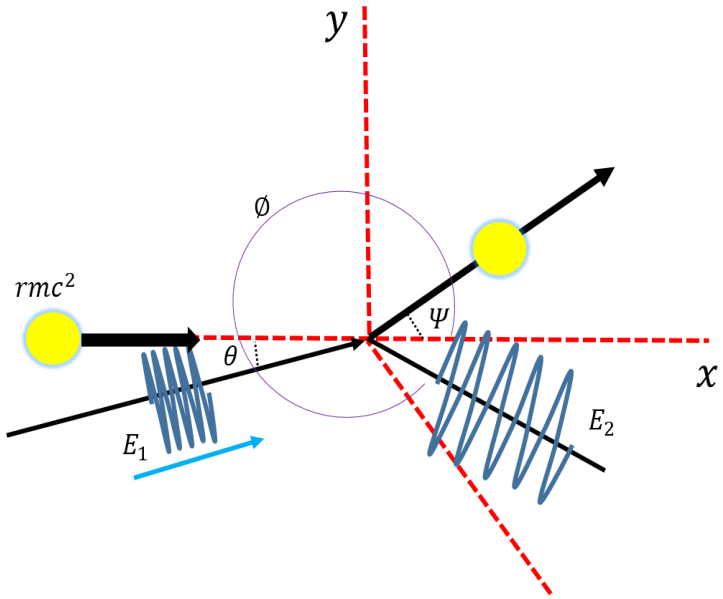

Figure 1.7 Schematic illustration of inverse Compton scattering in the laboratory frame.

mation can be expressed as follows:

$$
\begin{aligned}
E_1^* &= \gamma E_1(1-\beta\cos\theta) \\
E_2^* &= \gamma E_2(1-\beta\cos\phi) \\
\theta^* &= \begin{cases} \arcsin[\dfrac{\sin\theta}{\gamma(1-\beta\cos\theta)}] \\ \arccos(\dfrac{\beta+\cos\theta}{1-\beta\cos\theta}) \end{cases} \\
\phi^* &= \begin{cases} \arcsin[\dfrac{\sin\phi}{\gamma(1-\beta\cos\phi)}] \\ \arccos(\dfrac{\beta+\cos\phi}{1-\beta\cos\phi}) \end{cases}
\end{aligned}
\tag{1-3}
$$

where E_1 and E_2 are the energies of the incident and scattered photons, respectively, in the laboratory frame and θ and ϕ are the collision angle and the scattering angle, respectively, as shown in Figure 1.7. E_2 can be expressed as follows:

$$
E_2 = \frac{mc^2\gamma E_1(1-\beta\cos\theta)}{mc^2\gamma(1-\beta\cos\phi)+E_1[1-\cos(\theta-\phi)]} \tag{1-4}
$$

Now, for a head-on ($\theta = 180$ deg) laser-electron collision, the scattered photon will obtain its maximum energy of $4\gamma^2 E_1$ if $\phi = 0$ deg, meaning that the scattered photon returns in the opposite direction from that in which it came. Equation 1-5 describes this

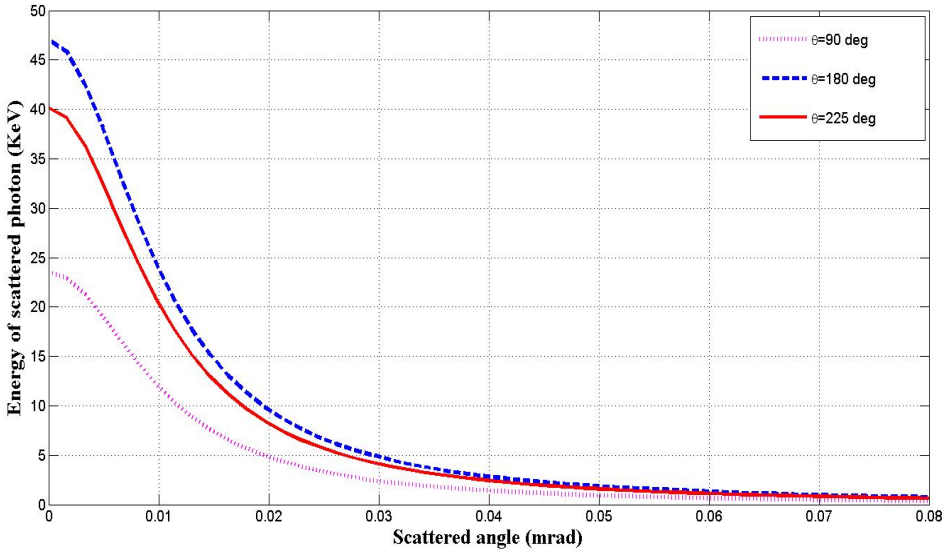

Figure 1.8 Scattered photon energy as a function of the scattering angle at collision angles of 90 deg, 180 deg and 225 deg. The incident electron energy is 50 MeV, and the laser wavelength is 1030 nm.

case:

$$E_{2max} = \frac{\gamma^2 E_1 (1+\beta)^2}{1 + \frac{4\gamma E_1}{mc^2}(1+\beta)} \sim 4\gamma^2 E_1 \tag{1-5}$$

Here, we assume that the electron energy is high (50 MeV) and that the laser wavelength is 1030 nm (E_1 = 1.2 eV), i.e., β~1 and γ~100. Then, the maximum energy of the scattered photon is 48 keV. As shown in Figure 1.8, the maximum energy is achieved at θ = 180 deg. Figure 1.8 shows the scattered photon energy as a function of the scattering angle. Figure 1.9 shows the relationship between the maximal energy of the scattered photon and the collision angle.

1.2.2 Differential Cross Section

The differential cross section for Thomson scattering in the electron rest frame can be expressed as follows[46]:

$$\frac{d\sigma}{d\Omega^*} = \frac{r_0^2}{2}\left(\frac{E_2^*}{E_1^*}\right)^2\left[\frac{E_1^*}{E_2^*} + \frac{E_2^*}{E_1^*} - \sin^2(\phi^* - \theta^*)\right] \tag{1-6}$$

where r_0 is the classical electron radius, $d\sigma$ is the differential scattering cross section, and $d\Omega$ is the spatial solid angle of the scattered photons. From a physical standpoint,

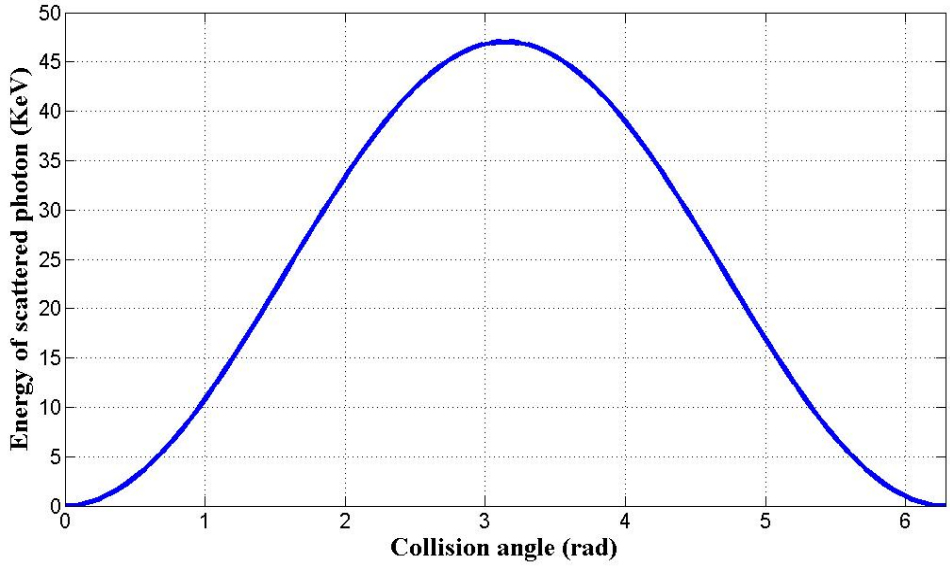

Figure 1.9 Maximal scattered photon energy as a function of the collision angle. The incident electron energy is 50 MeV, and the laser wavelength is 1030 nm.

$d\sigma$ allows to determine the probability that photons of energy E_1 will be converted into photons of energy E_2 with directions that lie within a spatial solid angle of $d\Omega$ after colliding with high-energy electrons.

Upon converting Equation 1-6 into the laboratory frame, we obtain the following expression:

$$\frac{d\sigma}{d\Omega} = \frac{d\sigma}{d\Omega^*}\frac{d\Omega^*}{d\Omega} = \frac{d\sigma}{d\Omega^*}\frac{\sin\phi^*}{\sin\phi}\frac{d\phi^*}{d\phi} = \frac{d\sigma}{d\Omega^*}\frac{1}{\gamma^2(1-\beta\cos\phi)^2} \tag{1-7}$$

1.2.3 X-ray Yield

The flux of scattered photons produced by laser-electron interactions can be analytically estimated as the product of the luminosity (L) and the Compton scattering cross section (σ):

$$N_x = \sigma \times L \tag{1-8}$$

Here, the total cross section σ can be obtained by integrating Equation 1-7: $\sigma = \frac{8\pi}{3}r_0^2 = 6.65 \times 10^{-29}$ m^2. The luminosity L is determined by the spatial distributions of the photons and electrons, the collision frequency and the collision angle. If the distributions of the laser pulse and the electron bunch are denoted by $\rho_l(x, y, z, t)$ and $\rho_e(x, y, z, t)$,

respectively, then the collision luminosity is given by[47]

$$L = 2cf_c N_e N_l \sin^2\theta \iiint \int_{-\infty}^{+\infty} \rho_e(x,y,z,t)\rho_l(x,y,z,t)dxdydzdt \tag{1-9}$$

where θ, f_c, N_l and N_e are the collision angle, the collision frequency, the number of photons in one pulse and the number of electrons in one bunch, respectively.

If the distributions of the laser pulse and the electron bunch are both three-dimensional Gaussian distributions and the widths of the beam are considered to be constant, then the luminosity can be expressed as follows[47]:

$$L = \frac{f_c N_l N_e \sin\theta}{2\pi} \frac{1}{\sqrt{\sigma_{Ve}^2 + \sigma_{Vl}^2}\sqrt{(\sigma_{He}^2 + \sigma_{Hl}^2)\sin^2\theta + (\sigma_{Le}^2 + \sigma_{Ll}^2)\cos^2\theta}} \tag{1-10}$$

where σ_{He}, σ_{Ve} and σ_{Le} denote the horizontal spread, vertical spread and pulse duration, respectively, of the electron bunch, whereas σ_{Hl}, σ_{Vl} and σ_{Ll} denote the same quantities for the laser pulse.

1.3 Overview of TTX and ThomX

As discussed in Sections 1.1 and 1.2, technological developments in fiber lasers, optical cavities, chirped pulse amplification and particle accelerators have made it possible to exploit the ICS process, in which a low-energy photon scatters off an electron circulating in a synchrotron machine, to generate X-rays. Through the resulting exchange of momenta, the energy of the photon can be increased by a factor of $4\gamma^2$, where γ is the Lorentz factor of the electron beam, shifting it into the X-ray regime.

The ICS X-ray source was first proposed by G.Matone from Frascati, Italy[48] in 1977 and was demonstrated soon in 1980[49]. So far, high flux γ rays $(3.5 \pm 0.3) \times 10^8$ ph/s has been obtained at ATF facility[50,51]

At present, there are two types of ICS X-ray sources: one is based on a terawatt laser system and a linac system, and the other relies on a laser optical enhancement cavity and an electron storage ring. Nowadays there are almost twenty Compton machines which are in operation or under development[52]. Detailed information about Compton machine status could be found in Table 1.5 of Reference[52]. To our best knowledge, nowadays there are several Thomson scattering sources based on an optical cavity and an electron storage ring. One project called MightyLaser[50] was unfortunately dismantled. ThomX

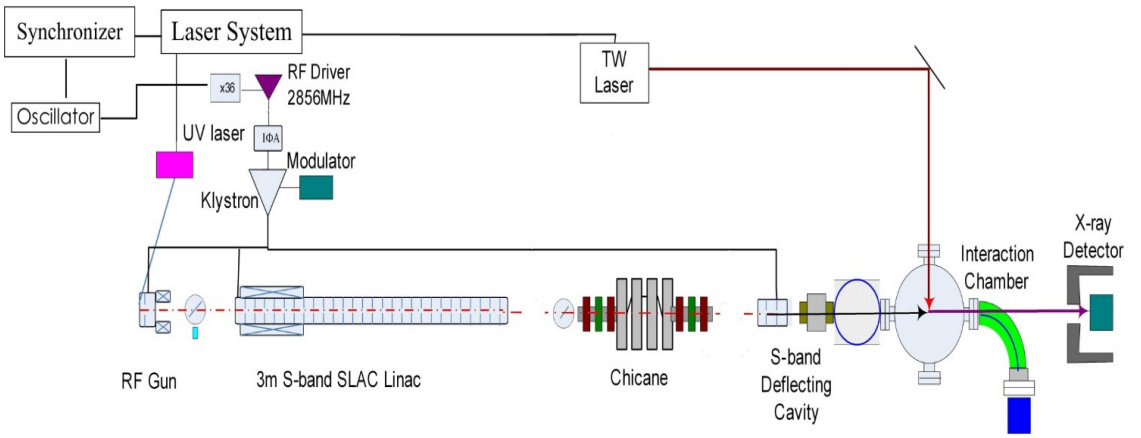

Figure 1.10 Schematic diagram of the layout of TTX.

project is funded and now under development, whose final goal of X-ray flux is as high as 10^{11-13} ph/s. Munich Compact Light Source[53] is in operation. The flux of 3×10^{10} ph/s has been obtained and the energy of X-ray is around 15-35 keV.

In the following subsections, two representative projects are briefly introduced.

1.3.1 TTX

TTX, short for the Tsinghua Thomson Scattering X-ray Source, is a typical linac-type Thomson source[54,55], consisting of a linac system and a terawatt femtosecond laser system. The linac system is made up of an S-band photocathode RF gun, a traveling wave tube and two X-band structures. High-quality, ultra-short electron pulses can be produced by using the linac system, as shown in Figure 1.10[54]. The low-repetition-frequency femtosecond laser system, whose peak power is in the terawatt range, produces laser pulses to collide with the electrons. The number of X-rays produced in experiments reaches 1.2×10^5 per collision after the removal of the backgrounds from beam dump and beam loss.

However, this machine must operate at a low repetition frequency because of the constraints of the high-peak-power laser system. In addition, the appearance of a nonlinear Compton effect[56] and the possible optical damage in the terawatt laser system also hinder the process of increasing the frequency. Nevertheless, for some applications, high-repetition-rate X-ray machines are preferred.

1.3.2 ThomX

ThomX is a French project funded by French government *Equipex* and the *Région Île-de-France* to create a compact source of X-rays for applications in the health sector and for cultural heritage investigations, among other purposes. The angular dependence of the energy of the X-ray beam makes it possible to select a desired X-ray energy range by blocking out the other angles with a diaphragm. By virtue of the sufficiently high initial laser power, an X-ray flux of $\sim 10^{11} - 10^{13}$ ph/s with a tunable energy of $45 - 90$ keV [57] will be achieved. These properties make ThomX a very attractive and cost-effective alternative to large synchrotron facilities, whose use is limited due to both their far-away locations and their limited beam time per user.

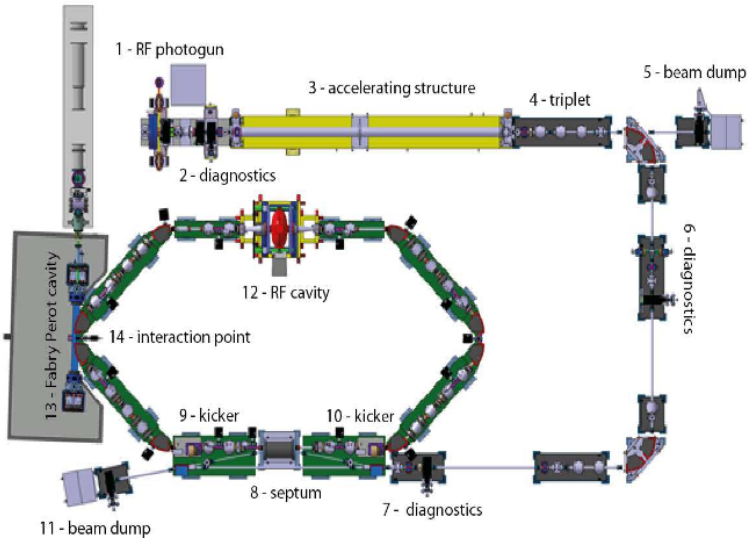

Figure 1.11 ThomX setup [57]. The electron beam is created in a photon gun, initially accelerated in a linear accelerator and then injected into a synchrotron storage ring using a kicker magnet. X-rays are produced at the interaction point between the high-power laser beam and the electron beam.

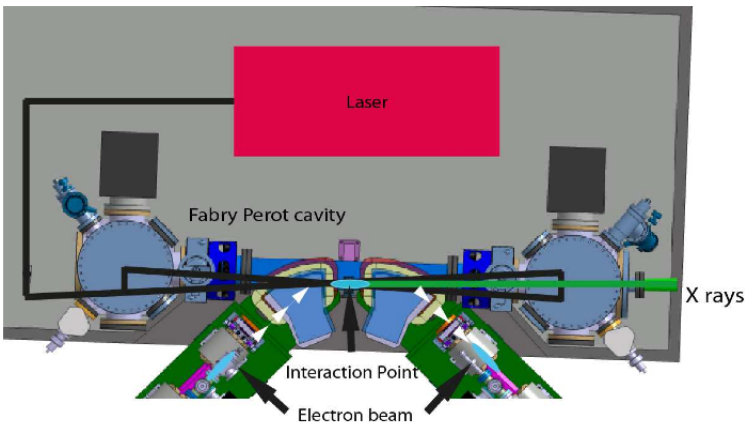

Figure 1.12 Interaction point between the high-power laser beam and the electron beam in the ThomX machine[57]. The laser beam is injected into the Fabry-Pérot cavity, where it accumulates, thus increasing its power. At the injection point, the laser beam is focused onto the passing electron beam, and an intense X-ray beam is produced via ICS and exits to the right, toward the experimental station.

The setup of the ThomX synchrotron machine is detailed in Figure 1.11, and the laser-electron interaction point can be seen in Figure 1.12. The ThomX ring circumference is 18 m long, with a revolution frequency of 16.7 MHz and a relatively low beam energy of 50 MeV[57]. For comparison with a conventional synchrotron light source, consider SOLEIL, which has a circumference of 354 m and a nominal beam energy of 2.75 GeV[8]. SOLEIL can deliver synchrotron light over a wide spectrum of 400 μeV – 100 keV[8], making it a very versatile instrument. At the same time, it has a very high brilliance (defined as the number of photons per second, per mm^2, per mrad^2, per 0.1% bandwidth (BW) $\Delta E/E$) of up to 10^{20} in some energy ranges[58]. It is important to note that ThomX cannot compete with such large-scale synchrotron light sources in terms of brilliance, as it can reach only approximately 10^{11} ph/s/mm^2/mrad^2/0.1% BW.

The parameters of ThomX are summarized in Table 1.3. It is hoped that ThomX will be able to deliver useful X-rays for small- to medium-scale applications for universities, museums, and hospitals, with a higher beam quality than that offered by X-ray cathode tubes and at a cheaper price than that of large synchrotron facilities.

1.4 Optical Enhancement Cavities and Their Applications

Laser-electron interactions based on an optical cavity and an electron storage ring, as described above, serve as the basis of a feasible technology for realizing compact but

Table 1.3 Parameters of the ThomX source[57]

Source	ThomX
Photon energy cut-off	46 keV (@50 MeV), 90 keV (@70 MeV)
Total flux	10^{11} – 10^{13} ph/s
Bandwidth (with a diaphragm)	1% – 10%
Divergence	$1/\gamma \sim 10$ $mrad$ without a diaphragm @ 50 MeV

high-quality X-ray sources. The optical enhancement cavity is a crucial part of such a facility and also lies at the core of this dissertation.

In the ICS process, a laser beam interacts with electron bunches to produce X-rays. With the direct use of a pulsed laser beam, much of the laser beam energy would be lost after one collision. To compensate for this, a passive Fabry-Pérot resonator, or an optical enhancement cavity, is used to recycle the phase-matched pulses and concentrate the energy of the laser beam over a very short period of time to produce very intense laser pulses. The output oscillator laser beam, however, has a relatively low average power, on the order of a hundred mW at most, whereas a power of hundreds of kW or more is needed to improve the X-ray flux. On the one hand, an amplifier is always necessary after the oscillator. To achieve the required average power level, a Fabry-Pérot cavity is used to accumulate the laser pulses. The stored laser beam is recirculated, and its electric field interferes constructively with the field of the incident pulses, up to a steady-state regime corresponding to a growth factor of more than 10,000 for our experiments case.

To our knowledge, the first use of a Fabry-Pérot resonant cavity in a pulsed laser mode dates back to the late 1970s. To excite two-photon transitions without a Doppler effect, the authors of Reference[59] stacked laser pulses in a cavity filled with gas. The use of pulsed dye lasers for ring-down spectroscopy was proposed in the late 1980s[60], as was frequency doubling in an external cavity in the picosecond regime[61]. The control of a passive cavity in an FEL emerged in the late 1990s for use in molecular spectroscopy[62].

At present, the technique of laser pulse stacking in an optical cavity has become quite mature. In addition to X- and γ-ray sources, optical cavities also have many other applications.

Absorption spectroscopy is a powerful tool for fundamental research and diagnostics. To measure the absorption of a gas, a Fabry-Pérot cavity filled with the gas of interest is

used, and the signals transmitted with and without the gas present are compared. Two methods, called CEAS (cavity-enhanced absorption spectroscopy) and CRDS (cavity ring-down spectroscopy), have been proposed for extracting this information[63].

The generation of XUV (extreme ultraviolet) harmonics in noble gases using intense femtosecond lasers is an active area of research. In 2005, a new technique was introduced for generating these high-rate (higher than the megahertz range) XUV harmonics[64]. In this technique, a femtosecond laser is coupled to a Fabry-Pérot cavity, into which a nozzle emits a jet of noble gas at the point where the beam size is at a minimum (i.e., at the beam waist). A sapphire blade is placed in the cavity after the laser-gas interaction zone. This blade, tilted at the Brewster angle for the intracavity beam, reflects the XUV harmonics generated between 20 nm and 140 nm. By optimizing the cavity-laser coupling and the intracavity peak power, excellent results have been achieved[65], thus paving the way for XUV spectroscopy.

An optical cavity can also be used to measure the polarization of the beam generated by a polarized positron source. In linear electron-positron colliders, such as the ILC (International Linear Collider) and CLIC (the Compact Linear Collider at CERN), it is essential to accurately measure the polarization states of the beams before collision. For this purpose, polarization measurements based on the Compton effect are adopted. This same process can also be used to produce polarized positrons[31].

Optical cavities are also applied in gravitational wave detection[66], laser frequency stabilization[67,68], and laser wires[69], among other applications.

1.5 Focus of the Dissertation

1.5.1 Main Work

This dissertation focuses on research and development related to high-power optical enhancement cavities for improving the X-ray flux.

The laser pulse stacking technique is described in Chapter 2. As an alternative to the classical model, a precise transient model is established that considers the CEP (carrier-envelope phase) effect and time detuning in the time and frequency domains. On the basis of this model, we analyze the cavity gain and linewidth in various cases. We found that for the same cavity gain, a higher-finesse but detuned cavity has a wider linewidth than a lower-finesse cavity without any detuning, meaning that it is easier to lock a laser to the former. A paraxial approximation of the solution for an astigmatic

cavity consisting of two astigmatic mirrors is briefly introduced, and we derived the non-paraxial corrections for general astigmatic beams and explained the *S*-shaped cavity mode observed in a non-planar four-mirror cavity.

Chapter 3 investigates various frequency stabilization methods and introduces the cavity thermal effect. We propose a new frequency stabilization method based on the polarization of a folded cavity and tuning of the cavity mirror reflectivity. Regarding the thermal effect, using Winkler's model, we find that the cavity gain is very sensitive to the mirror deformation in open loop. A strong feedback and ultra-low expansion mirrors are necessary.

High-power experiments on a prototype cavity for ThomX are reported in Chapter 4. First, the prototype S-Box cavity is introduced, including the oscillator, the amplifier, the cavity parameters and the mechanical system. A finesse of as high as approximately 26,000 is measured using four different methods. In addition, dust is found to have a strong effect on the finesse, and experiments at the final power are successfully demonstrated. The amount of power stored in the cavity can be as high as 400 kW by using a cavity with finesse 26,000. Modal instabilities were also observed.

Chapter 5 describes the design of a prototype cavity for TTX2.

1.5.2 Possible Innovative Points

This dissertation mainly makes four important contributions:

1. A precise model to describe the transient stacking process considering time detuning and the carrier-envelope phase effect is developed. We found that for the same cavity gain, a higher-finesse but detuned cavity has a wider linewidth than a lower-finesse cavity without any detuning, meaning that it is easier to lock a laser to the former.

2. A new laser frequency stabilization technique is proposed. This method relies on the cavity polarization property and tuning of the cavity mirror reflectivity. We use s- and p-wave phase detuning to produce an error signal that is used to lock the laser on the cavity. Compared to the traditional PDH method, this technique is simpler without need for frequency modulation and demodulation and we can choose the polarization we want inside the cavity.

3. To our best knowledge, we first derive the corrections to general astigmatic beams by solving Lax perturbation series of the wave equation for general elliptic Gaussian beams. This model agrees qualitatively with *S*-shaped cavity mode observed in a non-

planar four-mirror cavity.

4. High-power experiments were performed on a prototype cavity for ThomX. We obtained 400 kW power stored in the cavity in pulsed regime by using a cavity with finesse 26,000 and modal instabilities which limits this power were observed. We believe that this effect originates from cavity modal frequency degeneracy induced by thermal effect.

Chapter 2 Laser Pulse Stacking Technique

The laser pulse stacking technique plays an important role in our compact X-ray source. Fabry-Pérot resonators are mainly used to amplify the injected power and to circulate pulses. In this chapter, fundamental studies on Fabry-Pérot cavities are described. First, we introduce some basic laser concepts, and we present the operational principles of a pulse laser and an optical cavity by introducing the classical model and establishing a new transient model. In addition, we compare the linewidths of two cavities with the same gain, one with a certain finesse and no detuning and the other with a higher finesse but detuned. The latter has a wider linewidth, meaning that it is easier to lock a laser to such a cavity. Finally, astigmatic cavities are briefly discussed, and the non-paraxial corrections for general astigmatic beams are derived to explain the *S*-shaped optical mode.

2.1 Laser Principles

2.1.1 Wave Equations and Gaussian Beams

For an electromagnetic wave with a single frequency traveling along the z axis, the distribution of the light wave field satisfies the Maxwell equations. In addition, time-harmonic conditions are satisfied, and the electric field, with its complex amplitude, can be described by the Helmholtz equation as follows:

$$\nabla^2 \mathbf{e} + k^2 \mathbf{e} = 0 \tag{2-1}$$

One solution to Equation 2-1 that has a variable-separated form can be expressed as follows:

$$\mathbf{e}(x, y, z, t) = \Psi(x, y, z) \exp(i\omega t - ikz) \tag{2-2}$$

where ω is the angular frequency, $k = \omega/c$ is the wave number, and the scalar function Ψ is a partial expression of the electric field vector $\mathbf{e}$.

It is assumed that the trial solution $\Psi(x, y, z) = \Psi_0(x, y, z) \exp(-ikz)$ propagating along the z axis satisfies Equation 2-2. We can easily obtain the following equation by

substituting this trial solution:

$$(\frac{\partial^2}{\partial x^2} + \frac{\partial^2}{\partial y^2} + \frac{\partial^2}{\partial z^2} - 2ik\frac{\partial}{\partial z})\Psi(x, y, z) = 0 \tag{2-3}$$

Consider the slowly varying envelope approximation, as follows:

$$\left|\frac{\partial^2}{\partial z^2}\right| \ll \left|k\frac{\partial}{\partial z}\right|, \left|\frac{\partial^2}{\partial x^2}\right|, \left|\frac{\partial^2}{\partial y^2}\right| \tag{2-4}$$

With this approximation, Equation 2-3 simplifies to

$$(\frac{\partial^2}{\partial x^2} + \frac{\partial^2}{\partial y^2} - 2ik\frac{\partial}{\partial z})\Psi(x, y, z) = 0 \tag{2-5}$$

Equation 2-5 is valid only in the vicinity of the z axis. Because a laser generally has a very narrow beam, this equation can often be used to represent the distribution of the laser field. The case of a laser circulating in an optical cavity can be represented by imposing geometric boundary conditions on Equation 2-5. If the phase plane of the laser beam coincides with the surfaces of the optical cavity mirrors, the optical mode can propagate back and forth in the optical cavity without any change in its cross-sectional shape; in other words, optical resonance is achieved in the cavity. Such a laser beam is called a Hermite-Gaussian beam[70,71], and its mode is expressed as TEM_{mn}, where m and n denote different transverse modes:

$$\begin{aligned}\Psi_{mn}(x, y, z) = \Psi_0 \frac{\omega_0}{\omega(z)} \exp(-\frac{x^2 + y^2}{\omega^2(z)}) H_m(\frac{\sqrt{2}x}{\omega(z)}) H_n(\frac{\sqrt{2}x}{\omega(z)}) \\ \cdot \exp(-ik\frac{x^2 + y^2}{2R(z)} + i\phi(z)) \exp(-ikz)\end{aligned} \tag{2-6}$$

where

$$\begin{aligned}\omega(z) &= \omega_0\sqrt{1 + (\frac{z}{z_0})^2} \\ R(z) &= z\left(1 + (\frac{z_0}{z})^2\right) \\ \phi(z) &= (m + n + 1)\arctan(\frac{z}{z_0}) \\ z_R &= \frac{\pi\omega^2}{\lambda}\end{aligned} \tag{2-7}$$

Table 2.1 Ray matrices of common optical components

Distance d through a medium with a homogeneous refractive index n	$\begin{pmatrix} 1 & d/n \\ 0 & 1 \end{pmatrix}$
Thin lens with a focal length f	$\begin{pmatrix} 1 & 0 \\ -1/f & 1 \end{pmatrix}$
Reflective concave mirror with a curvature ρ	$\begin{pmatrix} 1 & 0 \\ -2/\rho & 1 \end{pmatrix}$

In Equation 2-7, λ is the laser wavelength, z is the axial distance from the focus (waist) of the beam, $\omega(z)$ is the beam size at position z, $R(z)$ is the radius of curvature of the beam's wavefront, $\phi(z)$ is an additional phase shift called the Gouy phase, and z_R is called the Rayleigh range. At a distance $z = z_R$, the beam size ω is larger than the waist ω_0 by a factor of $\sqrt{2}$. H_m and H_n are the Hermite polynomials of the m-th and n-th orders, respectively.

2.1.2 ABCD Law

For simplicity, the parameter $q(z)$ is defined as

$$\frac{1}{q(z)} = \frac{1}{R(z)} - i\frac{\lambda}{\pi\omega^2(z)} \tag{2-8}$$

Then, the propagation of a Gaussian beam can be described by a 2×2 transfer matrix. When a Gaussian beam with a parameter q_1 passes through an optical element described by a transfer matrix of $\begin{pmatrix} A & B \\ C & D \end{pmatrix}$, the parameter q_2 of the output beam is expressed as follows:

$$q_2 = \frac{Aq_1 + B}{Cq_1 + D} \tag{2-9}$$

When the beam passes through many optical components, we simply need to multiply the ray matrices in reverse order. In this way, the beam parameters can be traced out, and this method is often used to design setups for optical experiments. The ray matrices of several commonly used optical elements are given in Table 2.1 [72].

2.2 Classical Model of Laser Pulse Stacking

2.2.1 Pulse Laser Frequency Comb

In the time domain, the field of a pulsed laser beam consisting of an infinite number of pulses is ideally expressed as follows[73,74]:

$$e(t) = \sum_{n\to-\infty}^{n\to+\infty} e_n(t - nT)\exp(i[\omega_0(t - nT) + (\phi_0 + n \vartriangle \Phi_{ce})]) \tag{2-10}$$

where we have omitted the spatial dependence of the field. T is the period of the pulses, ω_0 is the angular frequency of the laser, ϕ_0 is the pulse phase for $n = 0$, and $\phi_0 + n \vartriangle \Phi_{ce}$ is the phase difference between the envelope and field cycles (where the abbreviation ce stands for 'carrier-to-envelope offset'). $\vartriangle \Phi_{ce}$ is also the phase difference between the cycles of the field corresponding to the n-th and $(n + 1)$-th pulses for all n. This property has been experimentally demonstrated with a relative precision of better than 10^{-15} [75,76].

As in linear optics, it is convenient to use the frequency-domain expression for the field[77]. By setting $\phi_0 = 0$ to simplify the expressions and then taking the Fourier transform of Equation 2-10, we obtain

$$\begin{aligned} FT\{e(t)\} \equiv E(\omega) &= \sum_{n\to-\infty}^{n\to+\infty} \int_{-\infty}^{+\infty} e_n(t - nT)\exp(i[\omega_0(t - nT) + n \vartriangle \Phi_{ce}])\exp(-i\omega t)dt \\ &= \sum_{n\to-\infty}^{n\to+\infty} \exp[in(-\omega T + \vartriangle \Phi_{ce})] \int_{-\infty}^{+\infty} e_n(t')\exp(-i[\omega - \omega_0]t')dt' \\ &= \sum_{n\to-\infty}^{n\to+\infty} \exp[in(-\omega T + \vartriangle \Phi_{ce})]E_n(\omega_0 - \omega) \end{aligned} \tag{2-11}$$

where $t' = t - nT$ and $E_n(\omega) = FT\{e_n\}$. Note that $E_n(\omega)$ no longer depends on n, and we have $E_n(\omega) = E_0(\omega)$ for all n. Finally, we simplify Equation 2-11 using the Poisson formula and obtain the following:

$$E(\omega) = 2\pi E_0(\omega_0 - \omega) \sum_{m\to-\infty}^{m\to+\infty} \delta(-\omega T + \Phi_{ce} - 2\pi m) \tag{2-12}$$

where δ represents the Dirac delta function. From Equation 2-12, we can derive the following fundamental information: the output pulses of a mode-locked laser form a comb in the frequency domain, as shown in Figure 2.1. This frequency comb can be

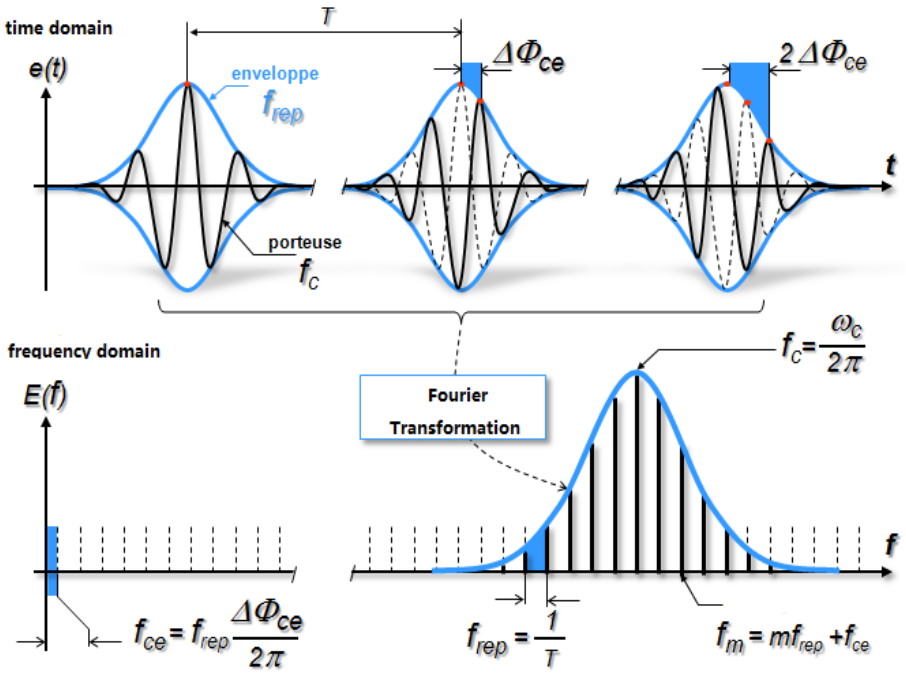

Figure 2.1 Time-domain (top) and frequency-domain (bottom) representations of the field of a pulsed laser beam[78]

expressed as follows:

$$\nu_m = \frac{\omega_m}{2\pi} = mf_{rep} + f_{rep}\frac{\Phi_{ce}}{2\pi} = mf_{rep} + f_{ce} \tag{2-13}$$

where $f_{rep} = 1/T$ is the pulse repetition frequency. Therefore, the frequency comb is defined by two parameters:

- f_{rep} describes the distance between two peaks of the comb.
- $f_{ce} = f_{rep}\Phi_{ce}/2\pi$ describes the position of the peak corresponding to $m = 0$, called the 'carrier-envelope offset frequency'.

The electric field envelope of an unchirped Gaussian pulse can be expressed as follows:

$$e_n(t - nT) = (\frac{4\ln 2}{\pi\tau^2})^{\frac{1}{4}} \exp(-2\ln 2\frac{(t - nT)^2}{\tau^2}) \tag{2-14}$$

where τ is the pulse duration.

2.2.2 Optical Cavity Frequency Comb

First, we consider a Fabry-Pérot cavity consisting of two spherical mirrors with the same radius of curvature R and separated by a distance of L_{cav}, as shown in Figure 2.2.

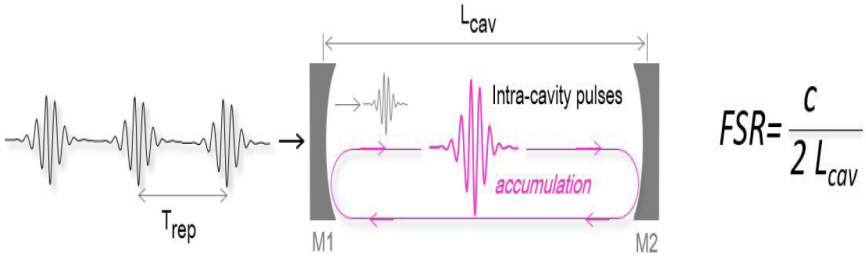

Figure 2.2 Laser pulse stacking process in a two-mirror optical cavity.

In addition, we choose R and L_{cav} such that the cavity configuration is stable[79].

Regarding the cavity mirrors, we assume that the coating is optimized for a wavelength of λ_0 and that the reflection coefficient can be expressed as

$$r(\omega) = \rho(\omega)\exp(-i\phi(\omega)) \tag{2-15}$$

where $\rho(\omega), \varphi(\omega)$ are real. We neglect the absorption and scattering losses in the mirror coatings, such that $|r(\omega)|^2 + |t(\omega)|^2 = 1$, where $t(\omega)$ is the transmission coefficient. To our knowledge, some laboratories, such as the Laboratoire des Matériaux Avancés (LMA) in Lyon, France, can manufacture high-quality mirrors with extremely small losses (less than 1 ppm).

To obtain the expression for the intracavity field, the frequency-domain representation of the field given in Equation 2-12 is used to sum the contributions from each element of the frequency comb. The field circulating in the cavity is expressed as

$$\begin{aligned} E_{cav} &= \widetilde{t}(\omega)E_0(\omega_0-\omega)[1 + r^2(\omega)\exp(\frac{-2i\omega L_{cav}}{c}) + r^4(\omega)\exp(\frac{-4i\omega L_{cav}}{c}) + \cdots] \\ &= \frac{\widetilde{t}(\omega)E_0(\omega_0-\omega)}{1-\rho^2(\omega)\exp(-i\Phi(\omega))} \end{aligned} \tag{2-16}$$

where $\Phi(\omega) = 2[\omega L_{cav}/c + \phi(\omega)]$.

Before determining the condition for resonance, we follow the calculation presented in Reference[80] and write the phase expansion term of the reflection coefficient of the mirrors as follows:

$$\phi(\omega) = \phi_0 + (\omega-\omega_0)\tau_0 + \epsilon(\omega-\omega_0) \tag{2-17}$$

where $\phi_0 = \phi(\omega_0)$, $\tau_0 = \frac{d\phi(\omega)}{d\omega}|\omega = \omega_0$, and $\epsilon(\omega - \omega_0)$ includes all higher-order terms in $(\omega - \omega_0)$ in the series, which can usually be neglected. Then, $\Phi(\omega)$ can be written as follows:

$$\Phi(\omega) = \omega(\frac{2L}{c} + 2\tau_0) + 2(\phi_0 - \omega_0\tau_0 + \epsilon(\omega - \omega_0)) \tag{2-18}$$

The cavity resonance frequencies can be obtained from the resonance condition:

$$n\lambda = 2L_{cav} + 2 * \frac{\phi(\omega)\lambda}{2\pi} \tag{2-19}$$

where λ is the optical wavelength.

We obtain the n-th resonance frequency as follows:

$$\begin{aligned} \nu_n &= (n - \frac{\phi_0}{\pi} + \frac{\omega_0\tau_0}{\pi} - \frac{\epsilon(\omega - \omega_0)}{\pi})\frac{c}{2(L_{cav} + c\tau_0)} \\ &= n\frac{c}{2(L_{cav} + c\tau_0)} + \frac{2\omega_0\tau_0 - 2\phi_0 - 2\epsilon}{2\pi}\frac{c}{2(L_{cav} + c\tau_0)} \\ &= nFSR + \nu_0 \end{aligned} \tag{2-20}$$

where FSR, short for 'free space range', is the frequency interval of the longitudinal cavity mode.

Remarkably, the frequency comb of the optical cavity is isometric with $\delta\nu = c/2/(L_{cav} + c\tau_0)$, as shown in Figure 2.3. The first-order term τ_0 plays a role in determining the tooth interval FSR of the frequency comb, and the teeth are shifted by a stationary offset of ν_0.

For a picosecond laser pulse, the intracavity dispersion of a low finesse cavity is so small that we can neglect it[81,82]. Thus, $FSR = c/(2L_{cav})$ and the n-th resonance frequency can be taken to be

$$\nu_n = n\frac{c}{2L_{cav}} \tag{2-21}$$

The dashed lines in the frequency-domain plot at the bottom of Figure 2.1 actually represent the optical cavity frequency comb. Hence, the resonance condition simply corresponds to the overlap of these two frequency combs.

Hence, the optical cavity frequency comb is also defined by two parameters:

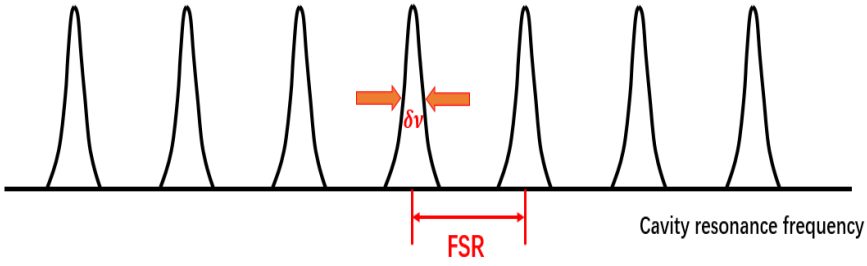

Figure 2.3 Optical cavity frequency comb.

- FSR describes the tooth interval of the frequency comb.
- ν_0 describes the position of the peak corresponding to $n = 0$.

2.2.3 Cavity Parameters and Resonance Condition

Before deriving the resonance condition, we need to define several important parameters of an optical cavity.

Linewidth The linewidth of the cavity, $\delta\nu$, is the width of the cavity mode at half the maximum height, as shown in Figure 2.3. A narrow linewidth means that it is difficult to lock a laser to the cavity, and a strong and robust feedback system is needed.

Finesse The finesse, $\mathcal{F}$, is the ratio between the free space range and the linewidth:

$$\mathcal{F} = \frac{FSR}{\delta\nu} \tag{2-22}$$

It is an important index for measuring the quality of an optical cavity. The finesse is determined by the parameters of the cavity mirrors; thus, it can also be defined as follows:

$$\mathcal{F} = \frac{\pi\sqrt{R_{eff}}}{1 - R_{eff}} \tag{2-23}$$

where R_{eff} is the square root of the product of the power reflection coefficients of all cavity mirrors, $R_{eff} = \sqrt{R_1 R_2 \cdots R_n}$.

Gain The gain is defined as the ratio between the energy E_{circ} stored in the cavity and the input laser energy E_{in}:

$$G = \frac{E_{circ}}{E_{in}} \tag{2-24}$$

For a high-finesse cavity, the gain can be on the order of 10^4.

Impedance matching When $r_1 = r_2 r_3 \cdots r_n$ is satisfied, where r_i is the field reflection coefficient of the i-th cavity mirror, we refer to this condition as *impedance matching*. In addition, $r_1 = r_2 r_3 \cdots r_n$ is equivalent to $T_1 = T_2 + T_3 \cdots T_n$, where T_i is the power transmission coefficient of the i-th cavity mirror. Impedance matching means that the input is equal to the total loss, including transmission.

As discussed in Sections 2.2.1 and 2.2.2, the pulse laser frequency comb consists of a set of Dirac delta functions, meaning that the teeth of the comb are straight lines. By contrast, the optical cavity frequency comb has a certain linewidth.

The resonance condition corresponds to the overlap of the two combs:

$$\begin{cases} f_{rep} = FSR \\ f_{ce} = \nu_0 \end{cases} \tag{2-25}$$

2.3 Precise Transient Model of Laser Pulse Stacking

In Section 2.2, the classical model of laser pulse stacking is described, providing a good understanding of the two frequency combs. However, the classic model of laser pulse stacking only works in steady state and cannot describe the transient process of cavity filling.

Hence, in this section, we establish a precise model for a beam with an arbitrary envelope to enable an analysis of the transient stacking process in both the time and frequency domains. As a special case, the process of filling the cavity with a Gaussian beam is analyzed. The results in both domains are the same, thereby verifying the correctness of the model.

2.3.1 Time-Domain Analysis

First, we define the following parameters:

ω_0: the central frequency, $\omega_0 = \frac{2\pi c}{\lambda_0}$

T: the round-trip time of the laser cavity (corresponding to a laser repetition rate of $f_{rep} = \frac{1}{T}$)

τ_{FP}: the round-trip time of the external Fabry-Pérot cavity

$\triangle \Phi_{ce}$: the carrier-envelope phase shift or pulse-to-pulse phase shift

$\alpha(t)$: the pulse envelope

r_i: the field reflection coefficient of the i-th cavity mirror, where we neglect the reflection phase shift of the mirror

R_i: the power reflection coefficient of the i-th cavity mirror, $R_i = r_i^2$

t_i: the field transmission coefficient of the i-th cavity mirror

T_i: the power transmission coefficient of the i-th cavity mirror, $T_i = t_i^2$

The electromagnetic field of the q-th single pulse is

$$e_q(t) = \alpha(t - qT)\exp(i[\omega_0(t - qT) + q \triangle \Phi_{ce}]) \tag{2-26}$$

Hence, the electromagnetic field of the pulse laser, expressed in a sequential representation, is

$$e(t) = \sum_q e_q(t) = \sum_q \alpha(t - qT)\exp(i[\omega_0(t - qT) + q \triangle \Phi_{ce}]) \tag{2-27}$$

When a pulsed laser beam is injected into an m-mirror optical cavity, a phase shift of $\pi/2$ arises during transmission. We can obtain the electromagnetic field inside the Fabry-Pérot cavity for N consecutive pulses as follows:

$$\begin{aligned} e_{c,N}(t) &= it_1 \sum_{k=0}^{N-1} \rho^k e_{N-1-k}(t - k\tau_{FP}) \\ &= \exp\left(i\omega_0 t + i(N-1)(\triangle \Phi_{ce} - \omega_0 T)\right) it_1 \sum_{k=0}^{N-1} \left(\rho \exp(-i(\omega_0 \delta\tau + \triangle \Phi_{ce}))\right)^k \alpha(t - k\delta\tau - (N-1)T) \end{aligned} \tag{2-28}$$

where $\rho \equiv r_1 r_2 \cdots r_m$ and $\delta\tau = \tau_{FP} - T$.

By integrating the electromagnetic field given in Equation 2-28 over time from negative infinity to positive infinity, we can obtain the contribution of the N-th pulse to the energy stored in the cavity during cavity filling. Thus, the energy stored in the

Fabry-Pérot cavity after the N-th pulse is

$$
\begin{aligned}
E_{c,N} &= \int_{-\infty}^{+\infty} \left| e_{c,N}(t) \right|^2 \\
&= T_1 \int_{-\infty}^{+\infty} \left| \sum_{k=0}^{N-1} \left(\rho \exp(-i(\omega_0 \delta\tau + \triangle \Phi_{ce})) \right)^k \alpha(t - k\delta\tau - (N-1)T) \right|^2 dt \\
&= T_1 \sum_{k,n=0}^{N-1} \rho^{k+n} \exp\Big(- i(k-n)(\omega_0 \delta\tau + \triangle \Phi_{ce}) \Big) \int_{-\infty}^{+\infty} \alpha(t - k\delta\tau - (N-1)T) \alpha(t - k\delta\tau - (N-1)T)
\end{aligned}
$$

For simplicity, we assume that $t = u + (k+n)\dfrac{\delta\tau}{2} + (N-1)T$:

$$
= T_1 \sum_{k,n=0}^{N-1} \rho^{k+n} \exp\Big(- i(k-n)(\omega_0 \delta\tau + \triangle \Phi_{ce}) \Big) \int_{-\infty}^{+\infty} \alpha(u - (k-n)\frac{\delta\tau}{2}) \alpha(u + (k-n)\frac{\delta\tau}{2}) du
$$

For simplicity, we also assume that $\triangle k = k - n$:

$$
\begin{aligned}
&= \frac{T_1}{1-\rho^2} \Bigg((1 - \rho^{2N}) \int_{-\infty}^{+\infty} \alpha^2(u) du \\
&+ 2 \sum_{\triangle k=1}^{N-1} (\rho^{\triangle k} - \rho^{2N - \triangle k}) \cos\left(\triangle k (\omega_0 \delta\tau + \triangle \Phi_{ce}) \right) \int_{-\infty}^{+\infty} \alpha(u - \triangle k \frac{\delta\tau}{2}) \alpha(u + \triangle k \frac{\delta\tau}{2}) du \Bigg)
\end{aligned}
\tag{2-29}
$$

According to Parseval's law, we have $\int_{-\infty}^{+\infty} \alpha^2(t) du = \int_{-\infty}^{+\infty} \left| \hat{\alpha}^2(f) \right| df$, where $\hat{\alpha}(f)$ is the Fourier transform of $\alpha(t)$. By simplifying Equation 2-29, we obtain

$$
\begin{aligned}
E_{c,N} =& \frac{T_1}{1-\rho^2} \Bigg((1 - \rho^{2N}) \int_{-\infty}^{+\infty} \left| \hat{\alpha}^2(f) \right| df \\
&+ 2 \sum_{\triangle k=1}^{N-1} (\rho^{\triangle k} - \rho^{2N - \triangle k}) \cos\left(\triangle k (\omega_0 \delta\tau + \triangle \Phi_{ce}) \right) \int_{-\infty}^{+\infty} \left| \hat{\alpha}(f) \right|^2 \exp(i 2\pi f \triangle k \delta\tau) df \Bigg)
\end{aligned}
\tag{2-30}
$$

Now, we define the function $A(t)$ as the inverse Fourier transform of $|\hat{\alpha}(f)|^2$, as shown in Equation 2-31. In addition, the total detuning phase Φ_D is the sum of the carrier-envelope phase $\triangle \Phi_{ce}$ and $\omega_0 \delta\tau$.

$$
\begin{aligned}
A(t) &= FT^{-1}\Big(|\hat{\alpha}(f)|^2 \Big)(t) = \int_{-\infty}^{+\infty} |\hat{\alpha}(f)|^2 \exp(i 2\pi f t) \\
\Phi_D &= \triangle \Phi_{ce} + \omega_0 \delta\tau
\end{aligned}
\tag{2-31}
$$

From Equation 2-30, it follows that

$$E_{c,N} = \frac{T_1}{1-\rho^2}\left(2\sum_{\triangle k=0}^{N-1}(\rho^{\triangle k} - \rho^{2N-\triangle k})\cos(\triangle k\Phi_D)A(\triangle k\delta\tau) - (1-\rho^{2N})A(0)\right) \tag{2-32}$$

When infinite pulses are injected into the cavity, i.e., $N \to +\infty$, the cavity will be in a steady state:

$$E_{c,\infty} = \frac{T_1}{1-\rho^2}\left(2\sum_{\triangle k=0}^{\infty}\rho^{\triangle k}\cos(\triangle k\Phi_D)A(\triangle k\delta\tau) - A(0)\right) \tag{2-33}$$

Equations 2-31 and 2-33 generally describe the transient and steady-state processes, respectively, of filling the Fabry-Pérot cavity with laser pulses with an envelope of $\alpha(t)$.

We take a Gaussian beam as an example for the following analysis. A Gaussian pulse without a chirp can be expressed as

$$\alpha(t) = B\exp(-\alpha t^2) \tag{2-34}$$

where α determines the duration of the laser pulse.

Then, we can obtain the function $\alpha(t)$ through inverse Fourier transformation and obtain $|\hat{\alpha}(f)|^2$:

$$|\hat{\alpha}(f)|^2 = B^2\frac{\pi}{\alpha}\exp(\frac{2\pi^2 f^2}{\alpha}) \tag{2-35}$$

The total injected laser energy E_0 is

$$E_0 = \int |\hat{\alpha}(f)|^2 dt = B^2\sqrt{\frac{\pi}{2\alpha}} \tag{2-36}$$

Hence, $A(t)$ can be found as follows:

$$A(t) = FT^{-1}|\hat{\alpha}(f)|^2(t) = E_0\exp(-\frac{\alpha t^2}{2}) \tag{2-37}$$

Finally, we can obtain the cavity energy $E_{c,N}$ after the N-th pulse and the steady-state energy $E_{c,\infty}$ in the cavity:

$$
\begin{aligned}
E_{c,N} &= E_0 \frac{T_1}{1-\rho^2}\left(2\sum_{\triangle k=0}^{N-1}(\rho^{\triangle k}-\rho^{2N-\triangle k})\cos(\triangle k\Phi_D)\exp(-\frac{\alpha\triangle k^2\delta\tau^2}{2})-(1-\rho^{2N})\right)\\
E_{c,\infty}(\delta\tau=0,\triangle\Phi_{ce}=0) &= E_0\frac{T_1}{(1-\rho)^2}
\end{aligned}
\tag{2-38}
$$

The cavity energy gain is also an important parameter. From Equation 2-38, the transient gain $G_{c,N}$ (here N represents 'Normalized', not the pulse number.) and the steady gain $G_{c,\infty}$ can be obtained as follows:

$$
\begin{aligned}
G_{c,N} &= \frac{E_{c,N}}{E_{c,\infty}(\delta\tau=0,\triangle\Phi_{ce}=0)}\\
&= \frac{1-\rho}{1+\rho}\left(2\sum_{\triangle k=0}^{N-1}(\rho^{\triangle k}-\rho^{2N-\triangle k})\cos(\triangle k\Phi_D)\exp(-\frac{\alpha\triangle k^2\delta\tau^2}{2})-(1-\rho^{2N})\right)\\
G_{c,\infty} &= \frac{T_1}{(1-\rho)^2}
\end{aligned}
\tag{2-39}
$$

2.3.2 Frequency-Domain Analysis

In this section, a description of the transient process of filling the Fabry-Pérot cavity is derived in the frequency domain. The derivation procedure is similar to that in Section 2.3.1.

By taking the inverse Fourier transform of the electromagnetic field of the q-th single pulse as given in Equation 2-26, we obtain

$$
\begin{aligned}
\hat{\alpha}_q(f) &= \int_{-\infty}^{+\infty}\exp(-i2\pi ft)\alpha(t-qT)\exp(i[\omega_0(t-qT)+q\ \triangle\ \Phi_{ce}])dt\\
&\quad \text{Suppose that } u=t-qT,\omega_0=2\pi\nu_0:\\
&= \exp(iq(\triangle\Phi_{ce}-2\pi fT))\int_{-\infty}^{+\infty}\exp\big(-i2\pi(f-\nu_0)u\big)\alpha(u)du\\
&= \exp(iq(\triangle\Phi_{ce}-2\pi fT))\hat{\alpha}_q(f-\nu_0)
\end{aligned}
\tag{2-40}
$$

The electromagnetic field inside a Fabry-Pérot cavity fed with N consecutive pulses is given by Equation 2-27. Taking the inverse Fourier transform of this equation, we

obtain

$$\begin{aligned}\hat{e}_{c,N}(f) &= it_1 \sum_{k=0}^{N-1} \rho^k \exp(-ik2\pi f\tau_{FP})\hat{e}_{N-1-k}(f) \\ &= \hat{\alpha}(f-\nu_0)\exp\left(i(N-1)(\triangle\Phi_{ce}-2\pi fT)\right)it_1 \sum_{k=0}^{N-1}\left(\rho\exp(-i(\triangle\Phi_{ce}+2\pi f\delta\tau))\right)^k \\ &= \hat{\alpha}(f-\nu_0)\exp\left(i(N-1)(\triangle\Phi_{ce}-2\pi fT)\right)it_1\frac{1-\rho^N\exp(-iN(\triangle\Phi_{ce}+2\pi f\delta\tau))}{1-\rho\exp(-i(\triangle\Phi_{ce}+2\pi f\delta\tau))}\end{aligned} \tag{2-41}$$

Hence, the energy inside the Fabry-Pérot cavity after the N-th pulse is given by the Parseval equality:

$$\begin{aligned}E_{c,N} &= \int_{-\infty}^{+\infty}|e_{c,N}(t)|^2df = \int_{-\infty}^{+\infty}|\hat{e}_{c,N}(f)|^2df \\ &= T_1\int_{-\infty}^{+\infty}\left|\hat{\alpha}(f-\nu_0)\frac{1-\rho^N\exp(-iN(\triangle\Phi_{ce}+2\pi f\delta\tau))}{1-\rho\exp(-i(\triangle\Phi_{ce}+2\pi f\delta\tau))}\right|^2df \\ &= T_1\int_{-\infty}^{+\infty}\left|\hat{\alpha}(f-\nu_0)\right|^2\frac{1+\rho^{2N}-2\rho^N\cos(N(\triangle\Phi_{ce}+2\pi f\delta\tau))}{1+\rho^2-2\rho\cos(\triangle\Phi_{ce}+2\pi f\delta\tau)}df \\ &= T_1\int_{-\infty}^{+\infty}\left|\hat{\alpha}(f)\right|^2\frac{(1-\rho^N)^2+4\rho^N\sin^2\left(\frac{N}{2}(\triangle\Phi_{ce}+\omega_0\delta\tau+2\pi f\delta\tau)\right)}{(1-\rho)^2+4\rho\sin^2\left(\frac{1}{2}(\triangle\Phi_{ce}+\omega_0\delta\tau+2\pi f\delta\tau)\right)}df \\ &= T_1\int_{-\infty}^{+\infty}\left|\hat{\alpha}(f)\right|^2\frac{(1-\rho^N)^2+4\rho^N\sin^2\left(\frac{N}{2}(\Phi_D+2\pi f\delta\tau)\right)}{(1-\rho)^2+4\rho\sin^2\left(\frac{1}{2}(\Phi_D+2\pi f\delta\tau)\right)}df\end{aligned} \tag{2-42}$$

The stored energy in the steady state is given by

$$E_{c,\infty} = \frac{T_1}{(1-\rho)^2}\int_{-\infty}^{+\infty}\frac{|\hat{\alpha}(f)|^2}{1+\frac{4\rho}{(1-\rho)^2}\sin^2\left(\frac{1}{2}(\Phi_D+2\pi f\delta\tau)\right)}df \tag{2-43}$$

We again take a Gaussian beam as an example. The expression for a Gaussian pulse without a chirp is given by Equation 2-34, and its Fourier transform is given by Equation 2-35. Thus, we have

$$|\hat{\alpha}(f)|^2 = E_0\sqrt{\frac{2\pi}{\alpha}}\exp(-\frac{2\pi^2f^2}{\alpha}) \tag{2-44}$$

Then, the cavity energy $E_{c,N}$ after the N-th pulse and the steady-state energy $E_{c,\infty}$ in

the cavity can be obtained by substituting Equation 2-44 into Equations 2-42 and 2-43:

$$E_{c,N} = T_1 E_0 \sqrt{\frac{2\pi}{\alpha}} \int_{-\infty}^{+\infty} \exp(\frac{2\pi^2 f^2}{\alpha}) \frac{(1-\rho^N)^2 + 4\rho^N \sin^2\left(\frac{N}{2}(\Phi_D + 2\pi f \delta\tau)\right)}{(1-\rho)^2 + 4\rho \sin^2\left(\frac{1}{2}(\Phi_D + 2\pi f \delta\tau)\right)} df \quad (2\text{-}45)$$

$$\begin{aligned} E_{c,\infty}(\delta\tau = 0, \triangle\Phi_{ce} = 0) &= E_0 \frac{T_1}{(1-\rho)^2} \sqrt{\frac{2\pi}{\alpha}} \int_{-\infty}^{+\infty} \exp(-\frac{2\pi^2 f^2}{\alpha})^2 df \\ &= E_0 \frac{T_1}{(1-\rho)^2} \end{aligned} \quad (2\text{-}46)$$

The normalized gain $G_{c,N}$ and the steady gain are expressed as

$$\begin{aligned} G_{c,N} &= \frac{E_{c,N}}{E_{c,\infty}(\delta\tau = 0, \triangle\Phi_{ce} = 0)} \\ &= \frac{T_1}{(1-\rho)^2} \sqrt{\frac{2\pi}{\alpha}} \int_{-\infty}^{+\infty} \exp(\frac{2\pi^2 f^2}{\alpha}) \frac{(1-\rho^N)^2 + 4\rho^N \sin^2\left(\frac{N}{2}(\Phi_D + 2\pi f \delta\tau)\right)}{1 + \frac{4\rho}{(1-\rho)^2} \sin^2\left(\frac{1}{2}(\Phi_D + 2\pi f \delta\tau)\right)} df \\ G_{c,\infty} &= \frac{T_1}{(1-\rho)^2} \end{aligned} \quad (2\text{-}47)$$

On the basis of the above discussions, we can determine the relationship between the gain and the finesse.

In an impedance-matched cavity, we have $r_1 = r_2 \cdots r_n$; hence, $\rho = r_1 r_2 \cdots r_n = R_1$. Finally, we have

$$G = \frac{T_1}{(1-\rho)^2} = \frac{1}{1-\rho} \simeq \frac{\mathcal{F}}{\pi} \quad (2\text{-}48)$$

However, the gain in the impedance matching case is not maximal. For a cavity with a given finesse, the maximum value of T_1 is necessary to achieve the maximal gain, according to Equation 2-47.

Because $\rho = r_1 r_2 \cdots r_n$, the minimum value of r_1 corresponds to $r_2 r_3 \cdots r_n \simeq 1$. This implies that $\rho = r_1$ in the maximal gain case; then, we can write

$$G = \frac{T_1}{(1-\rho)^2} = \frac{1-\rho^2}{(1-\rho)^2} \approx \frac{2\mathcal{F}}{\pi} \quad (2\text{-}49)$$

Remarkably, the maximal gain is twice as high as the gain in the impedance matching case.

2.3.3 Examples and Plots

Sections 2.3.1 and 2.3.2 above establish a complete model of the transient stacking process for laser pulses with an envelope $\alpha(t)$ of any shape in the time and frequency domains. Although the steady-state cavity energy $E_{c,\infty}$ and the cavity energy gain $G_{c,\infty}$ for Gaussian pulses are the same in both domains, as shown by Equations 2-38, 2-39, 2-46 and 2-47, this is not sufficient to ensure a correct approximation of the transient process. The energy after the N-th pulse, $E_{c,N}$, seems to differ between the two domains, at least in form. Thus, it is interesting to analyze the cavity-filling process for different cases.

Consider the injection of Gaussian pulses with a duration of ps into a cavity with a high finesse of $\mathcal{F} = 10,000$. α is determined by

$$\frac{1}{\sqrt{\alpha}} = 1 \text{ ps} \tag{2-50}$$

When the two frequency combs are perfectly superposed, i.e., $\delta\tau = 0$ and $\triangle\Phi_{ce} = 0$ mrad, the main resonance occurs, as shown in Figure 2.4. The filling curves overlap perfectly for both representations. In addition, the highest gain is reached in the filling process.

However, if the pulse laser frequency comb has an offset, such as $\triangle\Phi_{ce} = 1$ mrad, the normalized gain drops considerably, to less than 20%, as seen in Figure 2.5. In addition, the normalized gain shows a slight oscillation and ultimately stabilizes at 10%. Figure 2.6 shows that when the frequency offset is $f_{rep}/2$, i.e., $\triangle\Phi_{ce} = \pi$ rad, the gain is almost zero, showing no resonance at all, and there is excessive oscillation. Here, we present quantitative calculations concerning the CEP (carrier-envelope phase) effect on the cavity resonance. In fact, the CEP has a very strong effect on the gain for a high-finesse cavity.

Figure 2.7 shows the normalized gain as a function of the number of injected pulses when $\delta\tau = \lambda/c$, meaning that the difference in cavity length between the pulse laser and the Fabry-Pérot cavity is λ. A resonance still exists, and the final gain is approximately 10%. However, in the presence of a CEP of $\triangle\Phi_{ce} = 10$ mrad, there is no resonance, and the gain is close to zero, as shown in Figure 2.8.

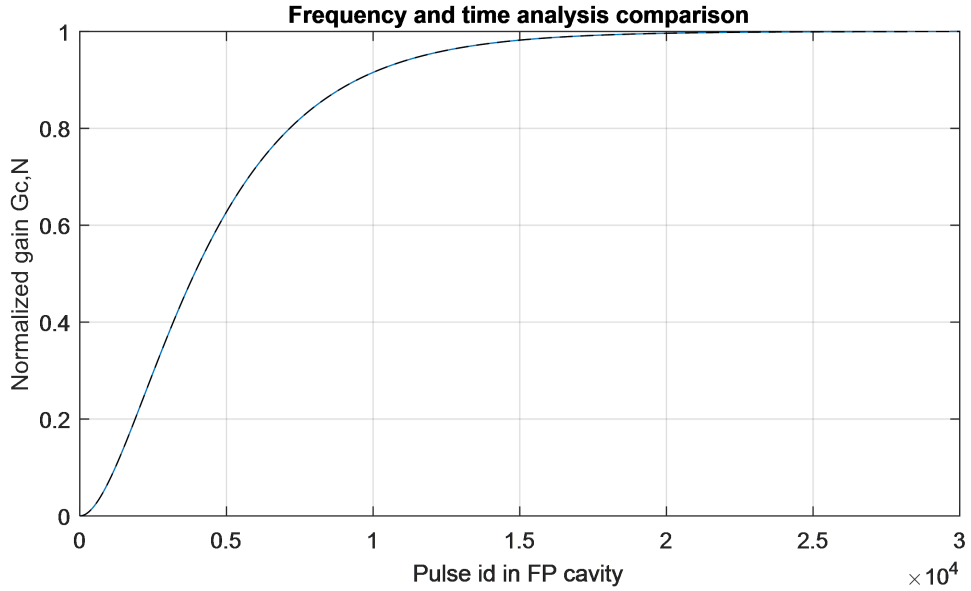

Figure 2.4 Normalized cavity gain ($\delta\tau = 0$, $\triangle\Phi_{ce} = 0$ mrad) as a function of the number of injected pulses. The dashed line corresponds to the time-domain analysis, and the solid line corresponds to the frequency-domain analysis.

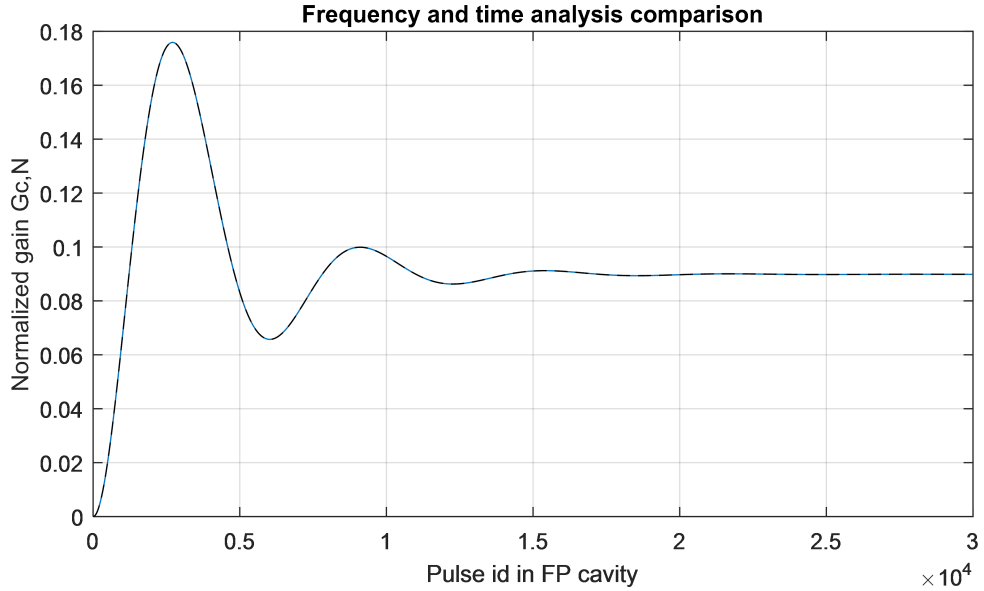

Figure 2.5 Normalized cavity gain ($\delta\tau = 0$, $\triangle\Phi_{ce} = 1$ mrad) as a function of number of injected pulses. The dashed line corresponds to the time-domain analysis, and the solid line corresponds to the frequency-domain analysis.

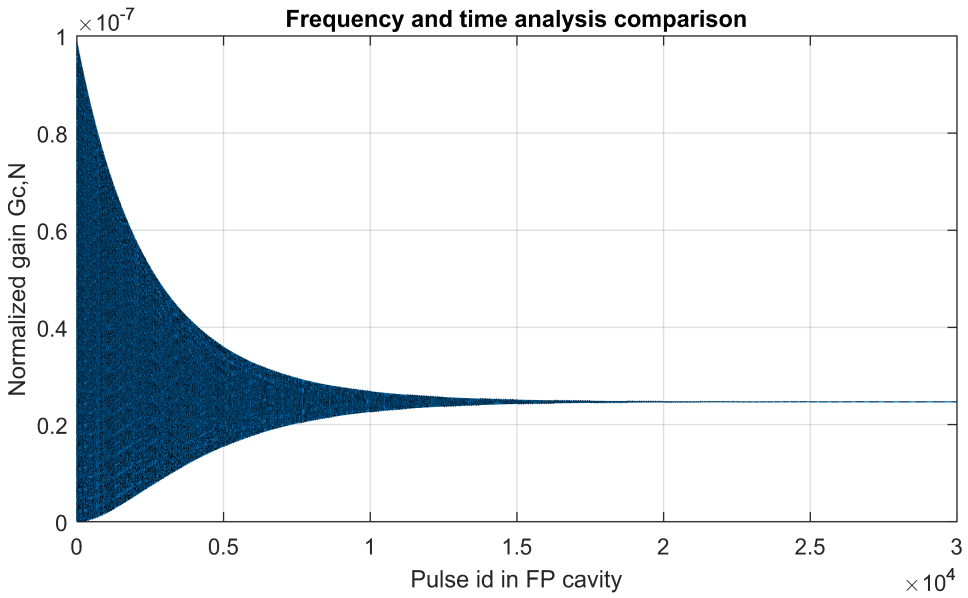

Figure 2.6 Normalized cavity gain ($\delta\tau = 0$, $\triangle\Phi_{ce} = \pi$ rad) as a function of the number of injected pulses. The dashed line corresponds to the time-domain analysis, and the solid line corresponds to the frequency-domain analysis.

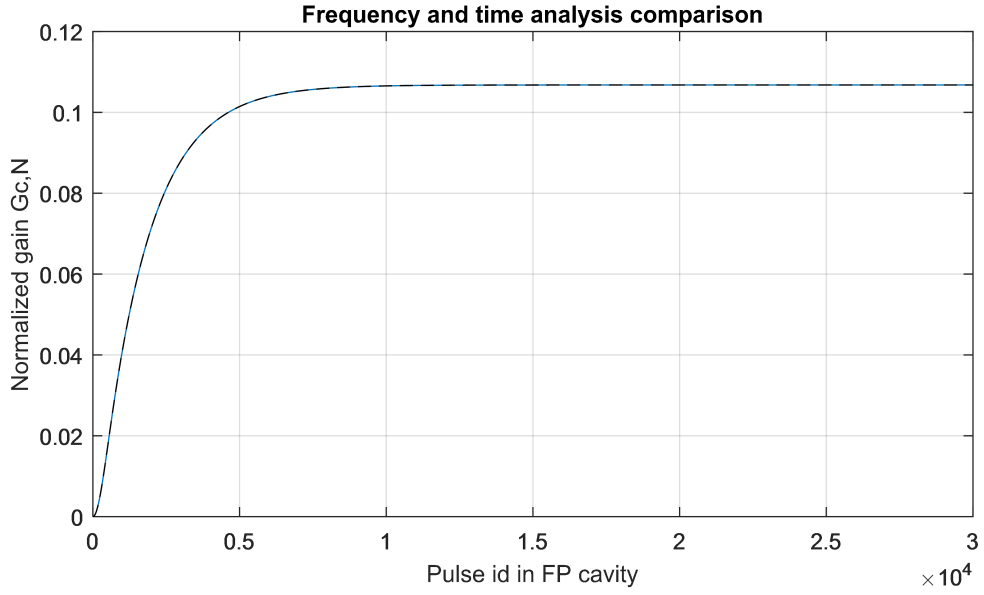

Figure 2.7 Normalized cavity gain ($\delta\tau = \frac{\lambda}{c}$, $\triangle\Phi_{ce} = 0$ mrad) as a function of the number of injected pulses. The dashed line corresponds to the time-domain analysis, and the solid line corresponds to the frequency-domain analysis.

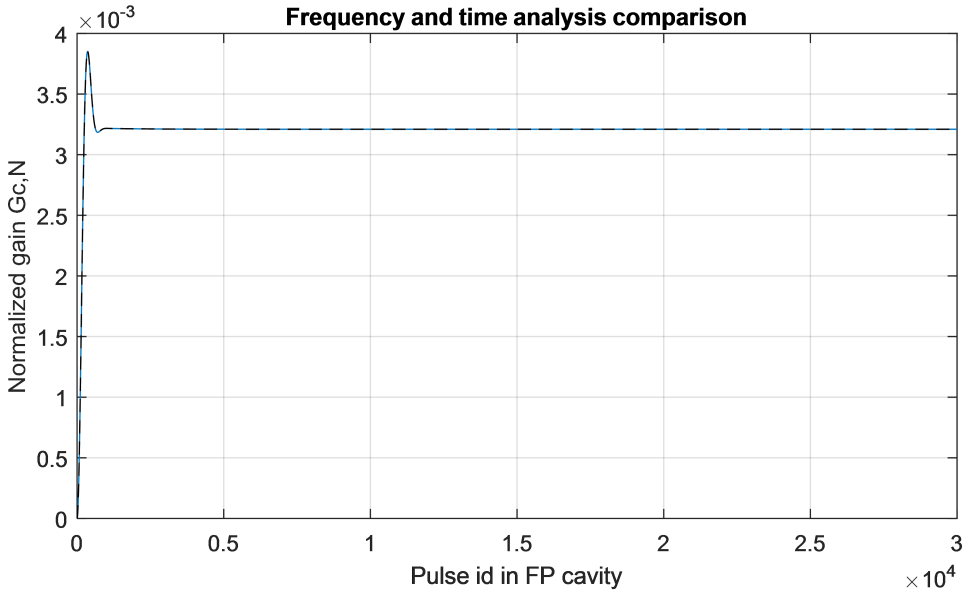

Figure 2.8 Normalized cavity gain ($\delta\tau = \frac{\lambda}{c}$, $\triangle\Phi_{ce} = 10$ mrad) as a function of the number of injected pulses. The dashed line corresponds to the time-domain analysis, and the solid line corresponds to the frequency-domain analysis.

2.4 Cavity Gain and Linewidth Analysis

To keep the cavity constantly at resonance, it is necessary to lock the laser to the cavity using a feedback system. The cavity gain under locking is a parameter of interest, and the linewidth is also an important parameter that determines the feedback precision.

2.4.1 Locking Concept

Many sources of laser noise exist in the optical system, such as the pump light, beam axis fluctuations and the positions of the mirrors. The cavity length may fluctuate by several nanometers, even for a free-running mode-locked pulse laser. Therefore, it is impossible to keep the cavity constantly at resonance without a locking system.

As discussed in Section 2.2, the resonance condition corresponds to the perfect overlap of the two frequency combs; i.e., Equation 2-25 must be satisfied. Figure 2.9 intuitively illustrates the matching between the two frequency combs. When $f_{rep} = FSR$ and $f_{ce} = 0$, the best coupling is obtained, as shown in Figure 2.9(a). In the case of $f_{rep} \neq FSR$, many of the teeth of the pulse laser frequency comb cannot couple to the cavity, as seen in Figure 2.9(b). Figure 2.9(c),(d) shows the effect of the offset f_{ce} on the coupling.

Locking analysis is always conducted in the steady state. The goal is to determine the

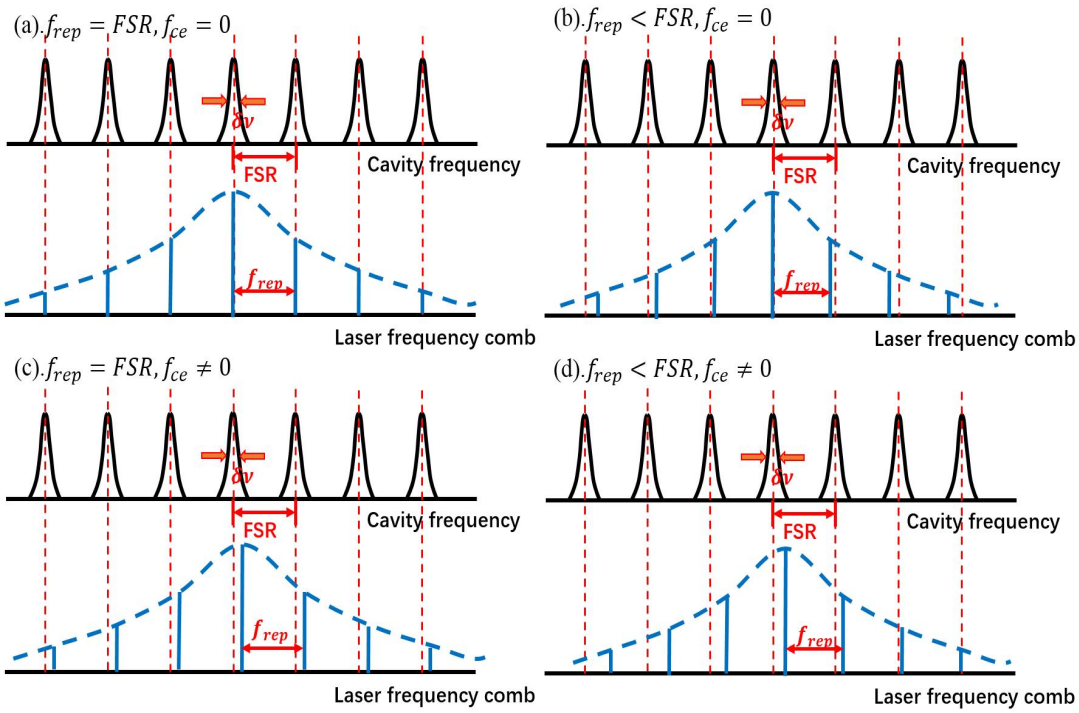

Figure 2.9 Schematic illustration of the coupling of the cavity and laser frequency combs.

relationship between the cavity detuning $\delta\tau$ and the CEP $\triangle\Phi_{ce}$ to ensure that the maximum energy can always be obtained inside the Fabry-Pérot cavity. We use the frequency-domain representation given in Equation 2-43 because of its ease of interpretation.

In Equation 2-43, the periodicity of the $\sin^2$ function relative to f is $\frac{1}{\delta\tau}$. We assume that the detuning $\delta\tau$ is small. Then, the periodicity of the $\sin^2$ function is very large. For a cavity detuning of a few wavelengths, $k\lambda$, we have

$$\frac{1}{\delta\tau} = \frac{c}{k\lambda} = \frac{\nu_0}{k} \tag{2-51}$$

Because the width of one period of the function in the denominator ($\sin^2$) is much wider than the width of the laser spectrum, the goal is simply to center the phase of the $\sin^2$ function approximately at the maximum of the laser pulse spectrum, which requires

$$\Phi_D = \triangle\phi_{ce} + \omega_0\delta\tau = 0 \tag{2-52}$$

Equation 2-52 is the locking expression. Then, one can determine the energy inside the Fabry-Pérot cavity when the laser is locked to the cavity. According to Equation 2-33, in the time domain, we obtain

$$E_{c,\infty}(locked) = \frac{T_1}{1-\rho^2}\left(2\sum_{\triangle k=0}^{N-1}\rho^{\triangle k}A(\triangle k\delta\tau) - A(0)\right) \tag{2-53}$$

According to Equation 2-43, in the frequency domain, we obtain

$$E_{c,\infty}(locked) = T_1\int_{-\infty}^{+\infty}\frac{|\hat{\alpha}(f)|^2}{(1-\rho)^2+4\rho\sin^2(\pi f\delta\tau)}df \tag{2-54}$$

2.4.2 Linewidths With and Without Detuning

The cavity linewidth is an extremely important Fabry-Pérot parameter. When the finesse is higher, the linewidth is narrower. A narrow linewidth means that it is difficult to lock the laser to the cavity, and a strong and robust feedback system (to be discussed in Chapter 3) is needed. Before investigating the linewidth, we must calculate the gain under locking.

When the laser is locked to the cavity ($\triangle\Phi_D = 0$), the steady-state energy $E_{c,\infty}(locked)$ for a Gaussian beam is given by Equations 2-37 and 2-53:

$$\begin{aligned} E_{c,\infty}(locked) &= E_0\frac{T_1}{1-\rho^2}\left(2\sum_{\triangle k=0}^{\infty}\rho^{\triangle k}\exp(-\frac{\alpha\triangle k^2\delta\tau^2}{2}) - 1\right) \\ E_{c,\infty}(locked,\delta\tau=0) &= E_0\frac{T_1}{1-\rho^2}\left(2\sum_{\triangle k=0}^{\infty}\rho^{\triangle k} - 1\right) = E_0\frac{T_1}{(1-\rho)^2} \end{aligned} \tag{2-55}$$

Hence, the normalized gain $G_{c,\infty}$ is

$$\begin{aligned} G_{c,\infty}(locked) &= \frac{E_{c,\infty}(locked)}{E_{c,\infty}(locked,\delta\tau=0)} \\ &= \frac{1-\rho}{1+\rho}\left(2\sum_{\triangle k=0}^{\infty}\rho^{\triangle k}\exp(-\frac{\alpha\triangle k^2\delta\tau^2}{2}) - 1\right) \end{aligned} \tag{2-56}$$

To simplify the normalized gain $G_{c,\infty}$, we define γ and use the following approxima-

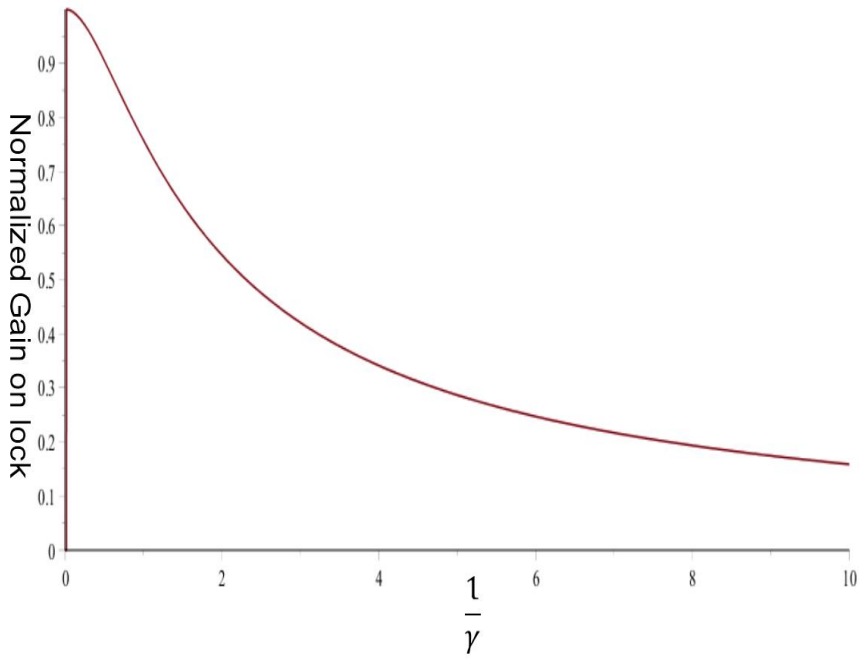

Figure 2.10 Normalized gain under locking as a function of $1/\gamma$.

tions:

$$\begin{cases} \rho = 1 - \dfrac{\pi}{\mathcal{F}} \\ \ln\rho \simeq -\dfrac{\pi}{\mathcal{F}} \\ \gamma \equiv -\dfrac{\ln\rho}{\sqrt{2\rho\alpha}\delta\tau} \simeq \dfrac{1-\rho}{\sqrt{2\rho\alpha}\delta\tau} \end{cases} \tag{2-57}$$

Finally, the normalized gain $G_{c,\infty}$ simplifies to

$$\begin{aligned} G_{c,\infty}(locked) &\simeq \frac{1-\rho}{1+\rho}\left(2\int_0^{+\infty}\rho^{\triangle k}\exp(-\frac{\alpha\triangle k^2\delta\tau^2}{2})d\triangle k - 1\right) \\ &\simeq -\frac{1-\rho}{1+\rho}\left(1+\frac{2}{\ln\rho}\sqrt{\pi}\gamma\exp(\gamma^2)(1-erf(\gamma))\right) \\ &\simeq \sqrt{\pi}\gamma\exp(\gamma^2)(1-erf(\gamma)) \end{aligned} \tag{2-58}$$

where erf is the error function. The normalized gain under locking is plotted as a function of $1/\gamma$ in Figure 2.10. We can also derive the same expression for $G_{c,\infty}(locked)$ that is given in Equation 2-58 through a frequency-domain analysis.

As discussed above, the cavity linewidth determines the degree of difficulty of locking

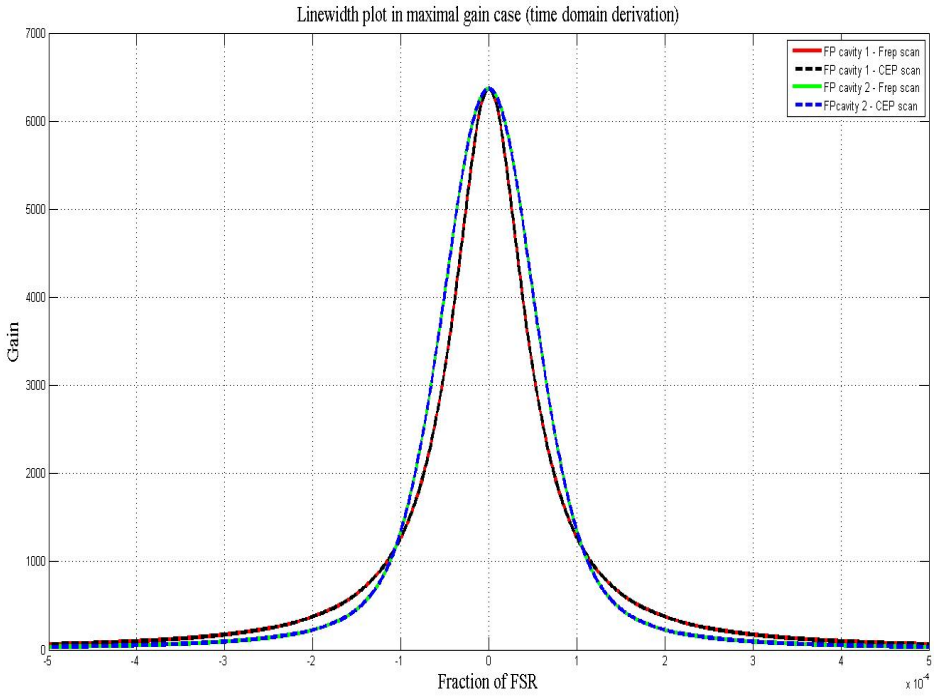

Figure 2.11 Gain as a function of detuning for Cavities 1 and 2 in the maximal gain case.

the laser to the cavity. Thus, a Fabry-Pérot cavity with a high gain and a wide linewidth is clearly preferred. A question naturally arises: between a cavity with a certain finesse but without any detuning and a detuned cavity with a higher finesse, which is preferable under the condition that both cavities have the same gain?

From Figure 2.10, we know that the detuning of the higher-finesse cavity must be suitably adjusted to achieve the same gain. We can solve the relevant equation to determine the necessary detuning as follows:

$$\begin{aligned} \sqrt{\pi}\gamma \exp(\gamma^2)(1 - erf(\gamma) = 0.5 \\ \gamma = \frac{1}{2.31} = \frac{1-\rho}{\sqrt{2\rho\alpha}\delta\tau} \end{aligned} \tag{2-59}$$

Because $\Phi_D = 0$ corresponds to the maximal gain, we can vary either the CEP $\triangle\Phi_{ce}$ or the offset f_{rep} to decrease the gain.

CEP scan: $\triangle\Phi_{ce} = \widehat{\triangle\Phi_{ce}} + \triangle\Phi_{ce}^s$

f_{rep} scan: $\delta\tau = \widehat{\delta\tau} + \delta\tau^s$

Now, we consider the following scenario:

- Cavity 1: $\mathcal{F} = 10^4$, no detuning ($\delta\tau = 0$, $\triangle\Phi_{ce} = 0$)

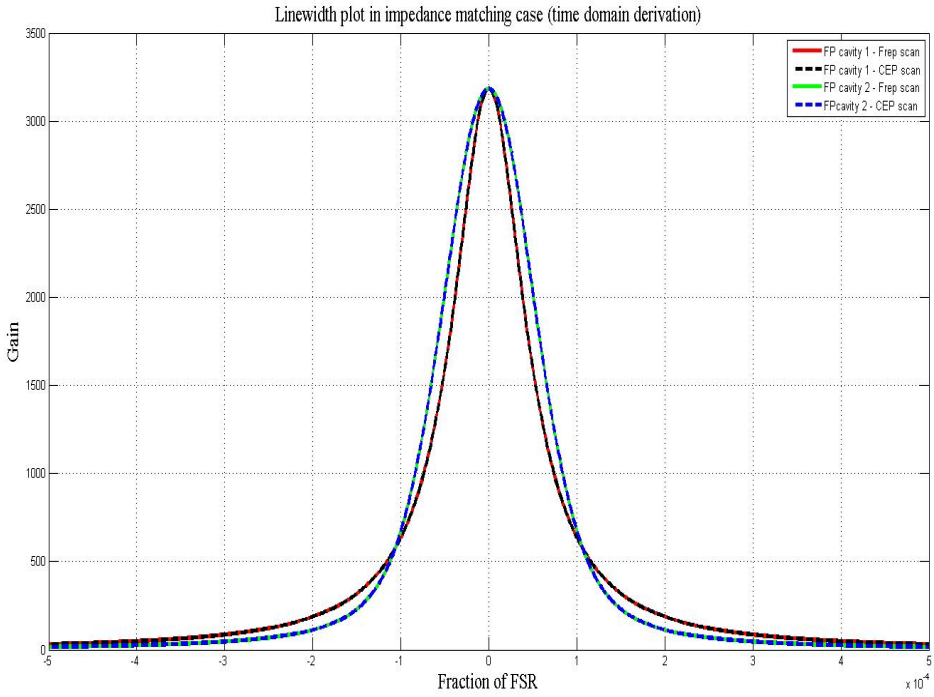

Figure 2.12 Gain as a function of detuning for Cavities 1 and 2 in the impedance matching case

- Cavity 2: $\mathcal{F} = 2 \times 10^4$, suitable detuning to achieve the same gain as Cavity 1
- CEP scan: $\triangle\Phi_{ce}^{s}$ from $-\pi/1000$ to $\pi/1000$
- f_{rep} scan: $\delta\tau^{s}$ from $-\lambda/2000/c$ to $\lambda/2000/c$

Before performing the scans, we adjust the CEP to cancel the global detuning phase $\widehat{\Phi_D} = 0$. Then, we have a new Φ_D during scanning:

$$\Phi_D = \widehat{\triangle\Phi_{ce}} + \triangle\Phi_{ce}^{s} + \omega(\widehat{\delta\tau} + \delta\tau^{s}) \tag{2-60}$$

Figures 2.11 and 2.12 show the cavity gains from the scans of Cavities 1 and 2 in the maximal gain case and the impedance matching case, respectively. The results are very consistent between the two cases. We find that the linewidth of Cavity 2 is wider than that of Cavity 1. Consequently, it is better to use a high-finesse but detuned cavity.

However, the filling processes of the two cavities are different, as shown in Figure 2.13. The initial results are not equivalent, although the same gain is ultimately reached in both cases.

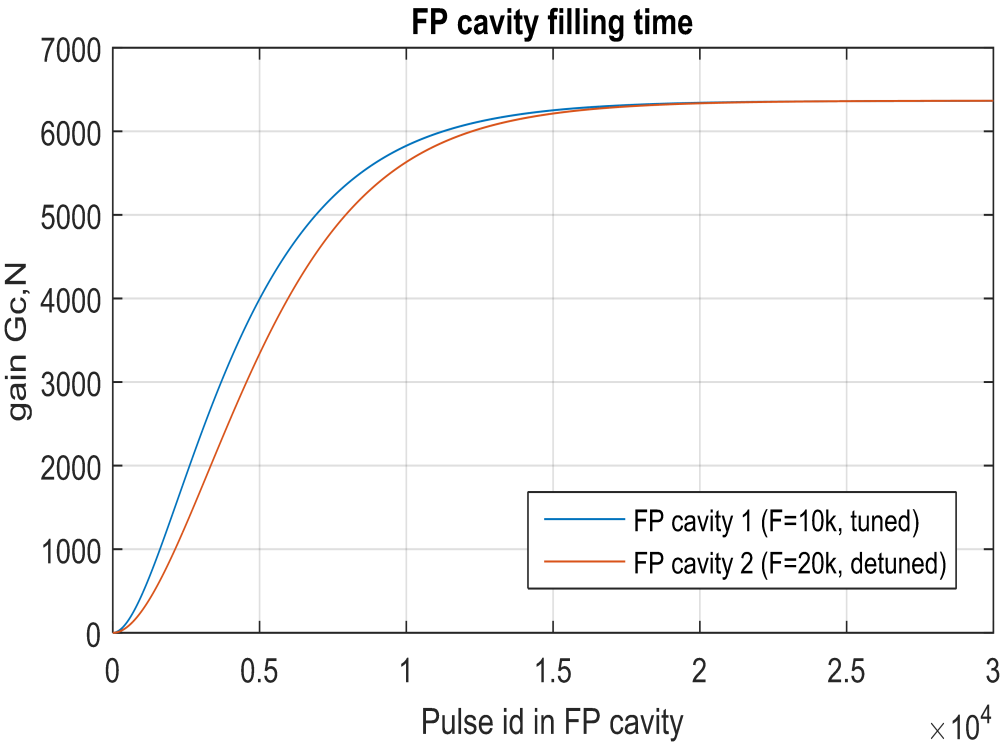

Figure 2.13 The filling processes of Cavities 1 and 2.

2.5 Astigmatic Cavity

A typical Fabry-Pérot cavity is made of two face-to-face spherical mirrors. The modes in such kind of optical cavity are transverse field distributions. They reproduce after one round-trip and bounce back and forth in the cavity. The method of calculating the modes of the typical cavity is by imposing the proper boundary conditions on free propagation light from one mirror to the other one. A complete set of Hermite Gaussian beams showed in Equation 2-6 describes the modes in such a resonator.

Another kind of resonator, named astigmatic resonators, is made of two astigmatic mirrors, such as cylindrical or elliptical mirrors. Nowadays the applications of astimatic resonators involve in many fields, like laser spectroscopy[83,84] and solid-state laser technology[85]. In addition, after the first description by Reference[86], general astigmatic light beams also receive a renewed attention in quantum optics, because they carry angular momentum while exhibiting no optical vortices on their wave front[87], in solid-state laser technology[85] and in high energy physics, where they appear to be the circularly polarized eigen-modes of the tetrahedral resonator[88] used to produce circularly polarized γ-rays[50,89]. This latter application also fits in producing gamma rays exhibiting angular momentum by Compton backscattering[90].

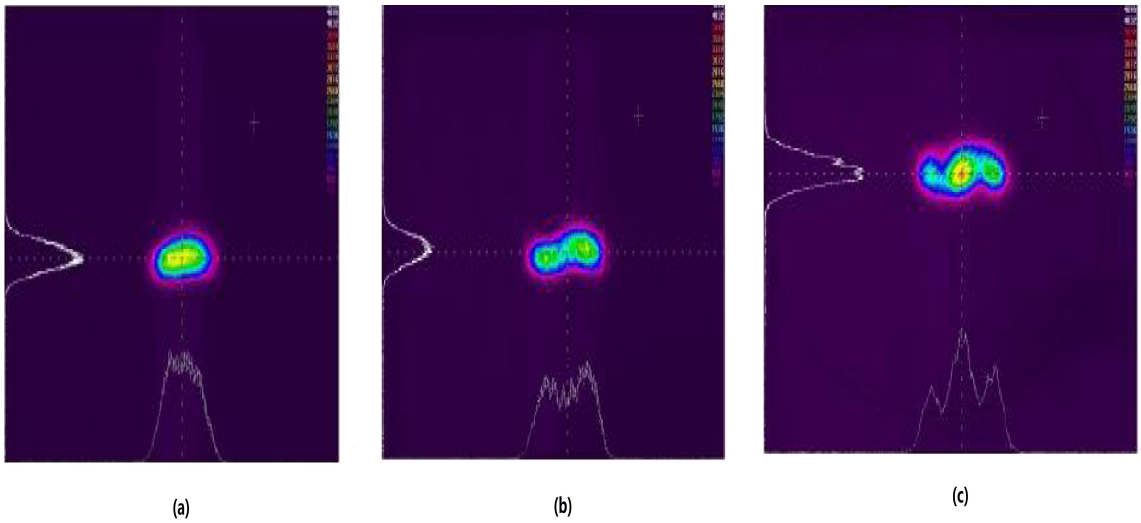

Figure 2.14 *S*-shaped beam modes observed by a 24×36 mm^2 CCD camera in a highly divergent non-planar four-mirror cavity[91]. From plot (a) to (c) the cavity is brought toward the instability region. The *S*-shaped appears in plot (c) when the cavity is close to the instability region.

In this section paraxial approximation solution of astigmatic cavity is firstly given. Explicit expression for the second order correction are next by solving Lax perturbation series of the wave equation for general elliptic Gaussian beams. Second order corrections are exemplified numerically considering the fundamental paraxial mode of an optical cavity made of two cylindrical mirrors close to its instability point.

Remarkably *S*-shaped beam modes appear as the beam propagates away from the cavity symmetry point for various choices of integration constants. This feature agrees qualitatively with observations made on a highly divergent non-planar four-mirror cavity[91] shown in Figure 2.14.

2.5.1 Paraxial Approximation Solution of Astigmatic Cavity

An astigmatic resonator is composed of two astigmatic mirrors. The cavity is twisted when the axes of the astigmatic mirrors are not parallel. In such a twisted cavity, the beam displays general astigmatism. So far, the modes and the propagation of twisted resonators has been studied by several researchers by using analytical methods[85,92,93] One operator algebraic method was proposed to get the complete set of paraxial eigenmodes in an astigmatic cavity[94]. Cavity basic information can be obtained from the complex eigenvectors of the round-trip 4×4 transfer matrix. In the following part, this method is introduced briefly.

The transfer matrix of free space propagation (distance d) is expressed as:

$$M_d = \begin{pmatrix} U & dU \\ 0 & U \end{pmatrix} \tag{2-61}$$

where U is the 2×2 unite matrix. However, the transfer matrix of an astigmatic optical element is not proportional to the unity matrix U. For an astigmatic reflective mirror, we can write the transformation matrix as[94]:

$$M_F = \begin{pmatrix} U & 0 \\ -F^{-1} & U \end{pmatrix} \tag{2-62}$$

where F is a symmetric, real 2×2 matrix. The eigenvalues of F represent the focal lengths in the two orientation of the mirrors. The orientation of the mirrors is determined by the eigenvector of F.

The round-trip matrix M which describes the composite astigmatic cavity is obtained by multiplying the matrices of all optical elements in the correct order.

In addition, the 4×4 transfer matrix of M has many interesting properties[94]. The eigenvector of M can be expressed as: μ_1, μ_1^* and μ_2, μ_2^*. μ_1, μ_1^* and μ_2, μ_2^* are two complex conjugate pairs with the corresponding eigenvalues m_1, m_1^*, and m_2, m_2^*.

In the reference plane $z = 0$, we combine two 2×2 matrix $C(0)$ and $K(0)$ into a single 2×4 matrix:

$$\begin{pmatrix} C(0) & iK(0) \end{pmatrix} = \begin{pmatrix} \mu_1^T \\ \mu_2^T \end{pmatrix} \tag{2-63}$$

Then the fundamental mode $u_{00}(\mathbf{r}, 0)$ at $z = 0$ in the astigmatic resonator is:

$$\Psi_0(\mathbf{r}, 0) = \sqrt{\frac{k}{\pi det(C(0))}} \exp\left(-\frac{k}{2}\mathbf{r}^{\mathbf{T}} C(0)^{-1} K(0)\mathbf{r} \right) \tag{2-64}$$

In order to simplify the fundamental modes, we suppose the complex matrix $\alpha(z) = \alpha_0(z) - i\alpha_1(z)$, besides $\alpha(0) = kC(0)^{-1}K(0)$. The relationship between $\alpha(z)$ and $\alpha(0)$ is[95]:

$$\alpha(z) = (U + \frac{iz}{k}\alpha(0))^{-1}\alpha(0) \tag{2-65}$$

Once we have $\alpha(z)$, we can calculate the fundamental mode at position z

$$\Psi_0(\mathbf{r},0) = \frac{[det\ \alpha_0(0)]^{\frac{1}{4}}}{[det\ \alpha(0)]^{\frac{1}{2}}}[det\ \alpha(z)]^{\frac{1}{2}} \exp\left(-\frac{1}{2}\mathbf{r}^{\mathbf{T}}\alpha(z)\mathbf{r}\right) \tag{2-66}$$

Besides, we can get the waist sizes and wavefront curvatures at position z from the matrix $\alpha(z)$.

2.5.2 *S-shaped* Non-paraxial Corrections to General Astigmatic Beams

Though highly convergent beams are usually favoured in the applications described above, the paraxial approximation of the wave equation is commonly used to model the general astigmatic beam propagation[86,87]. It raises the question of the effect of non-paraxial corrections. Non-paraxial expressions for general astigmatic focused wave eigenmodes were derived in Reference[96]. Unfortunately, these expressions lead to the paraxial expression of harmonic waves thanks to a simple dual transformation. Non-paraxial corrections for harmonic general-astigmatic beams have been published in Reference[97].

We use the method introduced in Reference[98] to solve perturbative wave equations following Lax's procedure[99] with Davis's rescription for the vector fields[100]. This method provides a natural way to solve Lax's system of peturbative equations for elliptical Gaussian beams and allows to access a wide space of solutions for the non-paraxial corrections.

However, the non-paraxial corrections depend on usually unknown initial and boundary conditions[101]. Therefore we do not pretend to provide the non-paraxial corrections of a particular general astigmatic beam but rather a large ensemble of non-paraxial solutions. Such an approach appears to be useful for studying the sensitivity of some physical processes to non-paraxial corrections such as the direct acceleration of electrons by laser beams[102].

We introduce the Lax's formalism modified for general astigmatic beam and provide second order non-paraxial corrections in the following part. Numerical examples are also provided.

Davis' method[100] is employed to derive the electromagnetic vector fields $\mathbf{E}(\mathbf{r},t) = -\nabla\Phi(\mathbf{r},t) - \partial_t\mathbf{A}(\mathbf{r},t)$ and $\mathbf{B}(\mathbf{r},t) = \nabla\times\mathbf{A}(\mathbf{r},t)$ from the scalar $\Phi(\mathbf{r},t)$ and vector $\mathbf{A}(\mathbf{r},t)$ potentials that are given by the wave equation $c^2\nabla^2\cdot\mathbf{A}(\mathbf{r},t) - \partial_t^2\mathbf{A}(\mathbf{r},t) = 0$ and the Lorenz Gauge equation $c^2\nabla\cdot\mathbf{A}(\mathbf{r},t) + \partial_t\Phi(\mathbf{r},t) = 0$.

In this section, we shall restrict ourselves to *long enough* electromagnetic pulses so that space-time coupling can be neglected[103]. We also assume that the electromagnetic wave is propagating along the z axis. We shall then look for solutions of the form

$$\mathbf{A}(\mathbf{r},t) = \Psi(\mathbf{r})g(\varphi)\exp(i\varphi)\hat{\mathbf{a}}$$

with $\varphi = \omega t - kz$, ω the optical angular frequency, $k = \omega/c = 2\pi c/\lambda$ and λ the optical wavelength. In this expression, $\hat{\mathbf{a}}$ is a unit vector which contributes to define the polarization of the electromagnetic wave[100]. Doughnut-shape radially -polarized fields are obtained by choosing $\hat{\mathbf{a}} = \hat{\mathbf{z}}$[104] whereas $\hat{\mathbf{a}} = a_x\hat{\mathbf{x}} + a_y\hat{\mathbf{y}}$ gives linear and circular polarization states.

Assuming a slowly varying envelope[105]

$$\left|\frac{1}{g(\varphi)}\frac{\mathrm{d}g(\varphi)}{\mathrm{d}\varphi}\right| \ll 1,$$

one gets $\nabla^2\Psi(\mathbf{r}) - 2ik\partial_t\Psi(\mathbf{r}) = 0$. This equation is solved pertubatively following Lax's method[99]. Accordingly the solution is obtained starting from the general astigmatic paraxial scalar field[95]

$$\Psi_0(\mathbf{r}) = \frac{[\det\alpha_0(0)]^{1/4}}{[\det\alpha(0)]^{1/2}}[\det\alpha(z)]^{1/2}\exp\left(-\frac{1}{2}\mathrm{R}^T\alpha(z)\mathrm{R}\right) \tag{2-67}$$

where $\mathrm{R}^T = (x,y)$ and $\alpha(z) = \alpha_0(z) - i\alpha_1(z)$. $\alpha_0(z)$ and $\alpha_1(z)$ are real 2×2 symmetric matrices that do not commute in the case of general astigmatism[86,106] $[\alpha_0(z),\alpha_1(z)] \neq 0$. The following identity $\alpha(z) = [I - i\alpha(0)z/k]^{-1}\alpha(0)$[95], with I the 2×2 identity matrix, highlights the intricate z dependence of $\Psi_0(\mathbf{r})$. The two eigenvectors of $\alpha(z)$ can be written $\chi_1^T = (\cos\Phi, -\sin\Phi)$ and $\chi_2^T = (\sin\Phi, \cos\Phi)$ where $\Phi \in \mathbb{C}$ is independent of z[96]. The corresponding eigenvalues of $\alpha(z)$ read

$$\frac{ik}{q_{1,2}(z)} \text{ with } q_{1,2}(z) = z - \beta_{1,2} + ip_{1,2}$$

where $\beta_{1,2}$ and $p_{1,2} \geq 0$ are real constants that coincide with the positions of the two beam waists and to the corresponding Rayleigh lengths respectively only in the case of simple astigmatism, *i.e* $[\alpha_0(z),\alpha_1(z)] = 0$[86].

Following Reference[106] we further fix the origin $z = 0$ midway between the two focus points, defined by the position where the radius of curvature is infinite along at least one direction. Introducing the 2×2 complex matrix

$$\mu(z) = \alpha^{-1}(z) = \mu_0(z) + i\mu_1(z),$$

where $\mu_{0,1}(z)$ are two 2×2 real matrices, the focus points are located at $z_{+,-} = \pm k m_0$, where $\pm m_0$ are the two eigenvalues of $\mu_0(0)$[106].

The minima of beam radii along the two main axes, that are not necessarily located at $z = z_{+,-}$, are written w_1 and w_2. One defines w_m as the smaller of these two values, and the other one as w_M. The following reduced variables are introduced that conveniently describe the beam elliptical profile

$$\xi = \frac{x}{w_m},\ \eta = \frac{y}{w_m},\ \zeta = \frac{z}{\ell_m}.$$

with $\ell_m = \pi w_m^2/\lambda$. The wave equation then reads:

$$\left(\frac{\partial^2}{\partial\xi^2} + \frac{\partial^2}{\partial\eta^2} + \epsilon^2\frac{\partial^2}{\partial\zeta^2} - 4i\frac{\partial}{\partial\zeta}\right)\Psi(\xi,\eta,\zeta) = 0 \tag{2-68}$$

with $\epsilon = \lambda/(\pi w_m)$.

Proceeding as in Reference[100], the solutions of Equation 2-68 are written as a power series of ϵ,

$$\Psi = \sum_{n=0}^{\infty} \epsilon^{2n}\Psi_{2n}.$$

For $\epsilon \ll 1$ one obtains the following set of equations

$$\left(\frac{\partial^2}{\partial\xi^2} + \frac{\partial^2}{\partial\eta^2} - 4i\frac{\partial}{\partial\zeta}\right)\Psi_{2n}(\xi,\eta,\zeta) = \begin{cases} 0 \text{ (if } n = 0), \\ \frac{\partial^2\Psi_{2(n-1)}(\xi,\eta,\zeta)}{\partial\zeta^2}. \end{cases}$$

Polar coordinates are not used because of the transverse elliptical shape of Ψ_0. Whereas the intricate ζ dependence of Ψ_0 makes it difficult to solve this set of equations in the parameter space (ξ, η), its form is simpler in the angular parameters space (k_ξ, k_η)[106]. For the sake of compactness, only the second order of the perturbation series in ϵ is

considered, but the procedure can be extended to any order without difficulty by use of modern computational tools. The Fourier transformed equation for $n = 1$ reads:

$$\left[k_\xi^2 + k_\eta^2 + 4i\frac{\partial}{\partial\zeta}\right]\overline{\Psi}_2(k_\xi, k_\eta, \zeta) = \frac{\partial^2\overline{\Psi}_0(k_\xi, k_\eta, \zeta)}{\partial\zeta^2} \tag{2-69}$$

where

$$\overline{\Psi}_0(k_\xi, k_\eta, \zeta) = \frac{[\det\alpha_0(0)]^{1/4}}{[\det\alpha(0)]^{1/2}}\exp\left(-\frac{1}{2}\Upsilon^T\mu'(z)\Upsilon\right) \tag{2-70}$$

is the Fourier transform of Ψ_0 [106] and where k_ξ and k_η are the dual variables of ξ and η, respectively, $\Upsilon^T = (k_\xi, k_\eta)$ and $\mu'(z) = \mu(z)/w_m^2 = (\alpha^{-1}(0) - i(z/k)I)/w_m^2$. Inserting Equation 2-70 in Equation 2-69 and looking for a solution in the form $\overline{\Psi}_2(k_\xi, k_\eta, \zeta) = Q_2(k_\xi, k_\eta, \zeta)\overline{\Psi}_0(k_\xi, k_\eta, \zeta)$ one obtains a first order partial derivative equation

$$\frac{\partial Q_2(k_\xi, k_\eta, \zeta)}{\partial\zeta} = i\frac{\left(k_\xi^2 + k_\eta^2\right)^2}{64}$$

which gives

$$Q_2(k_\xi, k_\eta, \zeta) = i(k_\xi^2 + k_\eta^2)^2\zeta/64 + P_2(k_\xi, k_\eta)$$

where $P_2(k_\xi, k_\eta)$ is any analytic function of k_ξ and k_η. It is formally equivalent to the solution obtained for circular Gaussian beam [98]. Proceeding as in Reference [98], one arbitrarily restricts the solution space for $P_2(k_\xi, k_\eta)$ to

$$P_2(k_\xi, k_\eta) = C_{2,2,0}k_\xi^4 + C_{2,0,2}k_\eta^4 + C_{2,1,1}k_\xi^2k_\eta^2 + C_{2,1,0}k_\xi^2 + C_{2,0,1}k_\eta^2 \tag{2-71}$$

$C_{2,m,n}$ (m and n are natural integers such that $0 < m + n \leq 2$) are complex constants that depend on boundary conditions. This arbitrary restriction to even and fourth powers in k_ξ, k_η is indeed enough to recover all published second order non-paraxial corrections to circular Gaussian beams [98]. Note that since we are dealing with elliptical beams, powers of k_ξ and k_η are taken independently making it appear three new integration constants with respect to the cylindrically symmetric case. Taking the inverse Fourier transform of $\overline{\Psi}_2$ one obtains:

$$\Psi_2(\mathbf{r}) = \frac{1}{16}\Big\{ i\zeta\Big(4{f_1}^4\tilde{\xi}^4 - 12{f_1}^3\tilde{\xi}^2 + 2f_1f_2(1-2f_2\tilde{\eta}^2) + {f_2}^2(4f_2(f_2\tilde{\eta}^2-3)\tilde{\eta}^2+3) + {f_1}^2(4f_2(2f_2\tilde{\eta}^2-1)\tilde{\xi}^2+3)\Big)$$
$$+ 16C_{2,0,0} + 16\Big(-2{f_2}^2\tilde{\eta}^2 - 4f_1f_2\tilde{\xi}\sin(2\Phi)\tilde{\eta} - 2{f_1}^2\tilde{\xi}^2 + f_1 + f_2 + [-2{f_2}^2\tilde{\eta}^2 + f_2 + f_1(2f_1\tilde{\xi}^2-1)]\cos(2\Phi)\Big)C_{2,0,1}$$
$$+ 8\Big[\Big(3[4{f_1}^4\tilde{\xi}^4 - 12{f_1}^3\tilde{\xi}^2 + 2f_1f_2(1-2f_2\tilde{\eta}^2) + {f_2}^2(4f_2(f_2\tilde{\eta}^2-3)\tilde{\eta}^2+3) + {f_1}^2(4f_2(2f_2\tilde{\eta}^2-1)\tilde{\xi}^2+3)]$$
$$- 4[(4f_1(f_1\tilde{\xi}^2-3)\tilde{\xi}^2+3){f_1}^2 + {f_2}^2(-4f_2(f_2\tilde{\eta}^2-3)\tilde{\eta}^2-3)]\cos(2\Phi) + (4{f_1}^4\tilde{\xi}^4 - 12{f_1}^3\tilde{\xi}^2 + 6f_1f_2(2f_2\tilde{\eta}^2-1) +$$
$${f_2}^2(4f_2(f_2\tilde{\eta}^2-3)\tilde{\eta}^2+3) + 3{f_1}^2(4f_2(1-2f_2\tilde{\eta}^2)\tilde{\xi}^2+1))\cos(4\Phi) + 8f_1f_2\tilde{\eta}\tilde{\xi}[2[f_2(2f_2\tilde{\eta}^2-3) + f_1(2f_1\tilde{\xi}^2-3)]\sin(2\Phi)$$
$$+ (f_2(2f_2\tilde{\eta}^2-3) + f_1(3-2f_1\tilde{\xi}^2))\sin(4\Phi)]\Big)C_{2,0,2} + 2\Big(-2{f_2}^2\tilde{\eta}^2 + 4f_1f_2\tilde{\xi}\sin(2\Phi)\tilde{\eta} - 2{f_1}^2\tilde{\xi}^2 + f_1 + f_2 + [-2{f_1}^2$$
$$\tilde{\xi}^2 + f_1 + f_2(2f_2\tilde{\eta}^2-1)]\cos(2\Phi)\Big)C_{2,1,0} - \cos(4\Phi)\Big(4{f_1}^4\tilde{\xi}^4 - 12{f_1}^3\tilde{\xi}^2 + 6f_1f_2(2f_2\tilde{\eta}^2-1) + {f_2}^2(4f_2(f_2\tilde{\eta}^2-3)\tilde{\eta}^2+3)$$
$$+ 3{f_1}^2(4f_2(1-2f_2\tilde{\eta}^2)\tilde{\xi}^2+1) + 8f_1f_2\tilde{\eta}\tilde{\xi}[f_2(3-2f_2\tilde{\eta}^2) + f_1\sin(4\Phi)(2f_1\tilde{\xi}^2-3)]\Big)(C_{2,1,1} - C_{2,2,0})$$
$$+ \Big(4\cos(2\Phi)(4f_1(f_1\tilde{\xi}^2-3)\tilde{\xi}^2+3){f_1}^2 + {f_2}^2(-4f_2(f_2\tilde{\eta}^2-3)\tilde{\eta}^2-3) + 16f_1f_2\tilde{\eta}\tilde{\xi}\sin(2\Phi)[f_2(3-2f_2\tilde{\eta}^2)$$
$$+ f_1(3-2f_1\tilde{\xi}^2)]\Big)C_{2,2,0} + \Big(4{f_1}^4\tilde{\xi}^4 - 12{f_1}^3\tilde{\xi}^2 + 2f_1f_2(1-2f_2\tilde{\eta}^2) + {f_2}^2(4f_2(f_2\tilde{\eta}^2-3)\tilde{\eta}^2+3) +$$
$${f_1}^2[4f_2(2f_2\tilde{\eta}^2-1)\tilde{\xi}^2+3]\Big)(C_{2,1,1} + 3C_{2,2,0})\Big\}\Psi_0(\mathbf{r}) \tag{2-72}$$

where

$$\begin{pmatrix}\tilde{\xi}\\ \tilde{\eta}\end{pmatrix} = \begin{pmatrix}\cos\Phi & \sin\Phi\\ -\sin\Phi & \cos\Phi\end{pmatrix}\begin{pmatrix}\xi\\ \eta\end{pmatrix}$$

and $f_{1,2} = i/(\zeta + \kappa_{1,2})$ with $\kappa_{1,2} = -\beta_{1,2}/\ell_m + ip_{1,2}/\ell_m$. Assuming a circular Gaussian beam, $w_1 = w_2$, $\Phi = 0$, $\beta_{1,2} = 0$, $p_{1,2} = \pi w_1^2/\lambda$, thus $f_1 = f_2 = i/(i+\zeta) \equiv f$, Eq. 2-72 reduces to Equation (4) of Reference[98].

To further compute Equation 2-72, one must provide numerical values for the coefficients $C_{2,m,n}$. We choose to match Equation 2-71 to some of the axisymetric non-paraxial particular solutions considered in Reference.[98]. The three cases considered below are given in Table 2.2. They correspond to different boundary conditions as explained in References.[98,101]. We also add an extra parameter set, S_4 in Table 2.2, to illustrate the large variety of shapes that can be obtained with Equation 2-72.

Table 2.2 Numerical values used for the integration constants according to different boundary conditions.

Set	$C_{2,0,1}$ $C_{2,1,0}$	$C_{2,0,2}$ $C_{2,2,0}$	$C_{2,1,1}$
S_1 [101]	$1/8$	$-1/64$	$-1/32$
S_2 [100]	$1/4$	$-1/64$	$-1/32$
S_3 [107]	$1/8$	0	0
S_4	0	0	1

2.5.3 Numerical Examples of Non-paraxial Corrections

To illustrate Eq. 2-72, the system of Reference[85], depicted on Figure 2.15, is considered. It is an optical resonator made of two cylindrical mirrors with radius of curvature R and separated by a distance L. The two cylindrical mirror axes are tilted by an angle θ. Formal and compact expressions for the fundamental mode in the paraxial approximation of such a resonator is given in Reference[85]. Here considerable interest is taken in highly elliptical modes possessing a small waist of the order of few wavelengths. To this aim, we choose $\theta = 1.74$ nrad, $R = 0.5$ m and $L = 2R(1-10^{-7})$. For $\lambda = 1.031$ μm the beam radii along the propagation axis z is depicted on Figure 2.16. With this choice of geometrical parameters the cavity mode is highly elliptical and close to the instability point[85]. The minor axis beam size is indeed four orders of magnitude smaller than the major axis, i.e. $w_m = 5.1$ μm, $w_M = 5.4$ cm at $z = 0$. Interestingly, both waists $w_{m,M}$ are located at $z = 0$ and the focus points at $z = \pm L/2$. These results have been further checked using the formalism of Reference[87].

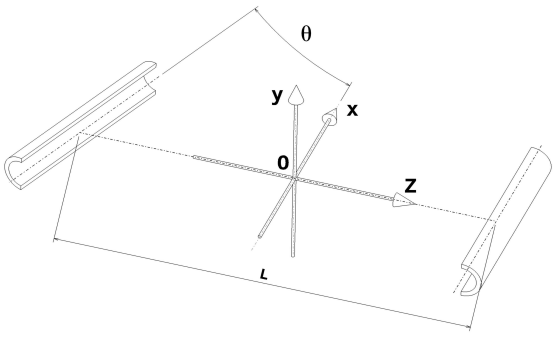

Figure 2.15 Schematic view of the cavity made of two cylindrical mirrors.

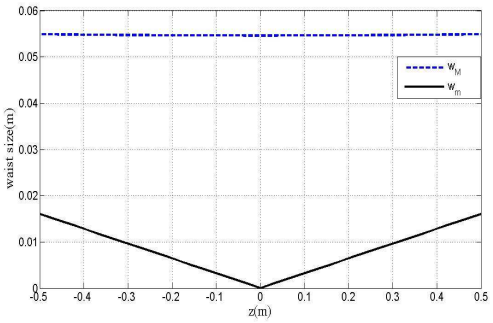

Figure 2.16 Beam radii along the propagation axis z.

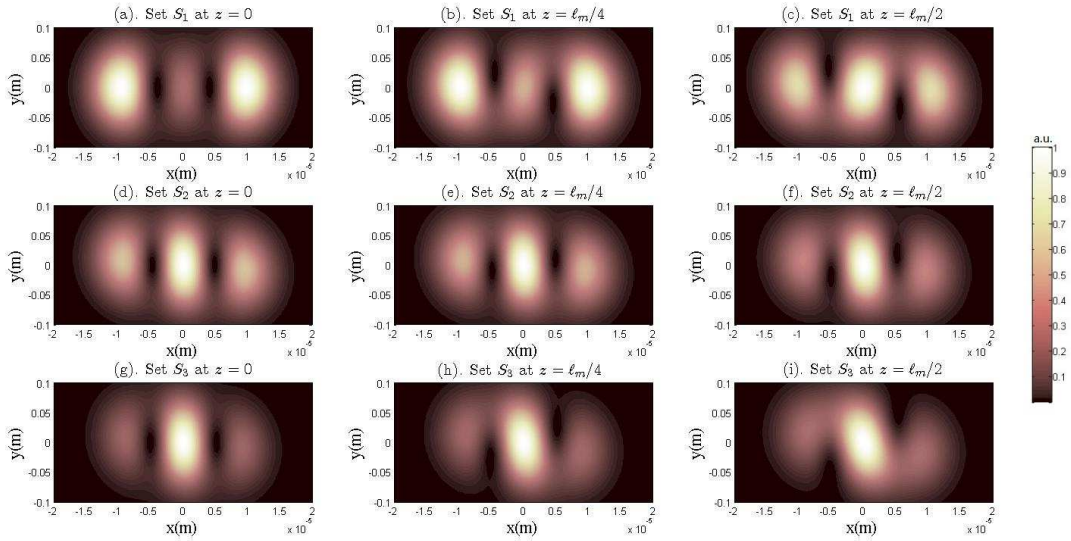

Figure 2.17 Transverse profiles of the second order correction to the paraxial approximation r_2 defined in Eq. 2-73 for parameter sets S_1 at (a) $z = 0$, (b) $z = \ell_m/4$ and (c) $z = \ell_m/2$; S_2 for (d) $z = 0$, (e) $z = \ell_m/4$ and (f) $z = \ell_m/2$; S_3 for (g) $z = 0$, (h) $z = \ell_m/4$ and (i) $z = \ell_m/2$.

The following normalized paraxial and second order non-paraxial beam intensity profiles are defined:

$$r_i(x, y) = \frac{|\Psi_i(x, y)|^2}{\max(|\Psi_i(x, y)|^2)}, (i = 0, 2) \tag{2-73}$$

$r_2(x, y)$ is shown on Figure 2.17 for the three parameters sets S_1, S_2 and S_3 at $z = 0$, $z = \ell_m/4$ and $z = \ell_m/2$. Three maxima are clearly visible and all sets lead to different mode shapes. The central blob contributes less than the other two in set S_1 at $z = 0$, which is contrary to set S_3. The set S_2 presents an intermediate behaviour. However, after propagating up to $z = \ell_m/4$, the central maximum becomes much higher. One sees that an *S-shaped* mode appears as the beam propagates away from $z = 0$ and that it rotates around the propagation axis as expected. A three-dimension view of r_2 is presented on Figure 2.18 by using the parameter sets S_4 at $z = 3\ell_m/4$. The *S-shape* beam can be more clearly observed.

Choices of Table 2.2 for the parameters $C_{i,j,k}$ are arbitrary. Any other reasonable complex value for these parameters also holds. To illustrate the large variety of non-paraxial second order correction shapes that can be obtained we fix $C_{2,1,1} = 1$ and set the other parameters to zero $C_{2,1,0} = C_{2,2,0} = C_{2,0,1} = C_{2,0,2} = 0$ (parameter set S_4 in Table 2.2). The resulting mode shapes are shown on Figure 2.19. This is clearly different from

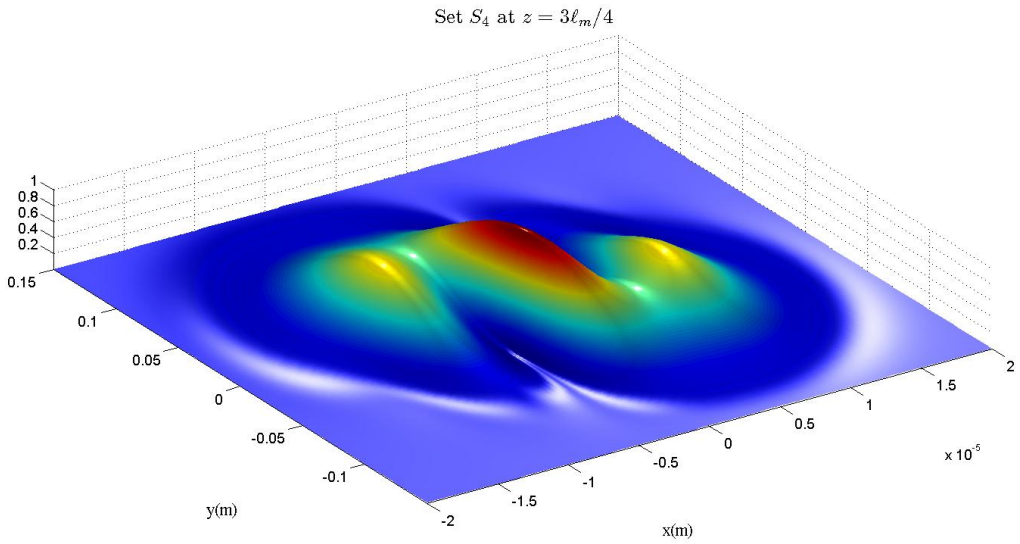

Figure 2.18 r_2 as a function of x and y for parameter sets S_4 at $z = 3\ell_m/4$.

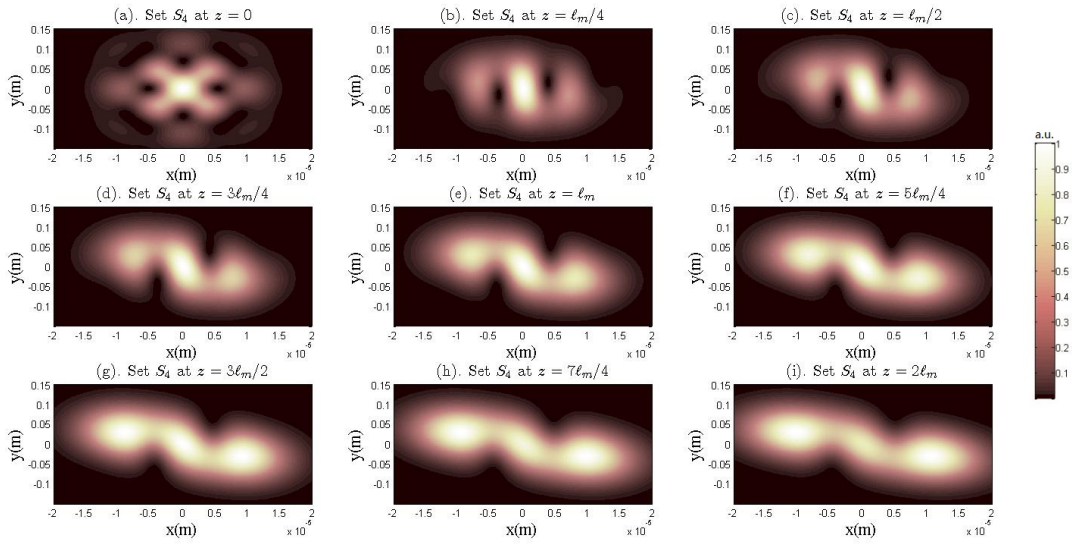

Figure 2.19 Transverse profile of the second order normalized correction quantity r_2 from $z = 0$ to $z = 2\ell_m$. Parameter set S_4 is used for this figure.

what we obtained previously though an *S-shaped* beam is clearly visible for $z > 0$.

r_0 is shown on Figure 2.20 for $L = 0.9$ m, *i.e.* far from the instability region. As expected, no *S-shape* appears, the intensity profiles at fixed values of z are elliptical.

Amazingly, such an *S-shaped* beam mode was indeed observed in a non-planar four-mirror cavity operating close to the instability region[91]. Another observation reported in Reference[91] is that the *S-shape* disappears when the cavity is departing from the instability region. To check that point, the cavity length was changed L down to $1 - 10^{-5}$

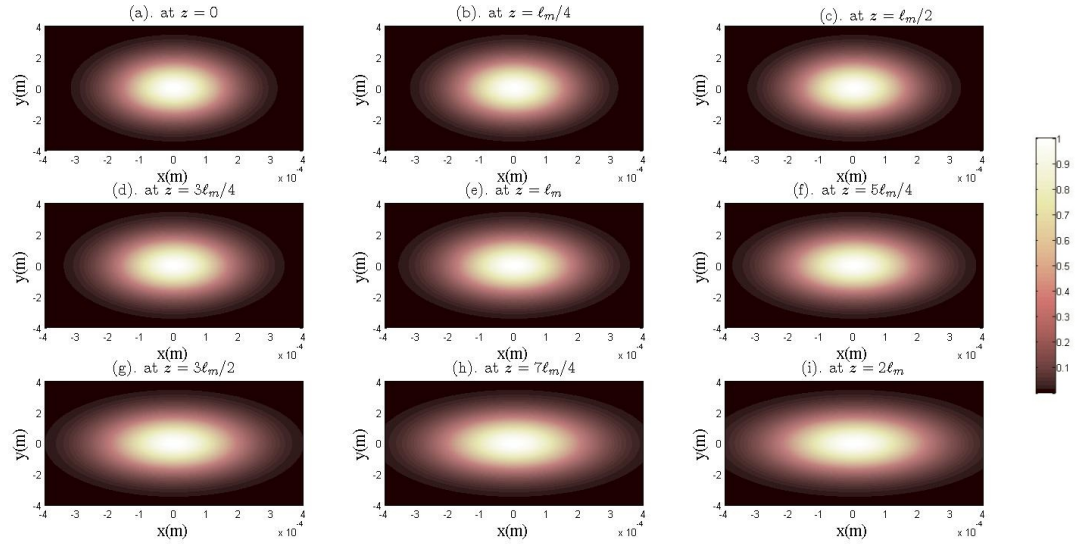

Figure 2.20 r_0 from $z = 0$ to $z = 2\ell_m$ when $L = 0.9$ m.

m, which is relatively far away from the unstable region. The resulting r_2 distributions are shown on Figure 2.21, where one sees that *S-shape* disappears in qualitative agreement with the result of Reference[91]. However, although modes of Reference[91] are general astigmatic beams[88], a quantitative model should include field aberrations induced by the spherical mirrors and other phenomenons such as mode degeneracy[108].

This is outside the scope of this section concentrates on the derivation of the expressions of non-paraxial corrections for general astigmatic beams.

We have solved Lax perturbation series of the wave equation for general elliptic Gaussian beams. Explicit expression for the second order correction was derived. It depends on unknown integration constants which allow to account for arbitrary boundary conditions. Second order corrections are exemplified numerically considering the fundamental paraxial mode of an optical cavity made of two cylindrical mirrors close to its instability point. Varying the values of the integration constants leads to a large variety of transverse shapes due to the second order correction. Remarkably *S*-shaped beam modes appear as the beam propagates away from the cavity symmetry point for various choices of integration constants. This feature agrees qualitatively with Figure 2.14 which was observed on a highly divergent non-planar four-mirror cavity[91].

General astigmatic beams may occur in misaligned four-mirror planar cavity. Therefore testing the model is very important.

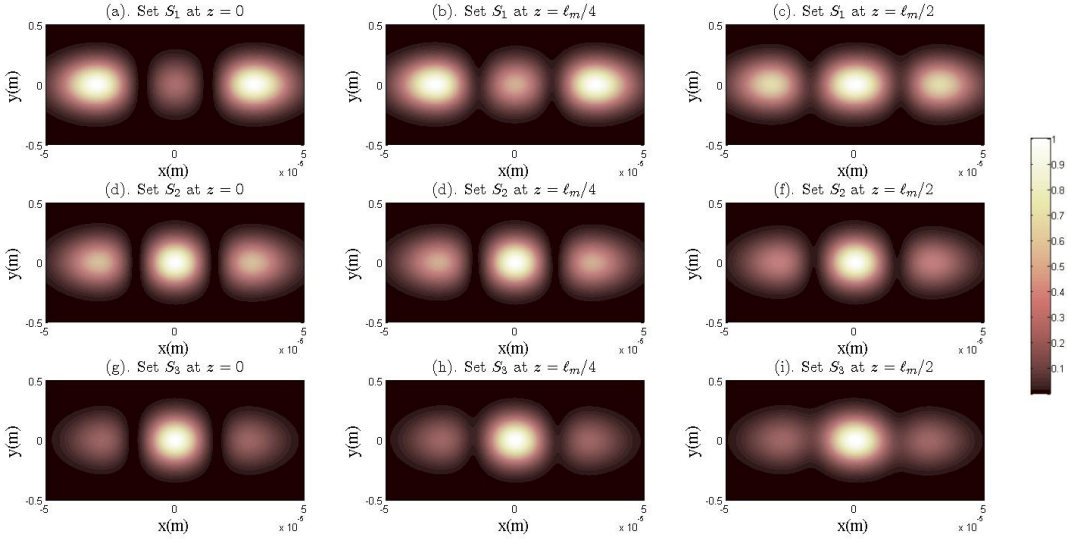

Figure 2.21 r_2 for parameter sets S_1 at (a) $z = 0$, (b) $z = \ell_m/4$ and (c) $z = \ell_m/2$; S_2 for (d) $z = 0$, (e) $z = \ell_m/4$ and (f) $z = \ell_m/2$; S_3 for (g) $z = 0$, (h) $z = \ell_m/4$ and (i) $z = \ell_m/2$.from $z = 0$ to $z = 2\ell_m$ when $L = 1 - 10^{-5}$ m.

Chapter 3 Laser Frequency Stabilization Methods and the Cavity Thermal Effect

To keep the cavity constantly at resonance, a laser frequency stabilization method for locking the laser to the cavity is necessary to compensate for all sources of noise, such as oscillator phase noise and acoustic noise. First, we discuss the measurement of the phase noise and introduce several laser-cavity locking techniques. Once good locking performance is achieved, a cavity thermal effect might be induced by the extremely high power stored in the cavity. To address this phenomenon, a model of the thermal effect and some qualitative calculations are presented.

3.1 Oscillator Phase Noise

Extremely accurate adjustments of the oscillator cavity length are required when a laser is locked to an external cavity, especially for a high-finesse cavity. We have found that the main source of noise is the phase noise of the oscillator. This phase noise leads to the laser field jitter in the oscillator cavity, resulting in fluctuations in the pulse repetition rate. Consider the example of a CW (continuous wave) laser locked at the cavity resonance frequency at Point 1 (marked in red) in Figure 3.1. Because of the fluctuations in the laser frequency caused by the phase noise, the locking point could drop to Point 2 (blue), or even Point 3 (black), which would cause the lock to be lost entirely. Notably, a cavity with a higher finesse will also have a narrower linewidth. For a cavity with a finesse on the order of tens of thousands, the linewidth is on the order of several kHz and is very sensitive to the locking status. Thus, it is necessary to measure the oscillator phase noise.

The phase noise is an arbitrary function added to the field phase term, such as the phase noise ϕ_n of the n-th laser pulse, as expressed in Equation 3-1:

$$e_1(t) = \sum_{n\to-\infty}^{n\to+\infty} B_n \exp\left(i\left(2\pi(nf_{rep} + f_{ce})t + \phi_n(t)\right)\right) \tag{3-1}$$

This phase noise function ϕ_n is not related to $f_{rep}t$. Here, we present a technique for measuring the phase noise of a pulse laser by using a reference.

A CW laser may have a low phase noise because of its relatively simple composition. In our method, therefore, a CW laser is used as the reference. Its electric field is expressed

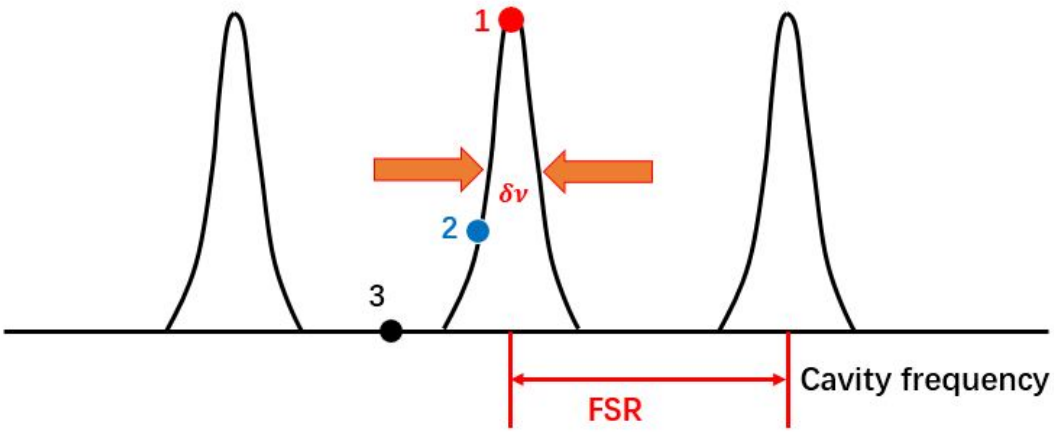

Figure 3.1 Locking points for a CW laser locked to a cavity. Point 1 corresponds to a good lock, whereas Point 2 corresponds to a poor lock because the highest resonance is not reached. The lock is lost entirely at Point 3.

in Equation 3-2:

$$e_2(t) = A \exp\left(i(2\pi \nu_a t + \phi_a)\right) \tag{3-2}$$

where ν_a is the central frequency, ϕ_a is the initial phase, and we assume that $\phi_a = 0$.

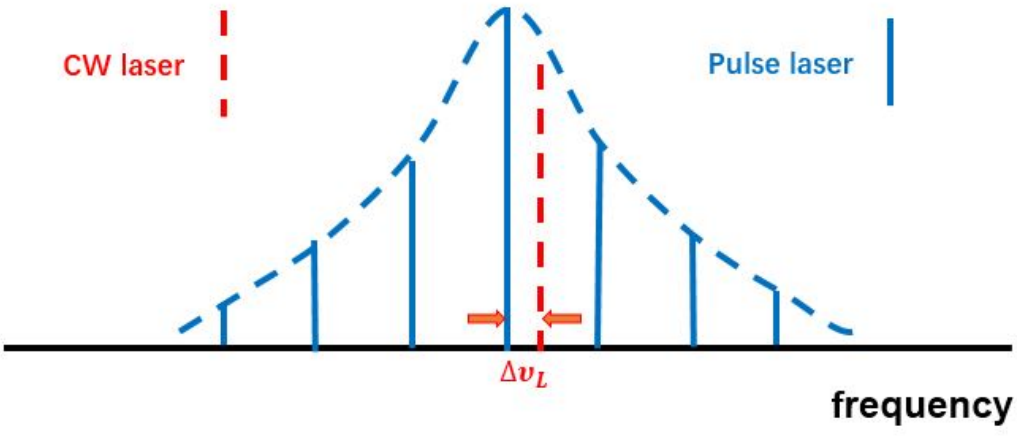

Figure 3.2 Difference $\triangle \nu_L$ between the central frequencies of a CW laser and a pulse laser in the frequency domain.

The two lasers have nearly the same wavelength but a central frequency difference

of $\triangle\nu_L$, as illustrated in Figure 3.2. The beat pattern produced by the field interference is

$$\begin{aligned} P_{AB}(t) =& |e_1(t) + e_2(t)|^2 = |e_1(t)|^2 + |e_2(t)|^2 + 2Re\{e_1(t)e_2(t)\} \\ =& A^2 + \sum_{n,k=-\infty}^{+\infty} B_n B_k \exp\left(i\left(2\pi(n-k)f_{rep}t + \phi_n - \phi_k\right)\right) \\ &+ 2\sum_{n=-\infty}^{n=+\infty} AB_n Re\{\exp\left(i(2\pi(nf_{rep} + f_{ce})t + \phi_n - 2\pi\nu_a t\right)\} \end{aligned} \tag{3-3}$$

We consider $k = n - \triangle k$, $P_A = A^2$, and $P_{Bk} = B_k^2$. $P_{AB}(t)$ simplifies to

$$\begin{aligned} P_{AB}(t) =& P_A + \sum_{k=-\infty}^{+\infty} P_k + 2\sum_{\triangle k>0}\sum_{n=-\infty}^{n=+\infty} B_n B_{n+\triangle k}\cos(2\pi\triangle k f_{rep}t + \phi_{n+\triangle k} - \phi_n) \\ &+ 2\sum_{n=-\infty}^{n=+\infty} AB_n \cos\left(2\pi(nf_{rep} + f_{ce} - \nu_a)t + \phi_n\right) \end{aligned} \tag{3-4}$$

In Equation 3-4, $P_A + \sum_{k=-\infty}^{+\infty} P_k$ is the DC part. $2\sqrt{P_A P_B}\cos\left(2\pi\triangle\nu_L t + \delta\phi_L\right)$ is the lowest-frequency part, and the other terms constitute the high-frequency part. By using a low-pass filter and IQ demodulation, we can extract the spectral density of the phase noise of the pulse laser. The experimental setup is shown in Figure 3.3. Suppose that we wish to measure the phase noise spectral density of an open system, *i.e.*, a free-running laser. The signal after the low-pass filter is so weak that we must utilize a low-noise amplifier to amplify it. The beat pattern and pulse laser frequency comb in the frequency domain can be clearly observed on the spectrum analyzer, as shown in Figure 3.4.

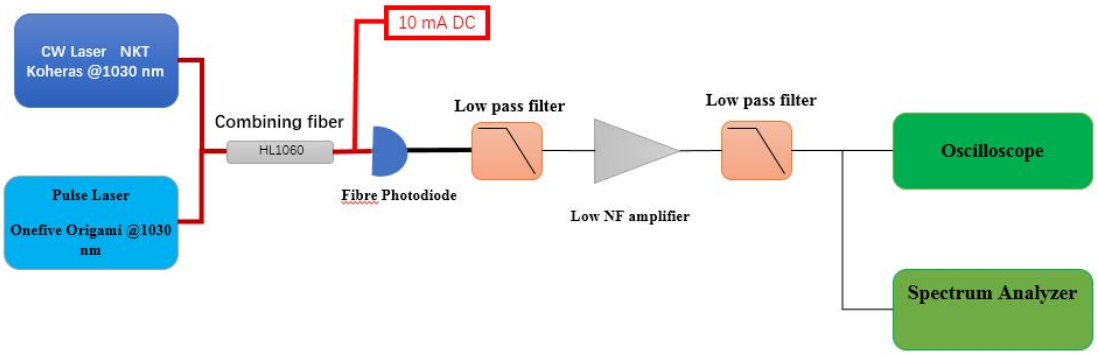

Figure 3.3 Experimental setup for phase noise measurements.

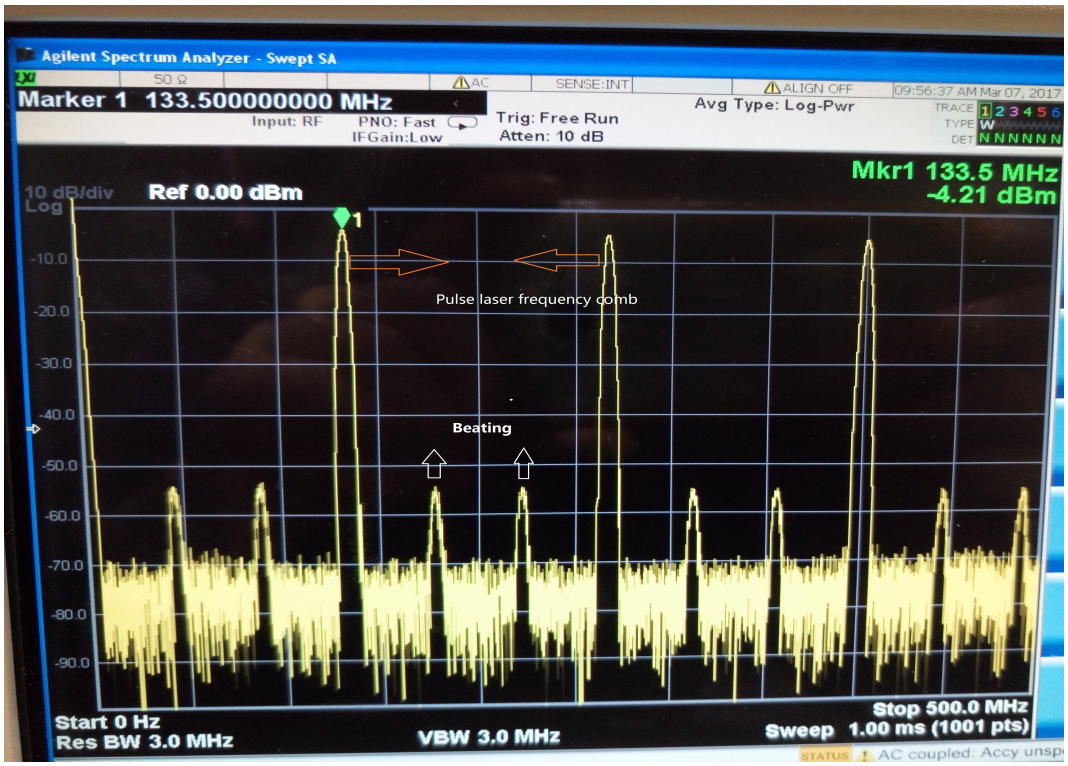

Figure 3.4 The observed beat pattern in the frequency domain. The higher peaks are part of the pulse laser comb. The lower ones correspond to the beat pattern generated by the central frequency difference.

Ultimately, the phase noise spectral density can be measured, as presented in Figure 3.5. This figure shows the result of measuring the phase noise of a Onefive Origami pulse laser, with the optical phase noise of an NKT Koheras CW laser as the reference. The phase noise of the pulse laser follows that of the CW laser until it reaches the thermal noise floor, which is slightly higher than expected, although this can be explained by the fact that the estimation was performed without some of the necessary low-pass filters. These filters introduce some losses, which reduce the power available for the measurement and, consequently, increase the influence of thermal noise on the phase noise.

Simple estimates of the measured phase noise $\delta\phi_L$ and time jitter δt are given by

$$\begin{aligned} \phi_{laser}(t) &= 2\pi\nu_L t + \delta\phi_L = 2\pi\nu_L(t+\delta t) \\ \delta t &= \frac{\delta\phi_L}{2\pi\nu_L} \end{aligned} \tag{3-5}$$

According to Equation 3-5, the time jitter obtained by integrating from 100 Hz to 100 kHz is approximately 31.5 fs, and the jitter from 20 Hz to 5 MHz is 161 fs. In addition,

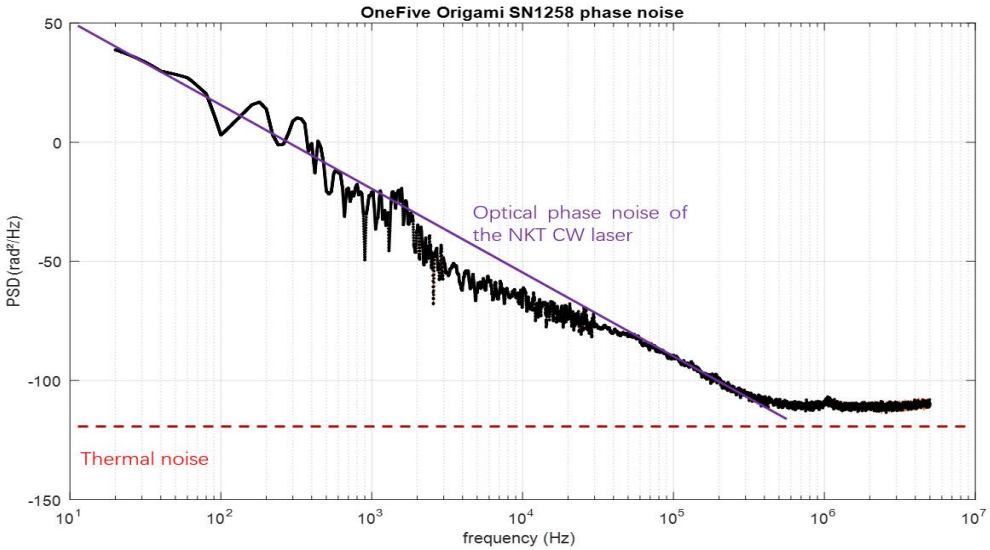

Figure 3.5 Phase noise spectral density of the Onefive Origami pulse laser.

the rms optical frequency shift can be obtained:

$$\delta f_{rep}^{rms} = \sqrt{2\int_0^\infty f^2 L(f)df} \tag{3-6}$$

where $L(f)$ is the power spectral density of a single sideband.

This section describes one method to measure the oscillator phase noise. The oscillator with low phase noise, such as Onefive Origami laser used in our experiments, is rather crucial for a high finesse cavity.

3.2 Locking Methods

Now, we shall discuss the principles of frequency stabilization based on control theory. A schematic diagram of a laser frequency control loop[109] is given in Figure 3.6. The laser, which has frequency noise with a spectral density of S_{laser} expressed in units of $\mathrm{Hz}/\sqrt{\mathrm{Hz}}$, emits a beam at a fixed frequency of ν. A discriminator, which is used to translate frequency fluctuations into voltage signal fluctuations, produces an error signal. The conversion factor is D, expressed in V/Hz. $S_{discri}(f)$ represents the noise spectral density of the discriminator. In fact, the discriminator contains a reference (optical cavity), which helps to produce the error signal. A servo with a gain of $G(f)$ is also applied to amplify the error signal, introducing a noise spectral density of $S_{servo}(f)$. Finally, an actuator with a conversion coefficient of A (expressed in Hz/V) converts the integrated,

amplified signal into frequency fluctuations. Because of the difficulty of distinguishing the noise of the laser from that of the actuator, the actuator noise is included in the laser noise.

The total noise spectral density in the closed loop is derived as the sum of the contributions from all noise sources, as follows:

$$S_{c-loop} = \frac{S^2_{laser+actuator} + |AS_{servo}|^2 + |AGS_{discri}|^2}{|1 + AGD|} \tag{3-7}$$

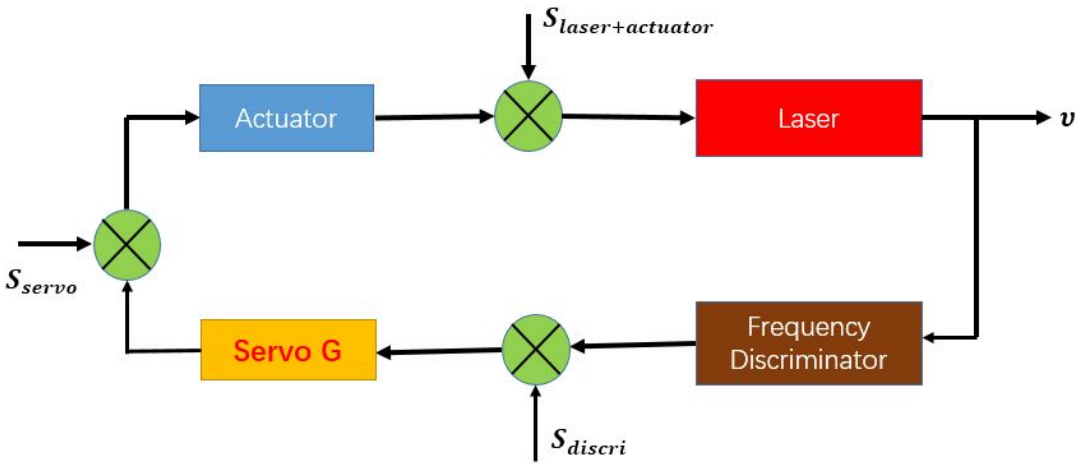

Figure 3.6 Schematic diagram of a laser frequency control loop.

It is interesting to consider a zoomed view of a cavity mode in the frequency domain, as shown in Figure 3.7. The vertical axis is plotted in logarithmic coordinates. For a cavity with a finesse of $F = 30,000$, the ratio between the cavity linewidth $\delta\nu$ and the laser frequency ν is as small as 10^{-11}. Even for a cavity with a finesse of $F = 3,000$, the ratio is 10^{-10}. For this reason, a robust and strong feedback system is truly necessary.

To keep the optical cavity at resonance, an error signal that is proportional to the difference between the cavity resonance frequency and the laser frequency is required. In the following subsections, several techniques for generating such an error signal are discussed.

3.2.1 Pound-Drever-Hall Technique

The most commonly used method for locking a laser to an optical cavity is called the PDH technique[110,111], named after its inventors: Pound, Drever and Hall.

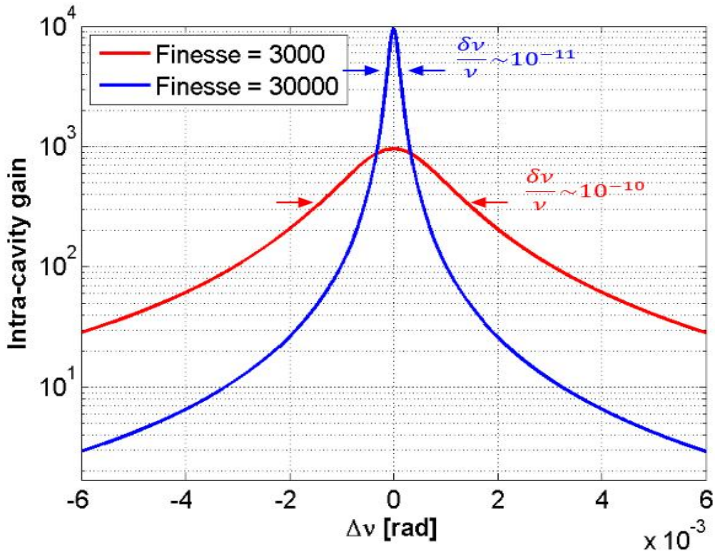

Figure 3.7 Zoomed view of cavity modes for $F = 3,000$ (red) and $F = 30,000$ (blue). This figure is plotted in semilogarithmic coordinates. $\triangle\nu$ is the frequency detuning.

This technique, which is illustrated in Figure 3.8, requires the phase of the incident beam to be modulated at an angular frequency Ω, here achieved by an electro-optical modulator (EOM), and demodulated to the correct phase after reflection from the input mirror of the Fabry-Pérot cavity.

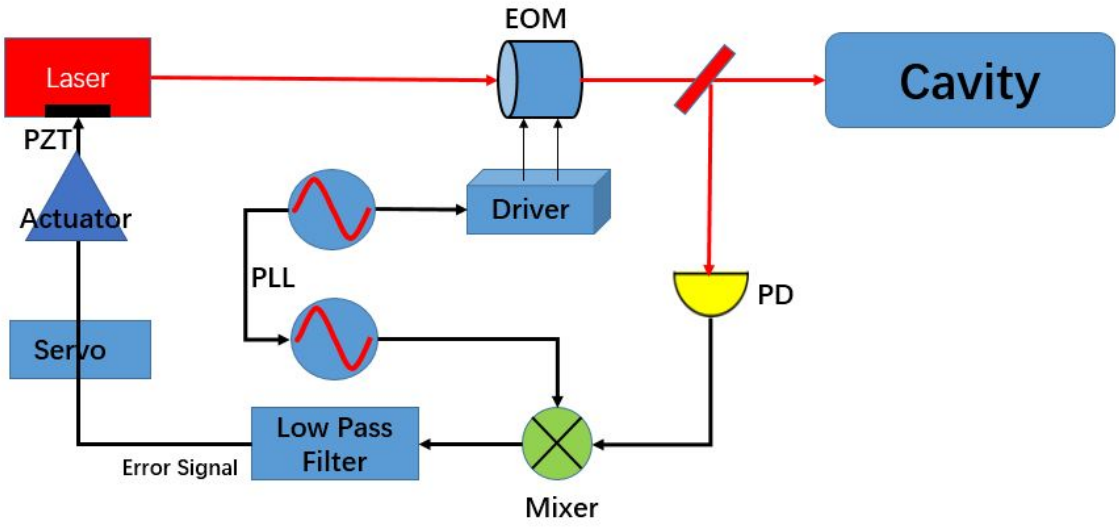

Figure 3.8 Schematic illustration of the PDH technique.

Now, we will describe the PDH technique in detail. The mathematical expression for the incident field after modulation by the EOM is obtained as follows:

$$\begin{aligned} e_{inc} =& e_0 \exp(i\omega t + i\beta \sin(\Omega t)) \\ \approx& e_0 \Big(J_0(\beta) + 2iJ_1(\beta)\sin(\Omega t) \Big) \exp(i\omega t) \\ =& e_0 \Big(J_0(\beta)\exp(i\omega t) + J_1(\beta)\exp(i(\omega+\Omega)t) - J_1(\beta)\exp(i(\omega-\Omega)t) \Big) \end{aligned} \tag{3-8}$$

where β is a small modulation depth, Ω is the demodulation frequency, and J_i $(i = 0, 1)$ is the i-th order Bessel function. In Equation 3-8, we decompose this modulation by using the Bessel series expansion, and we are only interested in the first harmonic. Phase modulation thus makes it possible to generate sidebands of $\omega \pm \Omega$. In practice, a very large modulation depth is needed to generate sidebands beyond the first order.

By using the field reflection coefficient of the cavity, $F(\omega)$, we can write the reflected field as follows:

$$e_{ref} = e_0 \Big[F(\omega)J_0(\beta)\exp(i\omega t) + F(\omega+\Omega)J_1(\beta)\exp(i(\omega+\Omega)t) - F(\omega-\Omega)J_1(\beta)\exp(i(\omega-\Omega)t) \Big] \tag{3-9}$$

The general expression for the field reflection coefficient of an n-mirror cavity is

$$F(\omega) = \frac{-r_1 + (r_1^2 + t_1^2) r_2 \cdots r_n \exp(-i\frac{\omega}{FSR})}{1 - r_1 \cdots r_n \exp(-i\frac{\omega}{FSR})} \tag{3-10}$$

where r_i and t_i are the field reflection and transmission coefficients, respectively, of the i-th mirror.

Suppose that P_0 denotes the total power, $P_c = P_0 J_0^2(\beta)$ represents the power in the carrier wave, and $P_s = P_0 J_1^2(\beta)$ is the power in each sideband. Then, the power measured on the photodiode in Figure 3.8 is given by

$$\begin{aligned} P_{ref} \simeq& P_c |F(\omega)|^2 + P_s \Big[|F(\omega+\Omega)|^2 + |F(\omega-\Omega)|^2 \Big] \\ &+ 2\sqrt{P_c P_s} \Big[Re\{\triangle F(\omega,\Omega)\}\cos(\Omega t) + Im\{\triangle F(\omega,\Omega)\}\sin(\Omega t) \Big] + (2\Omega \text{ terms}) \end{aligned} \tag{3-11}$$

where $\triangle F(\omega,\Omega) = F(\omega)F^*(\omega+\Omega) - F^*(\omega)F(\omega-\Omega)$ corresponds to the interferences between sidebands and $Re\{\cdot\}$ and $Im\{\cdot\}$ denote the real and imaginary parts, respectively, of the quantity enclosed in the curly braces.

The important idea underlying the PDH method is to use a modulation frequency that is not equal to FSR, such that the sidebands will not resonate in the cavity. From Equation 3-10, we obtain

$$F(\omega \pm \Omega) \simeq -1 \tag{3-12}$$

Equation 3-12 has a direct consequence on the function $\triangle F$:

$$\begin{aligned} \triangle F(\omega, \Omega) &= F(\omega)F^*(\omega + \Omega) - F^*(\omega)F(\omega - \Omega) \\ &\simeq F^*(\omega) - F^(\omega) \\ &\simeq -2iIm\{F(\omega)\} \end{aligned} \tag{3-13}$$

Thus, we see that the function $\triangle F$ is almost purely imaginary. This makes it possible to neglect its real part and write the power in the following form:

$$P_{ref} \simeq P_c|F(\omega)|^2 + 2P_s - 4\sqrt{P_c P_s}Im\{F(\omega)\}\sin(\Omega t) + (2\Omega \text{ terms}) \tag{3-14}$$

Finally, to retrieve the imaginary part of the carrier signal, it is necessary to demodulate the signal. The demodulation process consists of using a mixer to multiply the signal by $\sin(\Omega t)$. The mixer generates the product of both of its inputs. Thus, the error signal ϵ is obtained:

$$\epsilon \propto 4\sqrt{P_c P_s}Im\{F(\omega)\} \tag{3-15}$$

If the laser detuning $\delta\omega$ relative to the cavity resonance frequency is small, we can express the carrier frequency ω as

$$\frac{\omega}{FSR} = 2\pi N + \frac{\delta\omega}{FSR} \tag{3-16}$$

By substituting Equation 3-16 into Equation 3-10, we can simplify $F(\omega)$ as follows:

$$F(w) \simeq \frac{i\delta\omega}{\pi\delta\nu} \tag{3-17}$$

where $\delta\nu$ is the cavity linewidth. Hence, the error signal is given by

$$\epsilon \simeq -\frac{4}{\pi}\sqrt{P_c P_s}\frac{\delta\omega}{\delta\nu} \tag{3-18}$$

This means that the error signal is linear in the detuning $\delta\omega$ near the resonance. This is precisely what we want. The error signal is plotted as a function of the detuning in Figure 3.9. The error signal is linear near the resonance and crosses zero at zero detuning. At present, the PDH method is widely used in many fields, such as gravity wave detection, because of its stable and outstanding performance.

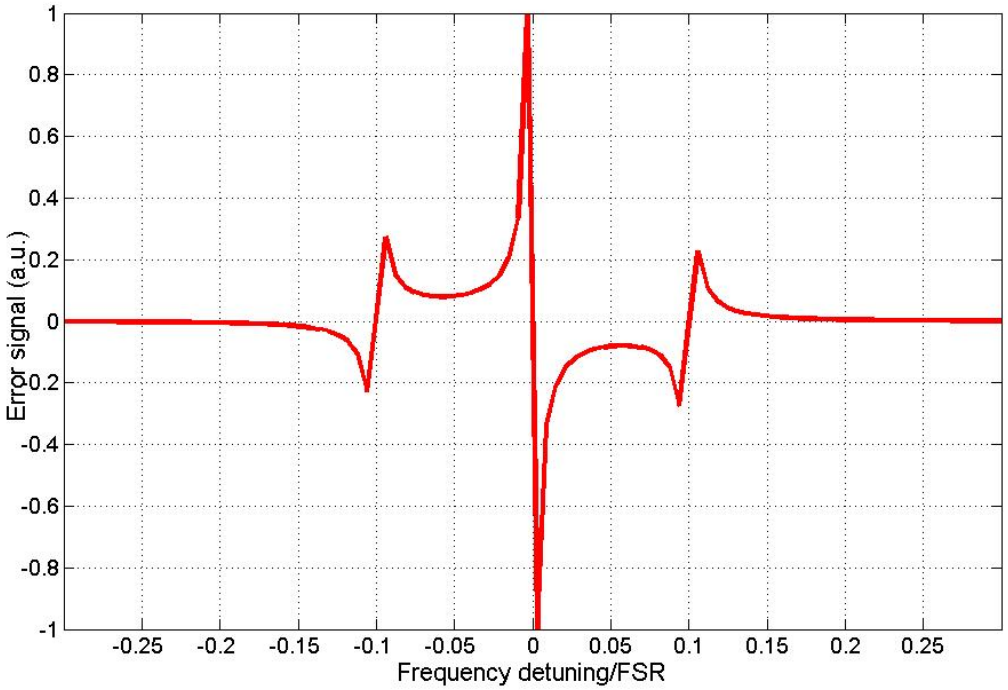

Figure 3.9 The PDH error signal as a function of $\delta\omega/FSR$. We consider a modulation frequency of $\Omega = 20$ MHz, $FSR = 200$ MHz, and $r_1^2 = r_2^2 = 0.99975$.

3.2.2 Tilt Locking

Tilt locking, which was proposed by Grey in 1999[112], utilizes the interference between the carrier field and a directly reflected phase reference. Instead of electro-optic frequency modulation and demodulation, tilt locking makes use of the coding and decoding of optical spatial modes.

A reference beam, such as a TEM_{01} or TEM_{10} beam, which interferes with the carrier beam at a split photodiode, is generated by the misalignment of the input beam. In addition, the adaptation between the input beam waist and the cavity waist leads to the generation of an even mode. This also could be used to generate an error signal, as proposed in Shaddock's thesis[113]. In the tilt locking technique, the phase of the TEM_{10} or TEM_{01} mode acts as a stable reference. In the ideal case, the off-resonance mode will be completely reflected by the cavity when the TEM_{00} beam is in resonance with the Fabry-Pérot cavity. The error signal is produced by the interference of the two modes at a split photodiode, which subtracts the two contributions, as presented in Figure 3.10[114]. In this figure, **Diff** is an abbreviation for the difference in the intensities of the TEM_{00} and TEM_{01} modes.

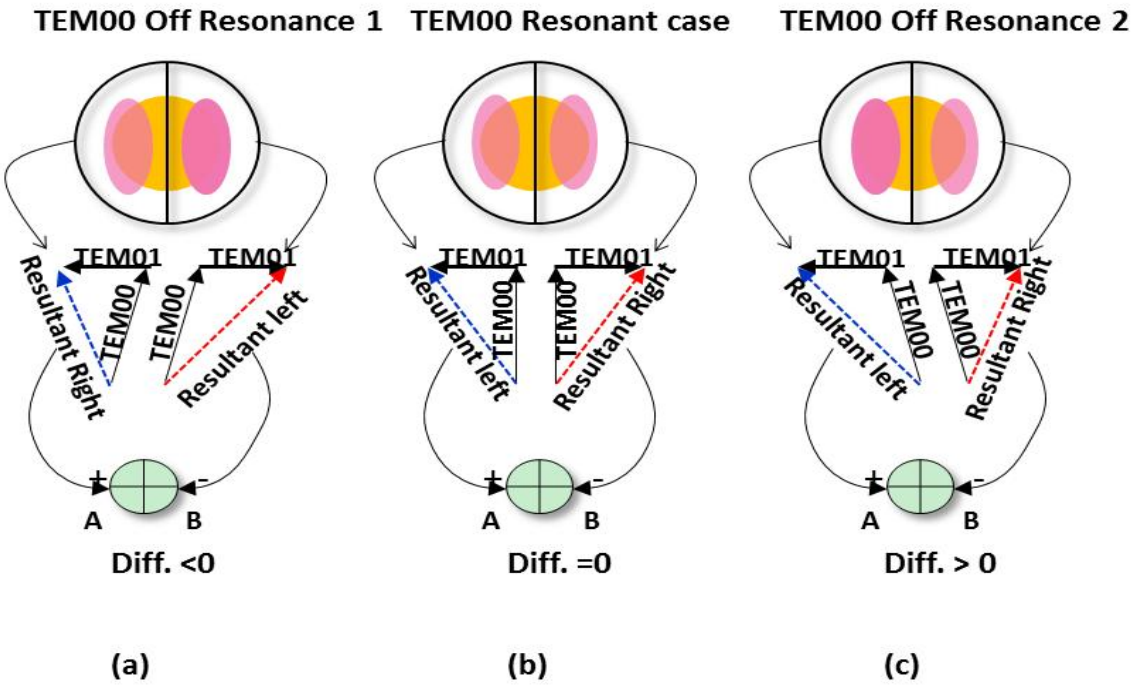

Figure 3.10 Overlap of TEM_{00} and TEM_{10} modes at a split photodiode and the vector superposition of the electric fields: (a) off resonance, Diff < 0; (b) on resonance, Diff > 0; and (c) off resonance, Diff > 0[114].

This kind of interference is influenced by the difference between the phases of the two modes. When the reflected beam from the cavity is focused on the split photodiode, the TEM_{10} mode on the left-hand side has a positive phase, whereas it has a negative phase on the right. The TEM_{00} mode, however, has a completely symmetric and nearly

identical phase. When the TEM_{00} mode is resonant with the cavity, the combined intensity difference is zero, as shown in Figure 3.10(b).

Compared with the PDH technique, tilt locking does not require electro-optic modulation or demodulation and has a simpler setup. However, it is very difficult to achieve proper alignment for tilt locking, and the method is very sensitive to the beam alignment[114].

3.2.3 Other Locking Techniques

Hänsch-Couillaud Locking

Hänsch-Couillaud locking[115] is an elegant and simple method that uses a birefringent cavity. The cavity is made birefringent by inserting a polarizing element, such as a linear polarizer or a Brewster plate. The reflected light becomes a frequency-dependent elliptically polarized beam and passes through a $\lambda/4$ waveplate and a polarizing beam splitter (PBS). The error signal is extracted by analyzing the polarization.

However, the feasibility of the Hänsch-Couillaud locking technique is limited. It is not useful for high-finesse cavities because the inserted element causes additional losses. In addition, the complexity and instability of this technique also hinder its broader use. In recent years, several simpler methods using birefringent cavities have been proposed[116,117].

Honda Locking

Another frequency stabilization method, this one designed especially for non-planar optical cavities, was proposed by Honda[118]. It is a variant of the Hänsch-Couillaud locking technique[115] that does not require the addition of polarizing elements.

This scheme uses a characteristic property of non-planar optical cavities: an additional geometric phase arising from the degenerate splitting of a three-dimensional cavity. A differential signal that can be used for locking is produced by means of a simple setup consisting of a PBS and photodiodes.

3.3 Cavity Polarization Locking

A new method of laser frequency stabilization using polarization property of an optical cavity has been developed in the context of this thesis[119]. In a standard Fabry-Perot cavity, the coating layers thickness of cavity mirrors is calculated to obtain the same phase shift for s- and p-wave but a slight detuning from the nominal thickness can produce

s- and p-wave phase detuning. A tiny change of the coating layer thickness of the cavity mirrors leads to s- and p-wave phase detuning. In the same way, if the incidence angle of cavity mirror is different from the nominal one for which the coating has been optimized, s- and p-wave also exhibit different phase shifts although the cavity is made of an even number of mirrors[88]. As a result, s- and p-wave accumulate a different phase after one round-trip in the cavity, *i.e.* they resonate at different frequencies. In this part, a new method is proposed to implement a simple error signal by using this polarization property.

3.3.1 Phase Detuning of Cavity Mirrors

The phase shift difference between s- and p-wave can be controlled by adjusting the last layer of a quarter-wave layers stack like $(HL)^{\mathrm{N}}HL_{\alpha}$, where H is a high index quarter-wave layer (e.g. Ta_2O_5), L is a low index quarter-wave layer (e.g. SiO_2), N is the number of periods, and L_{α} is the special tuning layer where α is the tuning coefficient of the last coating thickness. The matrix theory developed in Ref.[120] allows to compute the normalized electric and magnetic fields **B** and **C** at the front surface of the multilayer and parallel to it. All the optical properties can be deduced from these two quantities.

The characteristic matrix of a non-absorbing layer with refraction index n and a thickness e is defined by

$$R(\delta,\eta)=\begin{pmatrix}\cos\delta & i\sin\delta/\eta\\ i\eta sin\delta & \cos\delta\end{pmatrix} \tag{3-19}$$

where $\delta = 2\pi ne\cos\theta/\lambda$, $\theta = \arcsin(\sin\theta_0/n)$, θ_0 is the angle of incidence in vacuum, η is the optical admittance given by $\eta = \eta_0 n\cos\theta$ or $\eta = \eta_0 n/\cos\theta$ for s- and p-wave respectively, and $\eta_0 = \sqrt{\varepsilon_0/\mu_0}$ is the vacuum admittance. The dependence of η with polarization comes from different boundary conditions for **B** and **C** at the interface in both polarization planes.

A multilayer stack can be represented by an equivalent surface with an admittance Y given by

$$Y=\frac{||\mathbf{C}||}{||\mathbf{B}||} \tag{3-20}$$

$$\begin{pmatrix} B \\ C \end{pmatrix} = R(\delta'_L, \eta_L) R(\frac{\pi}{2}, \eta_H) \left[R(\frac{\pi}{2}, \eta_L) R(\frac{\pi}{2}, \eta_H) \right]^{\mathrm{N}} \begin{pmatrix} 1 \\ \eta_{sub} \end{pmatrix}. \tag{3-21}$$

The subscripts H, L and sub stand for high index material, low index material and the substrate respectively. The first matrix is the characteristic matrix of the tuned layer, for which $\delta'_L = \alpha\pi/2$, the second matrix is for the last high index quarter-wave layer and the last one is for N periods of quarter-wave layers (HL).

The amplitude reflection coefficient is calculated from: $r = (\eta_0 - Y)/(\eta_0 + Y)$. Thus, the phase shift on reflection can be deduced from

$$\tan\varphi = \frac{Im(r)}{Re(r)} \tag{3-22}$$

where:

$$Im(r) = -2\cos\delta'_L \sin\delta'_L \eta_0 [\eta^2_{sub}\eta_L/\eta^2_H(\eta_L/\eta_H)^{2\mathrm{N}} - \eta^2_H/\eta_L(\eta_H/\eta_L)^{2\mathrm{N}}] \tag{3-23}$$

and

$$\begin{aligned} Re(r) = \eta^2_0 [&\sin^2\delta'_L \eta^2_H/\eta^2_L(\eta_H/\eta_L)^{2\mathrm{N}} + \cos^2\delta'_L \times \eta^2_{sub}/\eta^2_H(\eta_L/\eta_H)^{2\mathrm{N}}] \\ &- \cos^2\delta'_L \eta^2_H(\eta_H/\eta_L)^{2\mathrm{N}} - \sin^2\delta'_L \eta^2_{sub}(\eta_H/\eta_L)^{2(\mathrm{N}+1)} \end{aligned} \tag{3-24}$$

For high reflective coating with a large number of periods N (*i.e.* $N > 10$), Equation 3-22 reads

$$\varphi \simeq \arctan\left(\frac{2\eta_{air}/\eta_L \cos\delta'_L \sin\delta'_L}{\eta^2_{air}/\eta^2_L \sin^2\delta'_L - \cos^2\delta'_L} \right) \tag{3-25}$$

In this case, the phase shift depends only on the tuned layer phase factor δ'_L and optical admittance η_L. Unlike the former, the latter depends on the polarization plane, thus inducing different phase shifts on reflection for both polarizations. The phase shift difference is given as function of the tuning parameter α in Figure 3.11. Phase shift differences up to ± 3.5 mrad can be achieved with α=0.62 or 1.38. The effect of the birefringence was simulated using the model of Ref. [121] and found that it did not change significantly the curve of Figure 3.11. Influence of thermal increase of the coatings on

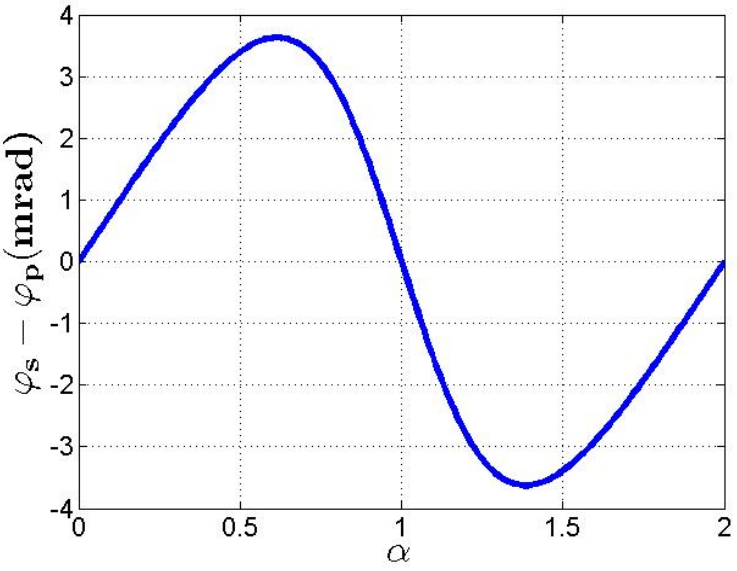

Figure 3.11 Difference between the s- and p-wave reflection phase shifts ($\varphi_s - \varphi_p$) as function of the tuning coefficient α of the first layer.

the phase shift difference was simulated and found to be of the order of 7.5×10^{-6} rad/K. This effect can thus be neglected.

This technique has been used to design the coating of the four-mirror planar bow-tie cavity in Section 3.3.2.

3.3.2 Stabilization method

This section concentrates on four-mirror planar cavities, but the method can be extended for other topologies of cavities. The complex reflection coefficient for s- and p-wave in the basis attached to the incidence plane of mirror i reads[88] $r_{is,p} = \rho_{is,p}\exp(i\varphi_{is,p})$ where $\rho_{is,p}$ and $\varphi_{is,p}(i \in [1,4])$ are the amplitude and phase shift of the reflection coefficient for s- and p-waves of the ith mirror. The Jones vector circulating in the cavity is[88]

$$\mathbf{V}_{circ} = \begin{pmatrix} \frac{t_{1s}}{1-\xi_s \exp(i\Psi_s)} & 0 \\ 0 & \frac{t_{1p}}{1-\xi_p \exp(i\Psi_p)} \end{pmatrix} \mathbf{V}_0 \tag{3-26}$$

where $t_{1s,p}$ are the transmission factors of the input mirror for both s- and p-wave; $\xi_{s,p} = \rho_{1s,p}\rho_{2s,p}\rho_{3s,p}\rho_{4s,p}$, and $\Psi_{s,p} = \varphi_{1s,p} + \varphi_{2s,p} + \varphi_{3s,p} + \varphi_{4s,p} + \varphi_{space}$, with φ_{space} the spatial propagation phase shift, $\mathbf{V_0}^{\mathrm{T}} = (V_{0s}, V_{0p})$ normalized to 1 is the incident Jones vector of

Table 3.1 Parameters of cavity mirrors

Mirror	M1	M2	M3	M4
Diffusion(ppm)	2	2.5	2	3
Absorption(ppm)	1	0.68	0.62	0.64
Transmission(ppm)	1060	410	334	375
Nominal φ(rad)	$\pi - 0.0018$	$\pi - 0.0028$	$\pi - 0.0028$	$\pi - 0.0028$

polarization. The intensity circulating in the cavity is

$$\frac{I_{circ}}{I_{in}} = \left| \frac{t_{1s}}{1 - \xi_s \exp(i\Psi_s)} V_{0s} \right|^2 + \left| \frac{t_{1p}}{1 - \xi_p \exp(i\Psi_p)} V_{0p} \right|^2. \tag{3-27}$$

where $t_{1s,p}$ are the transmission factors of the input mirror for both s- and p-wave; $\xi_{s,p} = \rho_{1s,p}\rho_{2s,p}\rho_{3s,p}\rho_{4s,p}$, and $\Psi_{s,p} = \varphi_{1s,p} + \varphi_{2s,p} + \varphi_{3s,p} + \varphi_{4s,p} + \varphi_{space}$, with φ_{space} the spatial propagation phase shift, ${\mathbf{V}_0}^{\mathrm{T}} = (V_{0s}, V_{0p})$ normalized to 1 is the incident Jones vector of polarization. The intensity circulating in the cavity is

$$\frac{I_{circ}}{I_{in}} = \left| \frac{t_{1s}}{1 - \xi_s \exp(i\Psi_s)} V_{0s} \right|^2 + \left| \frac{t_{1p}}{1 - \xi_p \exp(i\Psi_p)} V_{0p} \right|^2. \tag{3-28}$$

Ignoring the losses in the cavity, the complex amplitude of the reflected wave is[115,122]

$$\begin{aligned} {e^{\mathrm{r}}}_{s,p} &= {e^{\mathrm{i}}}_{s,p} \left[\sqrt{R_1} - \frac{T_1}{\sqrt{R_1}} \frac{R \exp(i\Psi_{s,p})}{1 - R \exp(i\Psi_{s,p})} \right] \\ &\equiv {e^{\mathrm{i}}}_{s,p} F(\Psi_{s,p}) \end{aligned} \tag{3-29}$$

where R_1 and T_1 are the reflectivity and transmission of the cavity input mirror, $R = \sqrt{R_1 R_2 R_3 R_4}$ is the cavity effective reflection coefficient, and Ψ is the total phase shift after one cavity round-trip different for s- and p-wave.

The proposed procedure is demonstrated on a four-mirror planar bow-tie cavity made of two planar mirror (M1 and M2) and two spherical mirror (M3 and M4) shown in Figure 3.13. M1 also acts as the coupling mirror. The mirror coating design has been done according to Section 3.3.1. For each mirror the tuning coefficient α has been adjusted to provide an optimal coupling and a finesse 3000. As a result, a round-trip phase shift is induced.

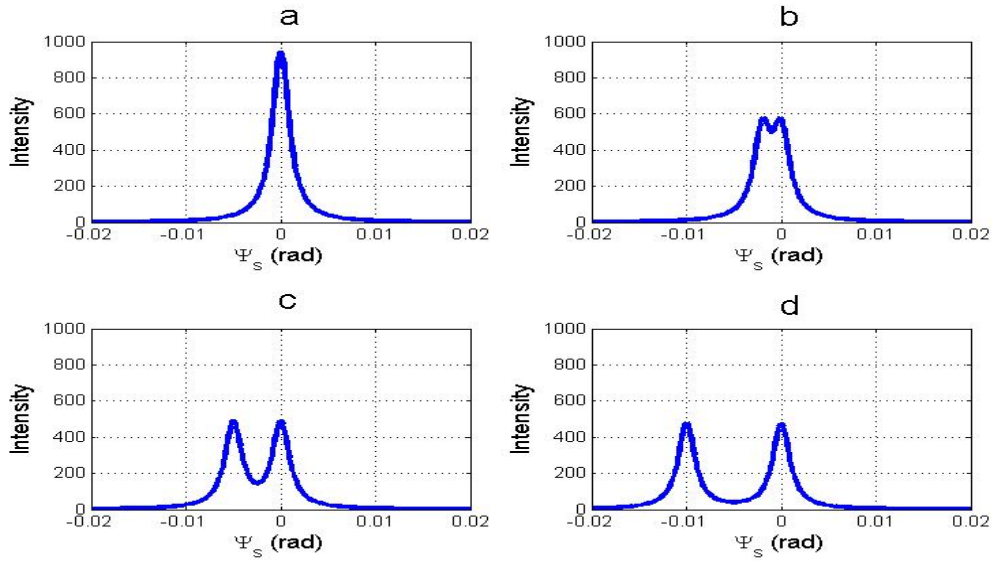

Figure 3.12 Calculated cavity circulating intensity as a function of Ψ_s. The four plots corresponds respectively to $\Psi_s - \Psi_p$= (a)0 mrad, (b)2 mrad, (c)5 mrad, (d)10 mrad.

Parameters of the mirrors are presented in Table 3.1. Nominal φ is the design phase shift in reflection between s- and p-wave. The total phase shift difference $\Psi_s - \Psi_p$ for s- and p-wave approximates 10 mrad. The cavity is 1.68 m long. The circulating intensity as a function of Ψ_s is shown on Fig 3.12 for various values of $\Psi_s - \Psi_p$. Two polarization peaks are observed when the phase difference is larger than 2 mrad.

In our design (see Figure 3.13) a quarter wave plate and a polarizing beam splitter (PBS) are placed in the reflection path of the input mirror. The quarter wave plate in Figure 3.13 is rotated so that the angle between the fast axis of assembly and the optical table is 45 degrees. The difference of the two polarization intensities obtained from reflection and transmission of the PBS acts as an error signal used for the feedback system.

A linear polarization rotated at 45 degrees is used as injection such that the reflection field reads

$$\mathbf{e}^{\mathrm{r}} \propto \begin{pmatrix} F(\Psi_p) + e^{-i\frac{\pi}{2}} F(\Psi_s) \\ e^{-i\frac{\pi}{2}} F(\Psi_p) + F(\Psi_s) \end{pmatrix} \equiv \begin{pmatrix} {e_p}^{\mathrm{r}} \\ {e_s}^{\mathrm{r}} \end{pmatrix} \tag{3-30}$$

where F is the reflection amplitude of the optical cavity defined in Equation 3-29. The signal $|{e_s}^{\mathrm{r}}|^2 - |{e_p}^{\mathrm{r}}|^2$ crosses zero at the maximum of the resonance peaks as shown in Figure 3.14. By choosing the sign of the slope of the error signal, one can select different

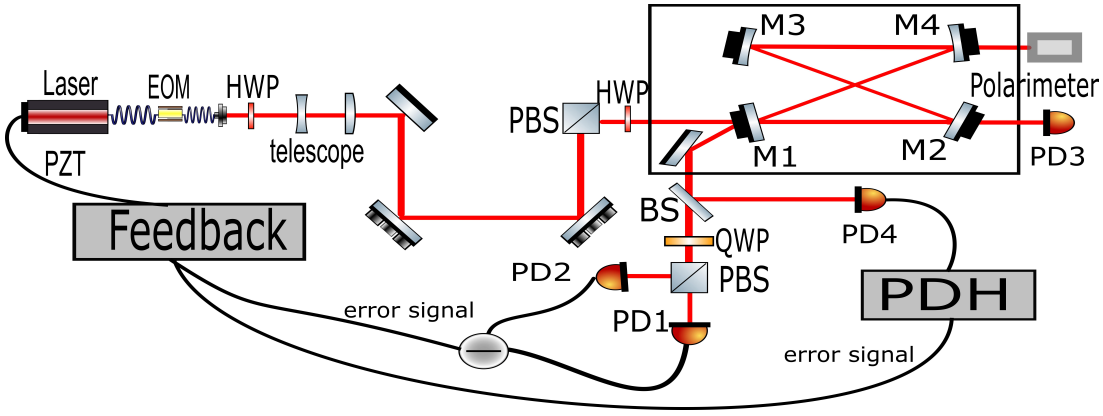

Figure 3.13 Experiment setup. M1, M2, M3 and M4 are the Fabry-Perot cavity mirrors. PD1, PD2, PD3 and PD4 are photodiodes. EOM is an electro-optic modulator. HWP is a half-wave plate. QWP is a quarter wave-plate. PBS is a polarizing beam splitter. BS is a beam splitter.

polarization peaks. The slope of the error signal,

$$K = \frac{\partial(|e_s{}^r|^2 - |e_p{}^r|^2)}{\partial \Psi_s}|_{\Psi_s=0} \tag{3-31}$$

is maximized when $\Psi_s - \Psi_p = \pi$. However, the value of the slope is equal to 99% of its maximum as soon as $|\Psi_s - \Psi_p| > 10$ mrad. We estimate the variation of the phase shift due to the thermal effect in a zero-order QWP accounting for the change of the refractive indices and thickness with temperature to be of 3×10^{-3} rad/K. Thus only in presence of very large (~100 K) temperature increase of the QWP, which is judged to be unlikely, a sensible effect on the error signal would be noticeable. However, this error signal was simulated and found to be not much distorted so that it can still be used to lock the cavity.

3.3.3 Experiment

An experiment was made to test this method as shown in Figure 3.13. The pulsed laser used in the experiment is the Menlo Orange Yb Laser with 178.5 MHz repetition rate and about 8 nm linewidth at 1030 nm central wavelength. A half-wave plate is placed upstream the injection in the cavity to produce a linearly polarized laser beam and balance the s- and p-wave intensities. The transmission intensity is monitored by

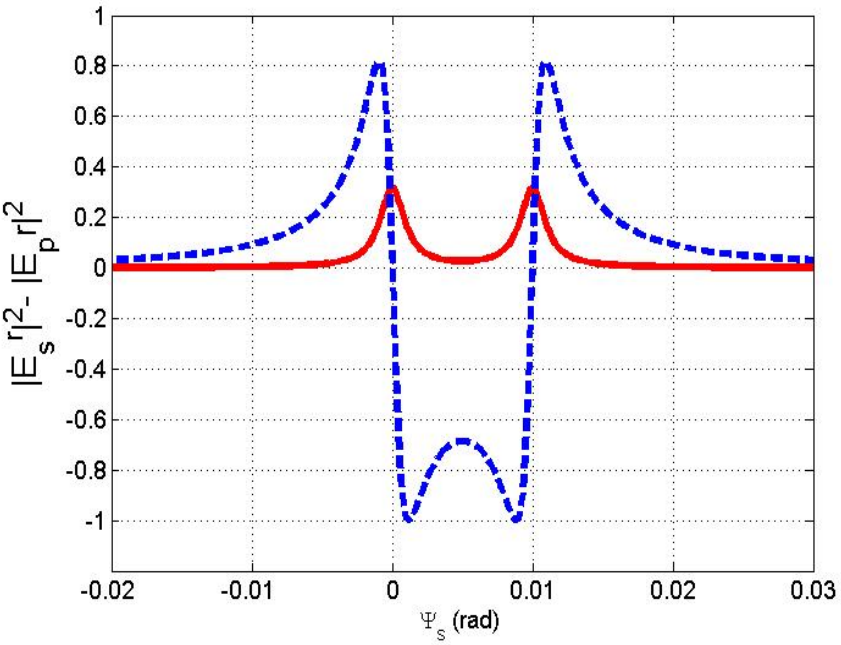

Figure 3.14 Calculated intensities of the cavity resonance peaks (solid line) and error signal (dashed line).

the photodiode PD3. The cavity reflected field is directed onto a beamsplitter. Half of the intensity is measured by the photodiode PD4 used in the PDH technique. The other half of the intensity goes through a quarter wave-plate rotated at 45 degrees and a PBS separates the two polarization states. The intensities of these two beams are measured by the photodiodes PD1 and PD2. Their output is amplified in a differential amplifier which produces the error signal for the feedback. The experimental error signal is shown in Figure 3.15, in good qualitative agreement with calculations of Section 3.3.2. Two separated peaks are seen on the transmitted signal during laser frequency scan. The noise of the signals just comes from the pulsed laser phase noise alone. This error signal was used to successfully lock the laser on the cavity as shown in Figure 3.16. The bottom black curve is the voltage applied to the piezo electric transducer (PZT) of the laser cavity to adjust the frequency. In this case, the residual noise is effectively due to limited bandwidth of the PZT actuator. A good stability was observed for several hours. During the lock, the polarization of the light in transmission of M4 is measured with a polarimeter. In this case, alternance between horizontal and vertical polarizations is observed after a simple sign inversion of the feedback gain of the loop. In both cases the degree of linear polarization is larger than 99.5%.

Different s- and p-wave intensities can be injected in the cavity by rotating the input

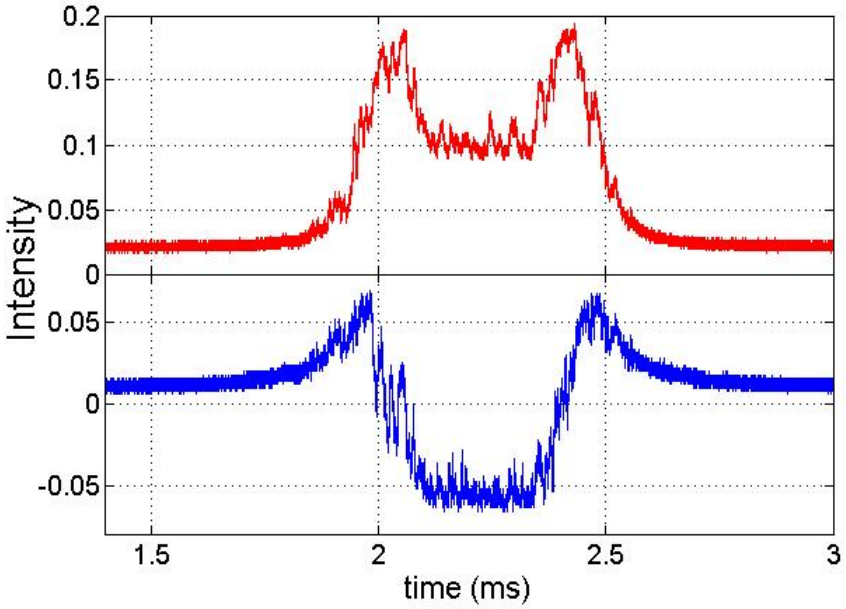

Figure 3.15 Experimental measurement. When PZT of the laser is adjusting the frequency, the intensity of transmission (top red curve) and error signal (bottom blue curve) are obtained.

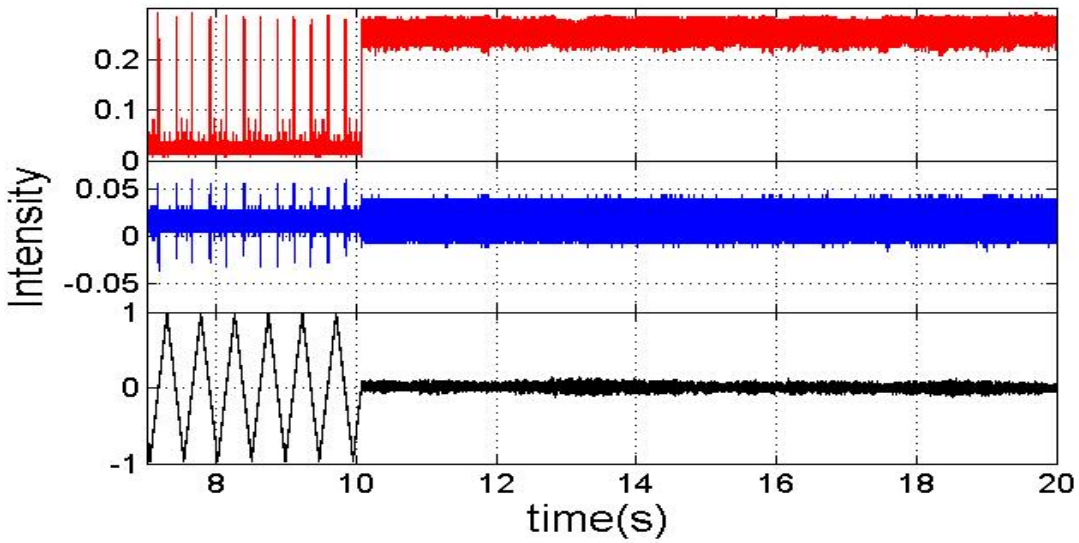

Figure 3.16 Experimental measurements of transmission (top red curve), error (middle blue curve), and PZT signals (bottom black curve) evolution over 20 s. Lock starts at 10 s.

half-wave plate. The possibility to have asymmetric amplitudes is crucial to reduce the power loss induced by the second polarization circulating in the cavity. The lock is still successful even though one peak is much smaller than the other one as shown in Figure 3.17. During the experiment, it is necessary to balance the error signal to zero by rotating the quarter waveplate. The lock is very sensitive to the rotation. This locking method is

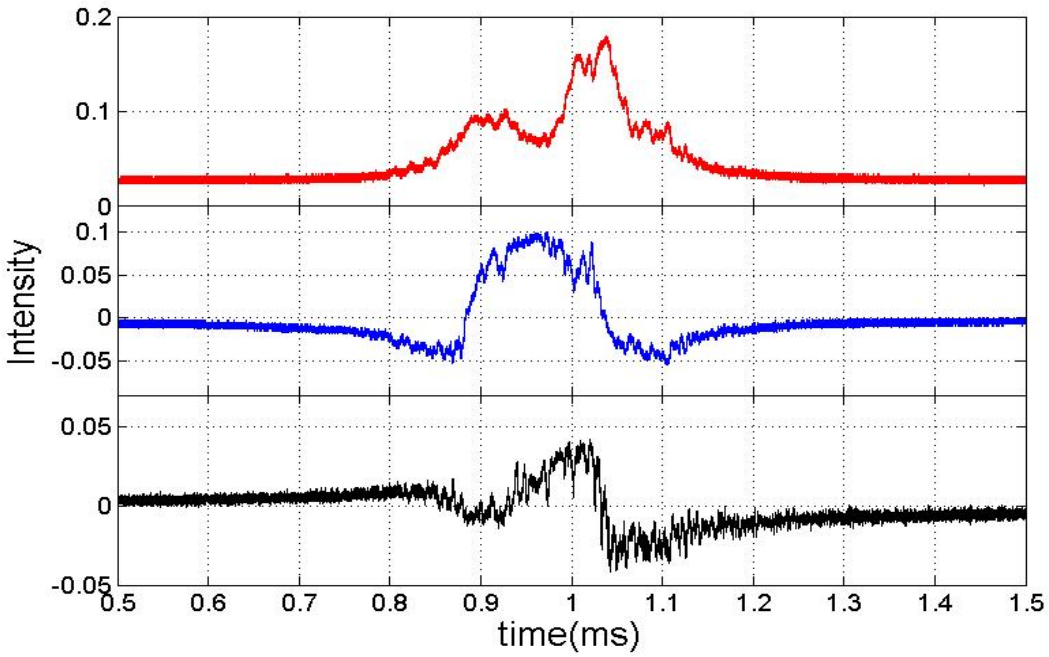

Figure 3.17 Experimental polarization (middle blue curve) and PDH (bottom black curve) error signals obtained with non-symmetric resonant peaks (top red curve).

qualitatively compared to the well established technique in Figure 3.17. Polarization lock and PDH technique error signals are thus measured at the same time. The polarization lock method can be easily implemented without any frequency modulation. The two error signals both cross zero at the maximum of the resonance peaks and look similar, however, the PDH technique cannot discriminate different polarizations since both slopes of the error signals have the same signs. Besides, since our error signal is built on a similar way as in Reference [123] where a quantitative comparison is provided, we expect that locking performance will be similar to PDH.

Contrary to the method of Reference[123], the method presented here is not usable for two-mirror cavities since it uses a phase shift between the s and p waves reflection coefficient. However, the error signal obtained with the method of Reference[123] depends

on the azimuth orientation of the cavity mirrors [124], while it only depends on the incident angles which are fixed by the cavity geometry in the method described in this paper. The implementation of the method of Reference [123] in the case of four-mirrors cavity may therefore be more complex.

This method was also implemented in employing an optical enhancement cavity in order to produce a narrow-bandwidth and high-flux photon beam at High Energy Accerlerator Reseach Organization (KEK), Japan[125]. They recieve the same error signal as ours and this lock is stable.

In conclusion, a new method to lock a laser on an optical cavity is proposed. Special design of coating layers of the cavity mirrors and laser non-nominal incidence angle lead to enough s- and p-wave phase detuning to generate two resonance peaks in the cavity. This polarization property can be used to generate an error signal and lock the laser to the cavity. Theoretical calculation and experiment results proved its feasibility.

However, the polarization locking technique is less stable than the PDH technique bacause of its sensitivity to beam pointing. We prefer to use the PDH techinque in our experiments.

3.4 Cavity Thermal Effect

The final goal of achieving high flux X-rays $10^{11} - 10^{13}$ ph/s needs extremely high power stored in the cavity (such as ThomX, more than 600 kW). The energy deposited by the beam in the substrate or coating of cavity mirrors is high enough so that it gives rise to mirror deformations. With the changes in mirror surfaces, the geometry-dependent Gouy phase is revised and cavity modes become huge, leading to the decrease of cavity coupling and gain. It is necessary to present some qualitative thermal effect analysis.

3.4.1 Winkler's Deformation Model

Because of its absorption in optical elements, a high-power laser can cause serious problems in an optical apparatus. A simple approach for estimating the thermal expansion of optical mirrors induced by an impinging laser beam is proposed in Reference[126]. When a beam passes through a beam splitter or a cavity coupling mirror, absorption may occur in the dielectric coating and inside the substrate material. An optical mirror exposed to a laser beam is locally heated, causing it to deform. In addition, the wavefront of the reflected or transmitted beam is also deformed. In addition to the geometric

deformation resulting from the local heating, the temperature gradient that forms inside the mirror substrate results in a gradient of the refraction index. This causes a change in the wavefront curvature of the beam. This phenomenon is called thermal lensing.

Thermal Expansion

When a laser beam reflects off a mirror, part of the beam power is absorbed by the coating. The power is absorbed (approximately 10^{-6}) and diffused through the substrate. A temperature gradient then forms in the substrate, extending over a hemisphere whose radius is equal to that of the beam spot on the mirror. The result is an expansion of the substrate, leading to deformation of the mirror's surface, even for a convex mirror. These thermal effects can be calculated using the Winkler model, which is described in Reference[126]. A more complete model can be found in References[127,128]. The mirror deformation is treated as a change δs in the curvature depth of the mirror, as shown in Figure 3.18.

Under the assumption that the deformation is directly proportional to the temperature gradient, one can evaluate the change in the depth of curvature as follows:

$$\delta s \approx \frac{\alpha \omega_m \delta T}{2} \tag{3-32}$$

where α is the thermal expansion coefficient of the substrate, ω_m is the radius of the beam spot on the mirror, and δT is the temperature change across the affected hemisphere.

The value of δT is related to the power absorbed by the coating, P_a:

$$P_a = \kappa \pi \omega_m^2 \triangle T \approx 2\pi \kappa \omega_m \delta T \tag{3-33}$$

where $\pi\omega_m^2$ is the surface area through which the heat is transported, κ is the thermal conductivity of the substrate, and $\triangle T$ is the temperature gradient in the substrate.

Finally, for an optical cavity, the change in the depth of curvature of the mirrors is proportional to the power stored in the cavity through the following relation:

$$\delta s_e \approx \frac{\alpha}{4\pi\kappa} \alpha_r P_s \tag{3-34}$$

where P_s is the power stored in the cavity and α_r is the power absorption coefficient of the cavity mirror coating. For ThomX α_r is less than 0.5 ppm.

Table 3.2[52] lists the thermal properties of different substrate materials. The substrate

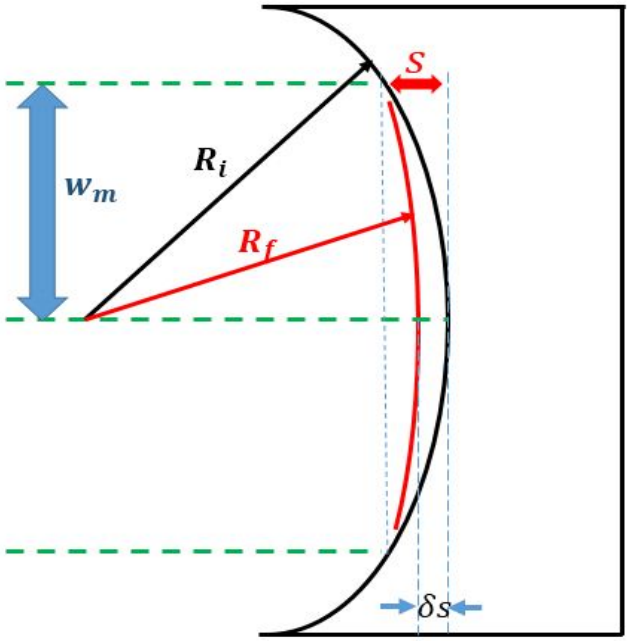

Figure 3.18 Schematic diagram of the mirror deformation induced by power absorption in the mirror coating. R_i and R_f are the initial and final radii of the mirror, respectively, *i.e.*, the radii before and after deformation. ω_m denotes the beam size. s is the depth of curvature before deformation. δs is the deformation-induced change in the depth of curvature.

Table 3.2 Thermal properties of materials commonly used as mirror substrates[52]. α is the coefficient of thermal expansion, κ is the thermal conduction, β is the thermo-optical coefficient, and α_s is the linear absorption coefficient. Values of δ_{se} are calculated for a stored power of 500 kW and a coefficient absorption of 1 ppm.

Materials	$\alpha(10^{-6}/\mathrm{K})$	κ(W/m/K)	$\beta(10^{-6}/\mathrm{K})$	α_s(ppm/cm)	δ s$_e(nm)$
Fused Silica	0.55	1.38	10	2	16
ULE	0.01	1.31	11	5850	0.3
Suprasil	0.6	1.38	10	0.5	17
Sapphire	5	46	13	50	4

of the cavity mirrors in ThomX is Corning Code 7972 ULE (Ultra Low Expansion) glass[129]. It is a titania silicate glass with near-zero expansion characteristics. The characteristics of this material are as follows: $\alpha = 10^{-8}$ K^{-1} and $\kappa = 1.31$ $Wm^{-1}K^{-1}$. Consider the following simple example: the storage of 500 kW of power in the cavity gives rise to a deformation of $\delta s_{e,ULE} \approx 0.304$ nm. For comparison, the properties of fused silica are $\alpha = 5.5 \times 10^{-7}$ K^{-1} and $\kappa = 1.38$ $Wm^{-1}K^{-1}$. The same amount of stored power causes a deformation of $\delta s_{e,FS} \approx 15.86$ nm. The deformation of ULE glass is thus approximately 50 times lower than that of fused silica. From Equation 3-34, we can see that the deformation depends on the ratio between the substrate expansion coefficient and the thermal conductivity. Thus, a low thermal expansion coefficient is desirable, but a high thermal conductivity is also important.

Thermal Lensing

When a laser beam passes through a mirror, such as the cavity coupling mirror, a portion of the laser power is also absorbed by the substrate. The temperature gradient in the substrate then extends throughout the entire thickness of the mirror. This temperature gradient induces a change in the refractive index of the material. The substrate then acts as a lens that alters the curvature of the wavefront of the transmitted beam. We can estimate the deformation caused by the thermal lensing effect[126] using the following equation:

$$\delta s_l = 1.3 \frac{\beta}{4\pi\kappa} \alpha_s e P_l \tag{3-35}$$

where $\beta = \partial n / \partial T$ characterizes the temperature dependence of the refractive index of the material, α_s is the absorption coefficient per unit length of the substrate, e is the thickness of the substrate in the beam propagation direction, and P_l is the laser power entering the cavity. For the best material presently known, namely, diamond, β/κ is as low as 10^{-8} m/W. Meanwhile, according to Table 3.2, β/κ is 2.8×10^{-7} m/W for sapphire and 7.24×10^{-6} m/W for fused silica, which seems extremely large by comparison with α/κ of thermal expansion.

However, this does not mean that the effect induced by thermal lensing is larger than that induced by thermal expansion (heat conduction). In a high-finesse cavity, the circulating power P_s in Equation 3-34 is much greater than the injected power P_l in Equation 3-35. Hence, it is reasonable to ignore the thermal lensing effect for the coupling mirror M1 whose substrates are made of fused silica, suprasil or sapphire. However, the linear absorption coefficient α_s of ULE is around 10^3 times larger than that of other

materials. We cannot ignore the thermal lensing effect of cavity mirror whose substrate is made of ULE. That is why we choose the sapphire substrate for coupling mirror.

Finally, in order to decrease the thermal deformation of ThomX cavity mirrors, we choose the sapphire substrate for the coupling mirror M1, and the ULE substrates for M2, M3 and M4. Meanwhile, thermal expansion is certainly the main cause of deformation for such highly reflective cavity mirrors M1, M2, M3 and M4.

Radius of Curvature of a Deformed Mirror

In Winkler's model, it is assumed that the mirror surface is always spherical before and after deformation; only the radius of curvature of the mirror changes. In Figure 3.18, R_i and R_f denote the initial and final radii, *i.e.*, the radii before and after deformation.

From Figure 3.18, one can relate the initial depth of curvature s to the initial radius of curvature R_i:

$$s = R_i - \sqrt{R_i^2 - \omega_m^2} \tag{3-36}$$

If $R_i \gg \omega_w$, as is the case in ThomX, where $R_i \approx 2$ m $\gg \omega_m \approx 2$ mm, then one can make the approximation $s \approx \omega_m^2/(2R_i)$. Similarly, the depth of curvature after deformation can be related to the new radius of curvature as follows: $s - \delta s \approx \omega_m^2/(2R_f)$. Finally, we have

$$R_f \approx \frac{1}{\frac{1}{R_i} - \frac{2\delta s}{\omega_m^2}} \tag{3-37}$$

We take a planar cavity coupling mirror ($R_i = +\infty$) as an illustrative example to provide a better understanding. Suppose that the cavity mode is approximately $\omega_m = 2$ mm and that the deformation is $ds = 20$ nm, caused by several hundred kilowatts of power. Then, we have $R_f = -100$ m. The radius of curvature has decreased dramatically. The change in the radius of curvature will result in a modification to the round-trip matrix. Hence, the size of the beam circulating in the cavity will be much larger than before. These changes must be considered in case they will make the cavity unstable.

3.4.2 Cavity Gouy Phase

We introduced the Gouy phase in Section 2.1.1 while discussing Gaussian beams. The Gouy phase is an additional phase shift of a Gaussian beam, of the form $\arctan(z/z_0)$.

The Gouy phase of any focused beam is a result of transverse spatial confinement, which induces a spread in the transverse momenta due to the uncertainty principle[130].

A Gouy phase shift can be accumulated as a Gaussian beam propagates through an optical setup consisting of multiple optical elements. Various methods can be used to calculate the accumulated Gouy phase[72,131,132].

Suppose that the cavity round-trip matrix is $\begin{pmatrix} A & B \\ C & D \end{pmatrix}$; then, the cavity Gouy phase accumulated over one round trip for a Gaussian eigenmode can be calculated from this matrix[87,131]:

$$\phi_G = \arccos(\frac{A+D}{2}) \tag{3-38}$$

As discussed in Section 3.4.1, the deformation caused by a high-power laser modifies the round-trip matrix. Hence, the Gouy phase will change along with the deformation. The Gouy phase of the prototype cavity for ThomX, which is called S-Box and is depicted in Figure 3.13, has been calculated as a function of the deformation. The results are shown in Figure 3.19.

The tangential and sagittal Gouy phases shown at the top of Figure 3.19 are different, but both increase linearly with the deformation. The change in the Gouy phase is what we are most interested in because the cavity gain is very sensitive to this variation (as will be discussed in Section 3.4.3). The change in the Gouy phase also exhibits a linear trend. The Gouy phase changes by approximately 26 mrad with a deformation of 1 nm.

3.4.3 Thermal Effect on Energy Gain

The thermal deformation leads to a decrease in the coupling between the injected beam and the cavity mode. The cavity gain also drops because of the change in the Gouy phase. Here, we derive the relationship between the gain and the deformation.

By analogy with Equation 2-16, we can write the cavity gain for an n-mirror cavity as follows:

$$G = \frac{|\widetilde{t_1}(\omega)|^2}{|1-\rho(\omega)\exp(-i\Phi(\omega))|^2} \tag{3-39}$$

where $\rho = r_1 r_2 \cdots r_n$.

When the laser is locked to the cavity, which means that $\Phi(\omega) = 2\pi$, the gain reaches

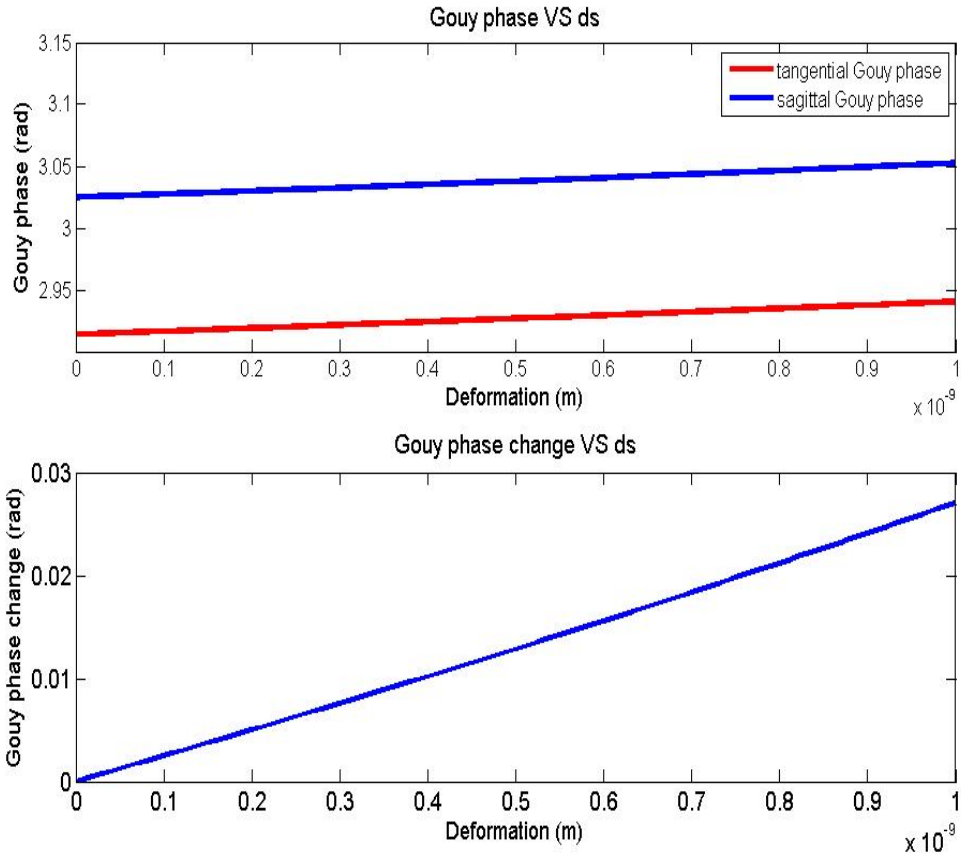

Figure 3.19 Top: Tangential and sagittal Gouy phases as functions of the deformation. Bottom: Change in the Gouy phase as a function of the deformation.

its maximum value of G_m. The change in the Gouy phase due to thermal deformation causes the gain to decrease. Let us consider the Gouy phase variation $\triangle\phi_G$ that corresponds to a gain drop of one half, $\frac{1}{2}G_m$. We have

$$\begin{cases} G_m = \dfrac{|\widetilde{t_1}(\omega)|^2}{|1-\rho(\omega)|^2} \\ \dfrac{1}{2}G_m = \dfrac{|\widetilde{t_1}(\omega)|^2}{|1-\rho(\omega)\exp(i\triangle\phi_G)|^2} \end{cases} \tag{3-40}$$

Under the assumption that the Gouy phase variation satisfies $\triangle\phi_G \ll 1$, we can obtain

$$\triangle\phi_G \approx \frac{1-\rho^2}{\rho} = \frac{\pi}{F} = \frac{1}{G_m} \tag{3-41}$$

Equation 3-41 provides a quantitative analysis of the relationship between the cavity finesse and the change in the Gouy phase that corresponds to a gain drop to half of the

maximal gain. We find that the cavity gain is very sensitive to the Gouy phase variation caused by the thermal effect, especially for a high-finesse cavity.

For an optical cavity that consists simply of two concave mirrors with the same radius of curvature, the round-trip matrix is written as[133]

$$\begin{pmatrix} A & B \\ C & D \end{pmatrix} = \begin{pmatrix} \frac{2f^2-2fL+(L-L_c)L_c}{2f^2} & \frac{(2f-L_c)(2fL+L_c+L_c^2-LL_c)}{2f^2} \\ \frac{-2f+L-L_c}{f^2} & \frac{2f^2-2fL+LL_c-L_c^2}{2f^2} \end{pmatrix} \tag{3-42}$$

where L_c is the distance between the two concave mirrors, L is the round-trip length of the cavity, and f is the focal length of each concave mirror.

To obtain a small waist, the cavity is always made to operate near the unstable region. We adopt the approximation $f = R_i/2 \sim L_c/2$; thus, we obtain

$$\frac{A+D}{2} = \frac{2f^2 - 2fL + LL_c - L_c^2}{2f^2} \approx -1 \tag{3-43}$$

Then, we assume that the scale of the variation of the term $\frac{A+D}{2}$ due to the thermal effect is $\epsilon = \delta(\frac{A+D}{2}) \ll 1$.

$$\arccos(\frac{A+D}{2} + \epsilon) \approx \arccos(-1+\epsilon) = \pi - \sqrt{2\epsilon} \tag{3-44}$$

We let δf denote a tiny change in the focal length of the concave mirrors; then, we have

$$\frac{\delta(\frac{A+D}{2})}{\delta f} = \frac{\delta(1 - \frac{L}{f} + \frac{LL_c - L_c^2}{2f^2})}{\delta f} \approx \frac{8L_c - 4L}{L_c^2} \tag{3-45}$$

In accordance with Equation 3-37, we adopt the approximation $\delta s \ll \omega_m$, and we obtain R_f as follows:

$$R_f \approx R_i(1 + \frac{2\delta s R_i}{\omega_m^2}) \tag{3-46}$$

From Equation 3-46, we can determine δR_i:

$$\delta R_i = \frac{2R_i^2 \delta s}{\omega_m^2} \tag{3-47}$$

Then, we can obtain ϵ:

$$\begin{aligned}\epsilon = \delta(\frac{A+D}{2}) &= \frac{\delta(\frac{A+D}{2})}{\delta f} \times \frac{\delta f}{\delta R_i} \times \delta R_i \\ &= \frac{4(2L_c - L)R_i^2 \delta s}{L_c^2 \omega_m^2}\end{aligned} \tag{3-48}$$

A tiny change ϵ in $\arccos(\frac{A+D}{2})$ leads to a Gouy phase shift of $-\sqrt{2\epsilon}$. From Equation 3-41, we know that a drop of one half in the gain corresponds to the following value of ϵ:

$$\epsilon = \frac{\pi^2}{2F^2} \tag{3-49}$$

From Equations 3-48 and 3-49, it is easy to obtain the relationship between the deformation $\delta s_{\frac{1}{2}}$ and the finesse F when the gain drops by half.

$$\delta s_{\frac{1}{2}} = \frac{\pi^2 \omega_m^2}{32(2L_c - L)F^2} \tag{3-50}$$

Equation 3-50 shows that the deformation $\delta s_{\frac{1}{2}}$ is inversely proportional to the square of F. This remarkable conclusion once again confirms that the gain is very sensitive to the deformation for a high-finesse cavity. The calculated cavity gain as a function of the deformation for the prototype cavity for ThomX with $F = 3,000$ is plotted in Figure 3.20. Here, we assume that all four cavity mirrors have the same deformation. From Figure 3.20, we find that a deformation of approximately 0.05 nm will cause the gain to decrease by half.

The discussion above shows that the gain is extremely sensitive to the deformation in open loop. Hence, a strong and robust feedback in closed loop is really needed to compensate the effect of deformation and hold the cavity on resonance all the time.

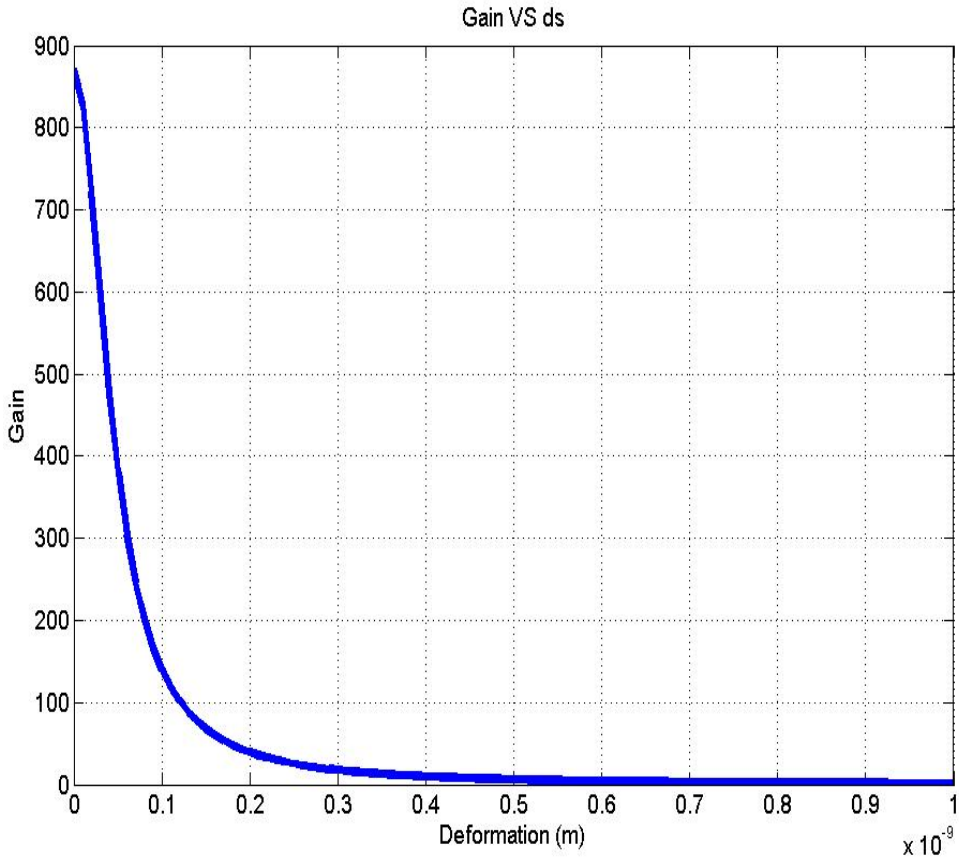

Figure 3.20 Gain as a function of the deformation for a cavity with $F = 3,000$.

Chapter 4 High-Power Experiments on a Prototype Cavity for ThomX

High-power experiments on a prototype cavity are described in this chapter. First, the prototype S-Box cavity is introduced, including the oscillator, the amplifier, and the mechanical design. The cavity finesse is approximately 26,000, as measured using four different methods, and we find that the deposition of dust on the cavity mirrors causes the finesse to decrease considerably. Ultimately, we achieve a stable power as high as 383 kW with a cavity gain of 10,000.

4.1 Prototype S-Box Cavity

The prototype cavity for the ThomX project is called S-Box and consists of two planar mirrors, M1 and M2, and two spherical mirrors, M3 and M4, as shown in Figure 4.1. The waist, *i.e.*, the interaction point, is located between the two spherical mirrors. In this section, the entire super-cavity optical system and the vacuum vessel design are described.

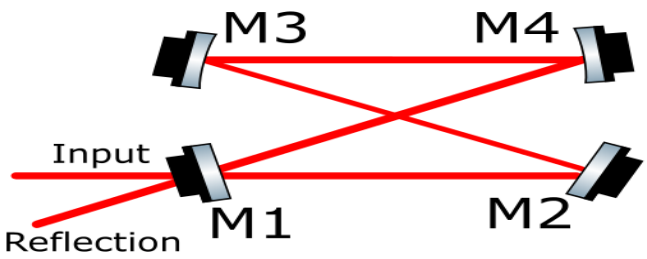

Figure 4.1 Schematic illustration of the S-Box cavity (prototype cavity for ThomX).

4.1.1 Oscillator

Three oscillators are chosen for injection into the prototype cavity. One is an NKT Koheras CW (continuous wave) laser operating at a wavelength of 1031 nm, whose highest power output is on the order of one hundred milliwatts. The second one is a Menlo Orange pulse laser, also operating at 1031 nm, with a repetition frequency of approximately 178.5 MHz, corresponding to the S-Box cavity length of 1.68 m. The last

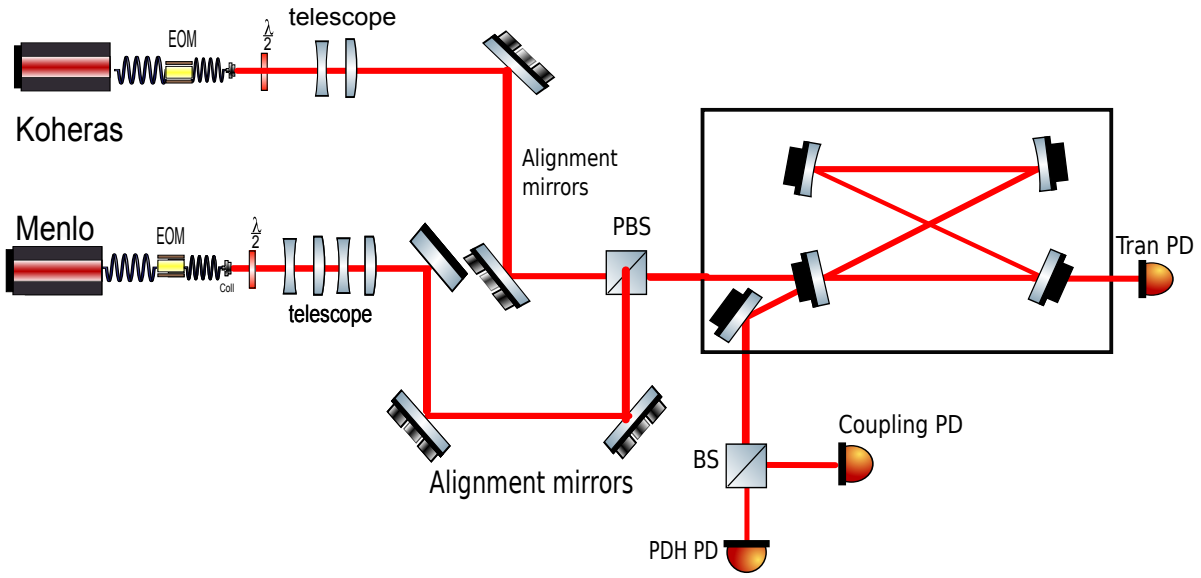

Figure 4.2 Schematic diagram of the experimental setup for testing the S-Box cavity.

one is a Onefive Origami bulk laser with extremely low phase noise. It operates at 1031 nm with a repetition frequency of 133.3 MHz. We received this Onefive laser at the end of my thesis.

Figure 4.2 shows a schematic diagram of the experimental setup for testing the S-Box cavity. Because of the different external cavity length, the Onefive Origami bulk laser does not appear in this figure. A telescope consisting of several lenses is mainly used for mode matching between the cavity mode and the input beam. Two alignment mirrors on each beam line provide good alignment to reduce the coupling to other high-order modes. The reflected beam from the cavity is split into two parts after passing through a beam splitter, as shown in Figure 4.2. Part of the beam is directed to a coupling photodiode, which is used to measure the coupling, and the other part of the beam is directed to a PDH photodiode, which is used to generate the error signal for locking. By recording the transmitted beam from the transmission photodiode and the coupling, we can achieve good alignment and mode matching. The S-Box cavity needs to be installed in a high-vacuum (approximately 10^{-2} mbar) vessel to reduce noise and obtain a stable lock. For the same reason, the entire setup must be installed on a mechanically stable optical table.

A CW laser is often used to measure the finesse of a cavity because such a laser has a low phase noise, as discussed in Section 3.1, and can be easily locked to the cavity.

Meanwhile, a pulse laser is provided as a seed resource for the laser amplifier. In our setup, double wedges were inserted into the Menlo oscillator for CEP (carrier-envelope phase) tuning.

However, because of the high phase noise, we failed to lock the Menlo laser to the cavity with a finesse of 26,000. It can be clearly observed that the error signal in Figure 4.3 is very noisy. The blue curve is the error signal when the cavity is unlocked. In fact, the error signal produced with the cavity polarization locking technique described in Section 3.3 reveals the high noise more clearly. To address this problem, we ultimately chose a Onefive Origami bulk laser, which has an extremely low phase noise, for the ThomX project. A measurement of its extremely low phase noise was presented in Section 3.1. The error signal generated by the Onefive oscillator is very clear, even for a high-finesse (26,000) cavity, as shown in Figure 4.4. A ringing effect is observed in the transmission curve for this high-finesse cavity.

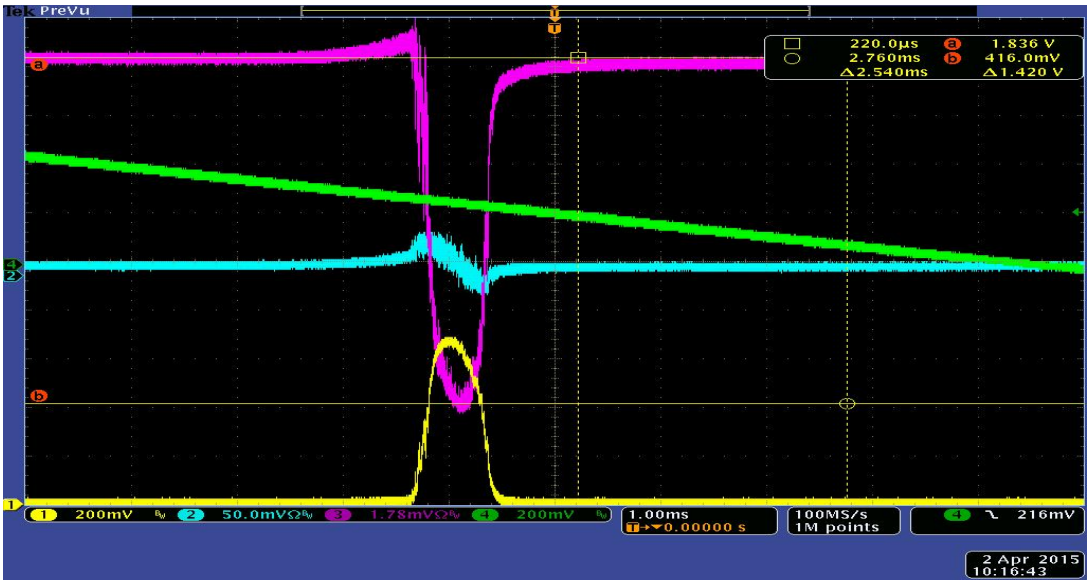

Figure 4.3 Open-loop measurement using the Menlo oscillator. The yellow curve is the cavity transmission curve. The blue curve is the error signal. The green curve is the ramp voltage applied to the PZT (piezo-electric transducer). The pink curve is the coupling signal.

4.1.2 Amplifier

To achieve our goal of high power storage in the cavity, an amplifier made by CELIA Laboratory[91,134] is required after the Menlo and Onefive Origami bulk oscillators. A schematic diagram of our amplifier is shown in Figure 4.5. There are three amplifica-

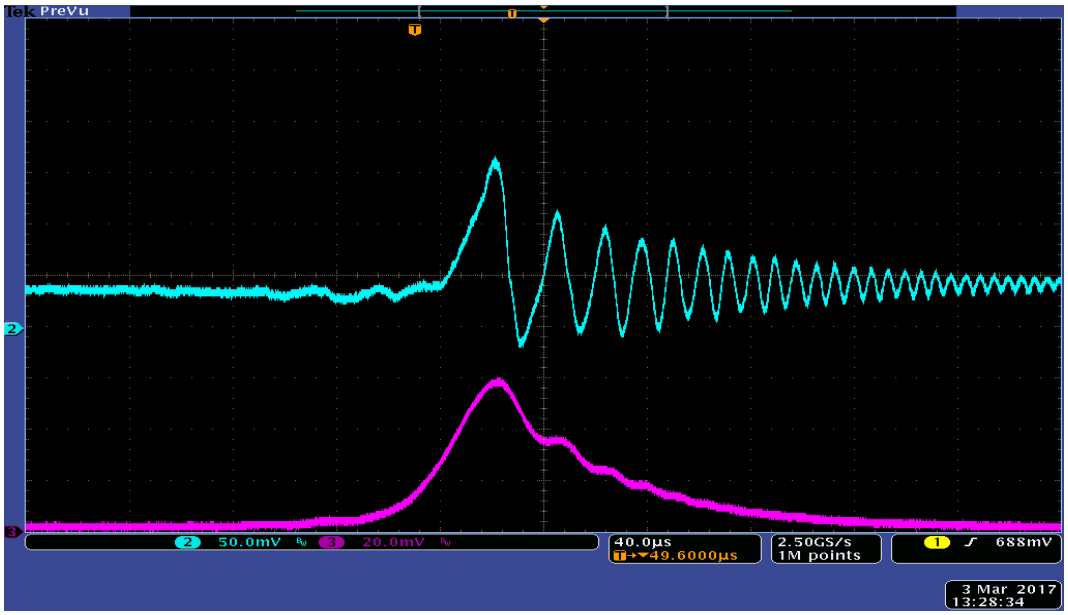

Figure 4.4 Error signal generated by the Onefive bulk oscillator (blue) and the corresponding transmission curve (pink).

tion stages in the amplifier. Before a pulse enters the amplifier, the pulse duration is expanded from approximately one hundred femtoseconds to approximately two hundred picoseconds. A diode is used to pump the laser in the first stage. An isolator protects the diodes and oscillator from the reflected beam. To monitor the operating conditions, 5% of the output power of the first stage is extracted using a DET36-A[135] photodiode. In the second and third stages, chillers are required to cool the diodes. Our group uses two diodes in the second stage and six diodes from Alphanov company[136] to pump the input laser in the last stage. The output power of the second stage can reach 2.25 W, whereas the output average power can be as high as 60 W in the last stage. We can control the output power by tuning the pump current. A CVBG (chirped volume Bragg grating)[91] is used to compress the pulse duration to several picoseconds. However, because of the high power, the fiber can be easily burned if the amplifier operates at full power for a long time. Hence, the amplifier would always operate under full power during our experiments.

In addition to the output power of the amplifier, we also care about the quality of the beam, as measured by the beam quality factor M^2 [137], which represents the degree of variation of the laser beam from the ideal Gaussian beam. We used the fast wavefront sensor of HASO device from Imagine Optic company[138] to measure the M^2 parameter, as shown on the left-hand side of Figure 4.6. Four wedges and two filters were used to lower the output power to avoid damaging the wavefront sensor. Figure 4.6 shows that the waist size is approximately 0.068 mm and is located at a distance of 101 mm from

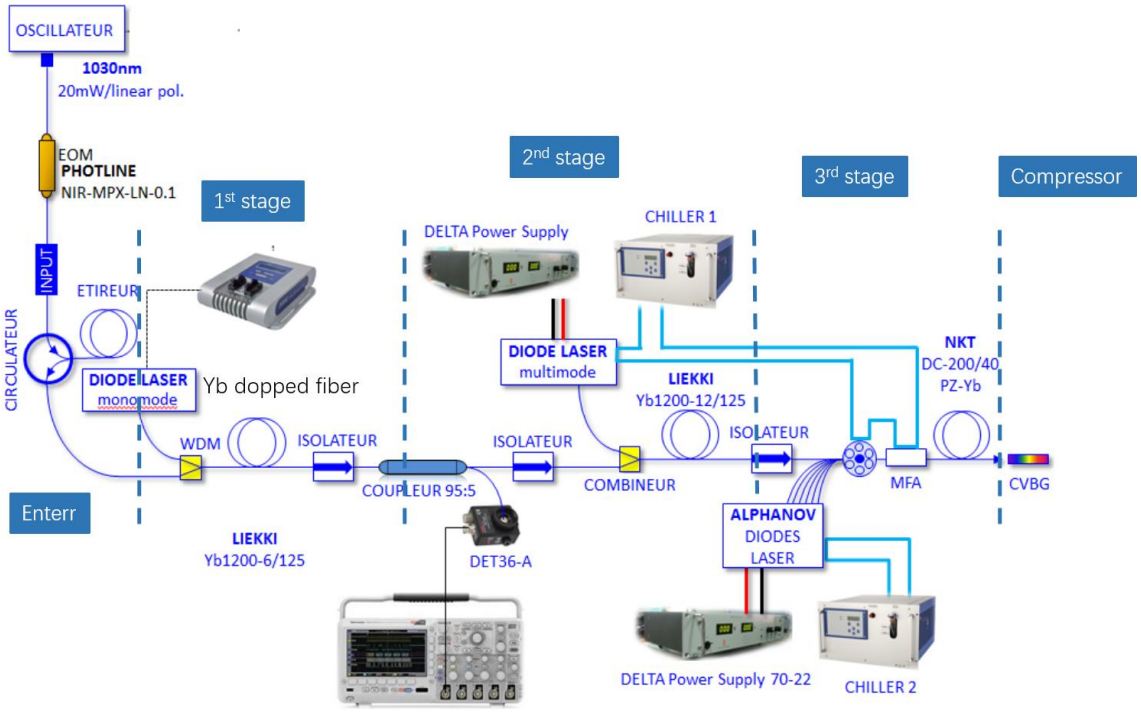

Figure 4.5 Amplifier for the S-Box cavity from CELIA [134]. There are three amplification stages.

the sensor. These two parameters can help us to design the telescope to ensure good mode matching. The value of M^2 is approximately 1.04, which indicates that the beam quality is very good. We also measured the beam profile at a high output power. Nearly identical beam properties can be observed in the two measurements presented in Figure 4.7. Correlation measures of more than 90% were achieved. For the two measurements, the first and second stages were operating at full power, and the pump current in the third stage was set to 1 A and 6 A.

The final amplifier for the ThomX project was designed and produced on the basis of these findings. The power reached is as high as 210 W, and the beam quality is also good. The amplifier can operate constantly at 104 W for more than 90 h. Such fiber amplifiers are very efficient.

4.1.3 Cavity Mirrors

Three sets of cavity mirrors shown in Table 4.1 are available in our experiments. The Mirror Set 1 and 2 are mainly used for doing test experiments on the prototype S-Box cavity. A new polarization lock technique was proposed in Section 3.3 by using the Mirror

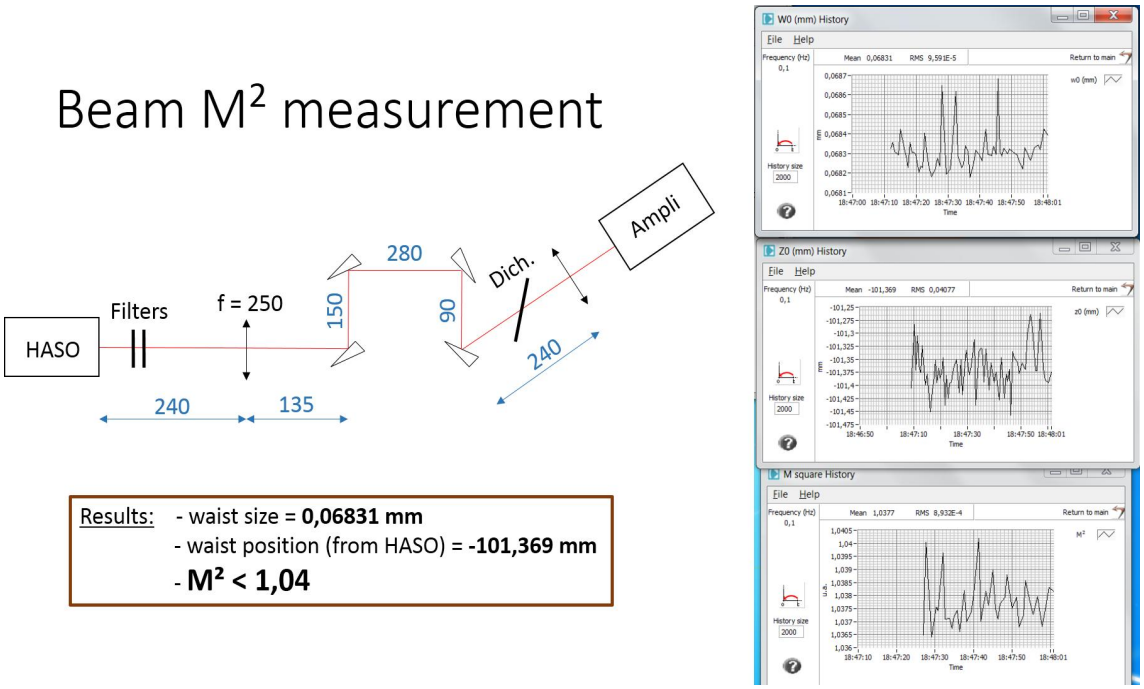

Figure 4.6 Measurements of the beam waist size, waist position and M^2 parameter after the amplifier with the second stage operating at 0.5 A. The output power was approximately 1 W. The distances between the wedges are reported in millimeters.

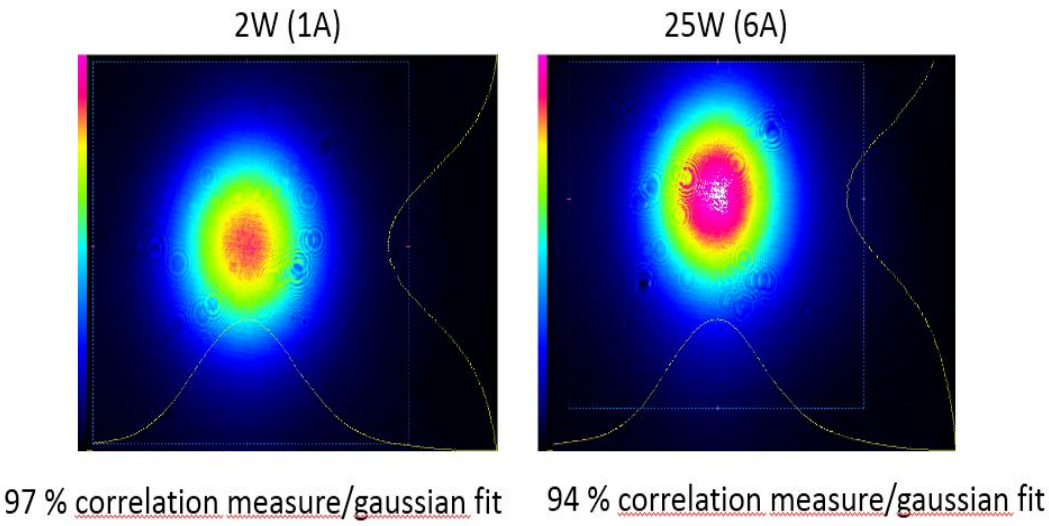

Figure 4.7 Measurements of the beam profile at pump currents of 1 A and 6 A. The first and second stages were operating at full power, and the pump current in the third stage was set to 1 A and 6 A. The former corresponds to an output power of 2 W, and the latter corresponds to 25 W.

Set 1. High-power experiments in Section 4.5 are reported with the help of the Mirror Set 2. The Mirror Set 3 whose finesse is as high as 42,500 will be installed on ThomX. The mirror substrates of Set 1, corresponding to $F = 3,000$, are all made of fused silica. Meanwhile, as dicussions in Section 3.4, in order to reduce the mirror deformation we choose ULE as the substrate material for M2, M3 and M4 and suprasil/sapphire for M1 of Mirror Set 2 and 3.

The parameters of the optical resonators we used are listed in Table 4.2. All cavities are planar and composed of two flat mirrors and two spherical mirrors. The beam waist between the spherical mirrors in tangential and sagittal direction are respectively $w_{0,t}$ and $w_{0,s}$ in Table 4.2. Cavities P178a and P178b differ in their finesse. They correspond to two different sets of mirrors. Then we increase the optical length of Cavity P178b to obtain the Cavity P133 and be able to use the OneFive Origami bulk oscillator.

4.1.4 Cavity Parameters

We introduce the cavity parameters of Cavity P178a. The length of the prototype S-Box cavity was determined based on the repetition frequency of the oscillator. Hence, the cavity length was fixed at 1.68 m. To achieve a high X-ray flux, a small interaction point, *i.e.*, the beam waist, must be small and cavity operations with such a small waist must be tested experimentally. To this end, the distance between the two spherical mirrors should be slightly larger than their radius of curvature. Figure 4.9 shows the design drawings for the prototype cavity. The radius of curvature of two spherical mirrors is 500 mm, and the distance between them is 504.3 mm, which means that the cavity is close to the unstable region. Two stepper motors were installed on M2 and M4 shown in Figure 4.1 to adjust the cavity length.

Figure 4.10 shows the tangential and sagittal beam sizes w_t and w_s, respectively, as functions of the distance from the mirror M1. The waist is located at the center of the distance between two spherical mirrors. At this point, the wavefront has an infinite radius of curvature. The tangential waist size w_t is 83.6 μm, and the sagittal waist size is approximately 60.6 μm. The tangential beam size on the mirror M1 is approximately 1.0 mm, and the sagittal beam size on M1 is 1.40 mm. To obtain a small waist, we set the distance between the two spherical mirrors such that the cavity would operate very close to the unstable region, as shown in Figure 4.11. If we increase the distance L between the two spherical mirrors, the beam size on M1 decreases very rapidly, while the waist size

Table 4.1 Three sets of cavity mirrors. The transmission, diffusion and absorption coefficients for power are given in parts per million. The theoretical finesses are also calculated.

Mirror Set 1 ($F = 3,000$)				
Mirror	M1	M2	M3	M4
Diffusion(ppm)	2	2.5	2	3
Absorption(ppm)	1	0.68	0.62	0.64
Transmission (ppm)	1060	410	334	375
Substrate Material	Fused silica			
Mirror Set 2 ($F = 28,000$)				
Mirror	M1	M2	M3	M4
Diffusion(ppm)	7	4.5	3.6	9
Absorption(ppm)	1.15	1.27	1.2	1
Transmission (ppm)	180	2	2	2
Substrate Material	Suprasil	ULE	ULE	ULE
Mirror Set 3 ($F = 42,500$)				
Mirror	M1	M2	M3	M4
Diffusion(ppm)	4	4.5	10	4.5
Absorption(ppm)	0.4	0.24	0.24	0.27
Transmission (ppm)	120	1.5	1.5	1.5
Substrate Material	Sapphire	ULE	ULE	ULE

Table 4.2 Parameters of the optical cavities used for testing experiments. The cavity mirror choice, the linewidth and waist size are given.

Cavity name	Cavity P178a	Cavity P178b	Cavity P133
FSR(MHz)	178.5	178.5	133
Cavtiy Length(m)	1.680	1.680	2.248
Cavity Mirrors	Set 1	Set 2	Set 2
Finesse	3000	28,000	28,000
Cavity Linewidth(kHz)	59	6.1	4.6
waist $w_{0,t}(\mu\text{m})$	84	84	83
waist $w_{0,s}(\mu\text{m})$	61	61	44

simultaneously increases considerably, as shown in Figure 4.11.

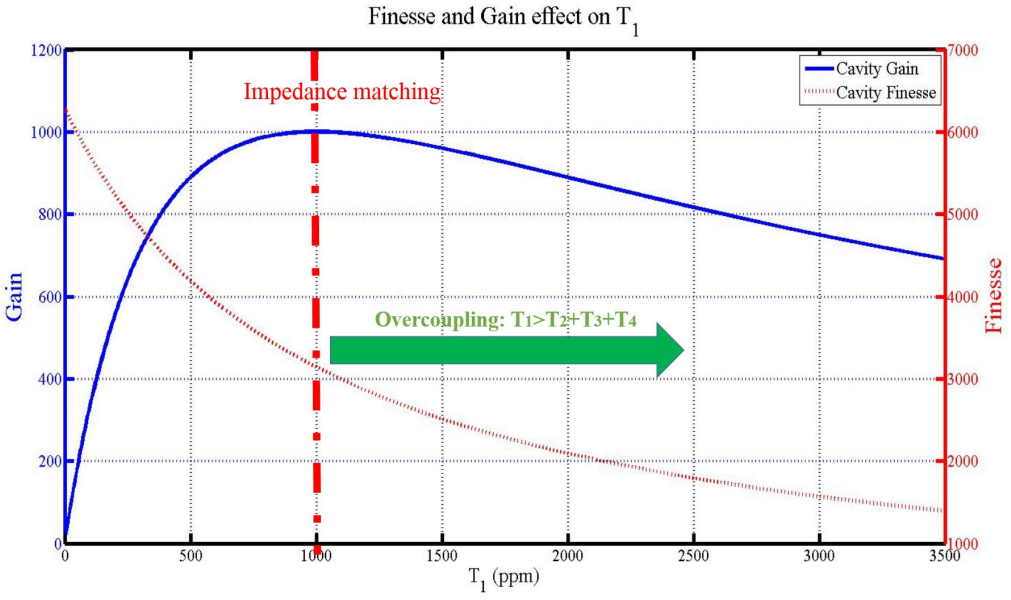

Figure 4.8 Cavity finesse and gain as functions of T_1.

The parameters of the cavity mirrors for a finesse of $F = 3,000$ are listed in Table 4.1. The cavity linewidth is approximately 58.9 kHz. With $F = 3,000$, the cavity is not in the impedance matching state. We designed the cavity to operate in the overcoupling regime, meaning that $T_1 > T_2 + T_3 + T_4$ shown in Figure 4.8. This choice was made because it is impossible to guarantee that the real transmissions of the cavity mirrors will be perfectly identical to the nominal ones; however, if the cavity falls into the regime in which $T_1 < T_2 + T_3 + T_4$, the energy gain will drop very rapidly shown in Figure 4.8. This

is also true for the high finesse cavity. Therefore, it is preferable to ensure that the cavity remains in the overcoupling regime to avoid an excessive decrease in gain.

The cavity mirrors for the ThomX project were manufactured by LMA (Laboratoire des Matériaux Avancés), located in Lyon, France. The finesse can reach as high as 28,000 and 42,500 shown in Table 4.1. The substrate of the cavity mirrors is Corning Code 7972 ULE (Ultra Low Expansion) glass, which is made of titania silicate and has near-zero expansion characteristics.

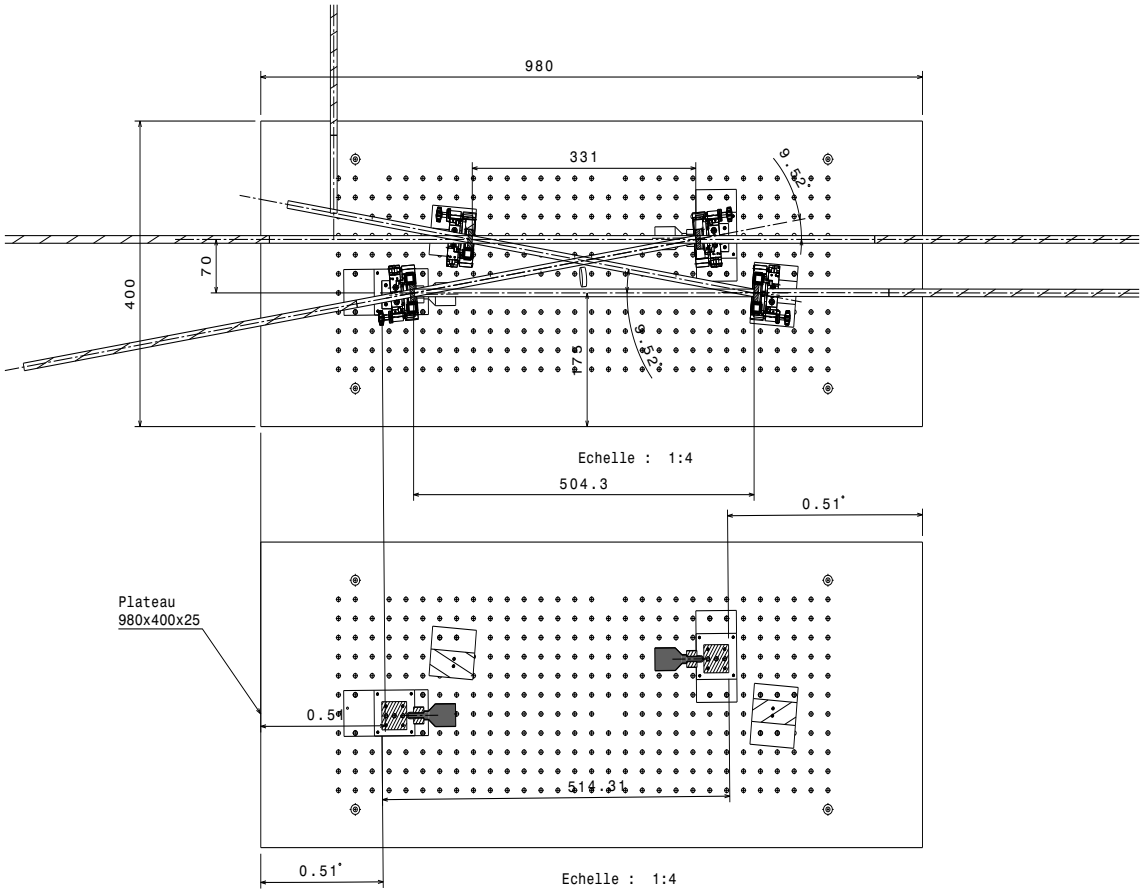

Figure 4.9 Design drawings for the prototype S-Box cavity P178a. The cavity consists of two planar mirrors and two spherical mirrors. The distance between the two spherical mirrors is 504.3 mm, which is slightly larger than their radius of curvature (500 mm). Two motors are used to adjust the cavity length.

4.1.5 Mechanical Description

Because of the mean free path of the electron beam and the instability of locking in air, the cavity must be installed inside a high-vacuum chamber. The design and

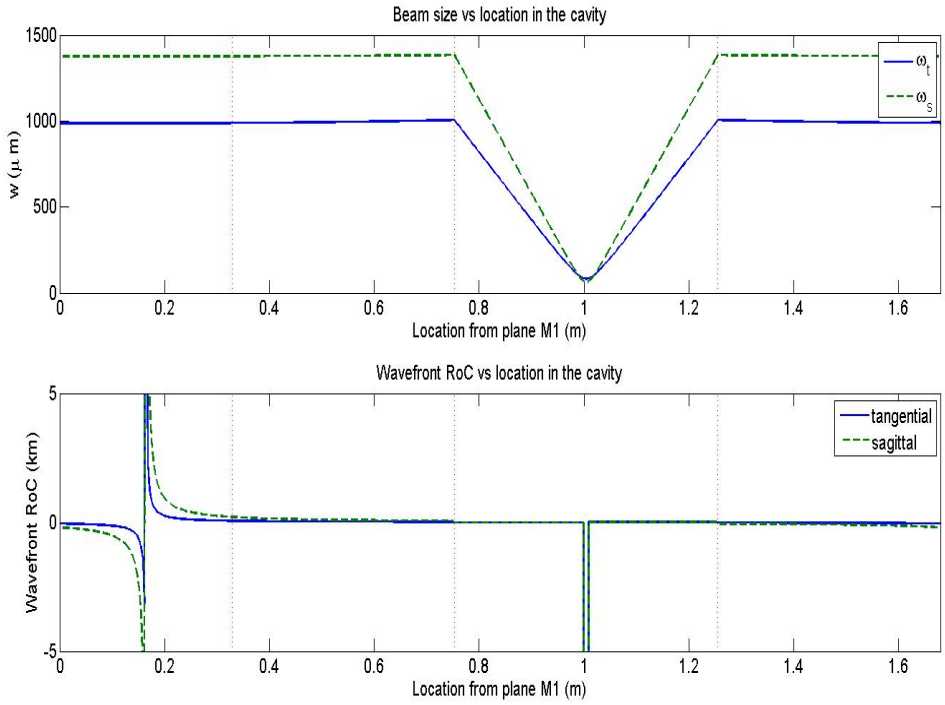

Figure 4.10 Top: The tangential and sagittal beam sizes w_t and w_s, respectively, as functions of the distance from the mirror M1. Bottom: The tangential and sagittal radii of curvature of the wavefront as functions of the distance from M1. The positions of the four mirrors are represented by the red dashed lines.

construction of the vacuum vessel for the prototype S-Box cavity were less complex than for ThomX itself because of the additional complexity introduced by the storage ring. However, some difficulties were still encountered during the manufacturing of the S-Box apparatus. Photographs of the prototype S-Box cavity are shown in Figure 4.12. The prototype consists of aluminum panels with seals and stainless steel frames. The ports of the vacuum vessel are mainly used for laser injection, coupling measurements, the feedthrough electrode for the mirror motors, the vacuum pump and vacuum monitoring. The vacuum in the vessel chamber can reach several 10^{-5} bar.

Because of the storage ring, the mechanical design of ThomX is much more complex than that of the prototype cavity. In the electron ring, there is a separation of only 200 mm between the dipoles, where the interaction point is located. Hence, it is impossible to host the optical cavity in a single vacuum chamber. In our group's design, the four cavity mirrors are separated into two vacuum chambers outside the dipoles, as shown in Figure 4.13. The laser beam crosses the electron beam at an angle of 2 degrees to allow the X-rays to escape from between the mirrors. Figure 4.14 shows the IP (interaction point) chamber,

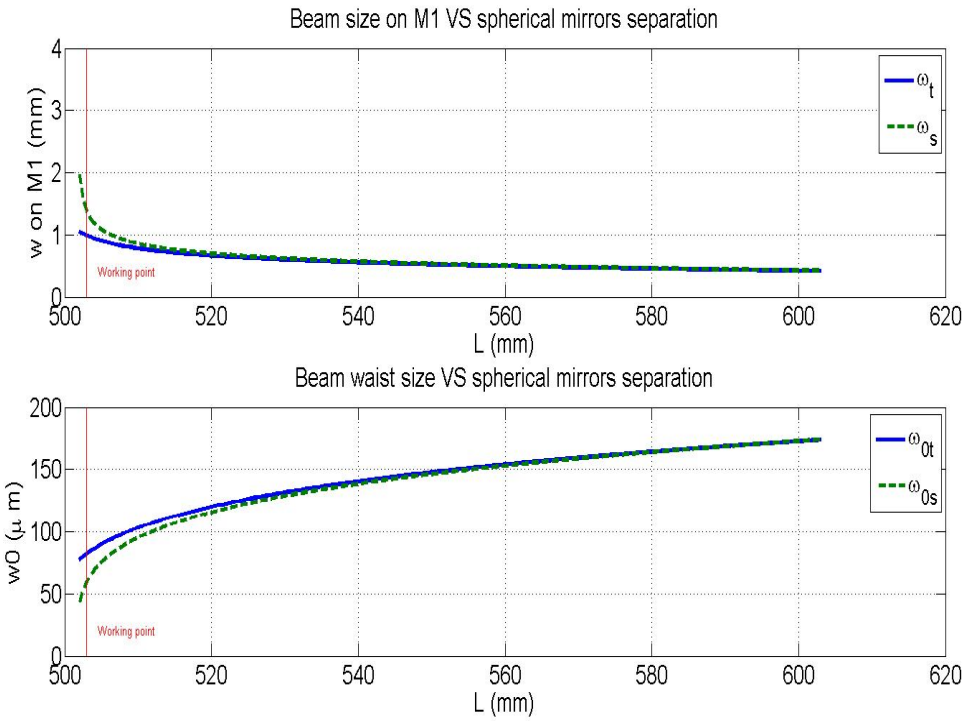

Figure 4.11 Top: The tangential and sagittal beam sizes on M1, w_t and w_s, respectively, as functions of the distance between the spherical mirrors. Bottom: The tangential and sagittal beam waists as functions of the distance between the spherical mirrors. The red line represents the working point.

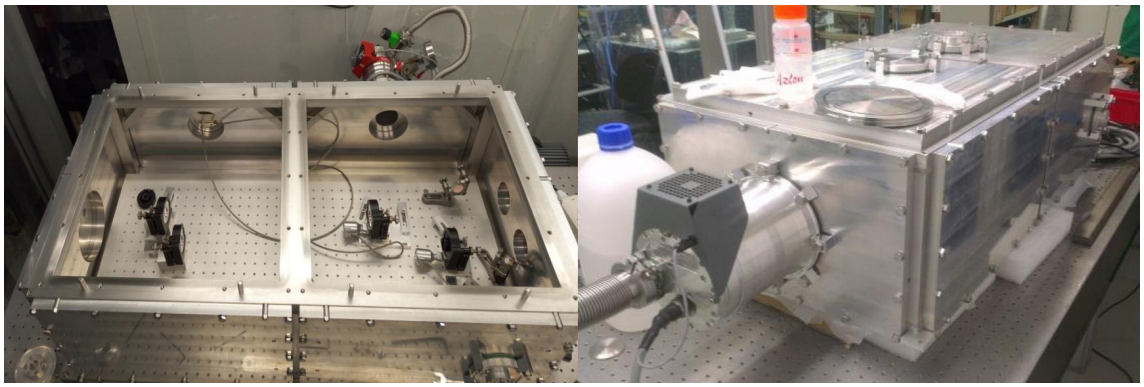

Figure 4.12 Photographs of the prototype S-Box cavity: (left) the cavity when open and (right) the cavity in vacuum.

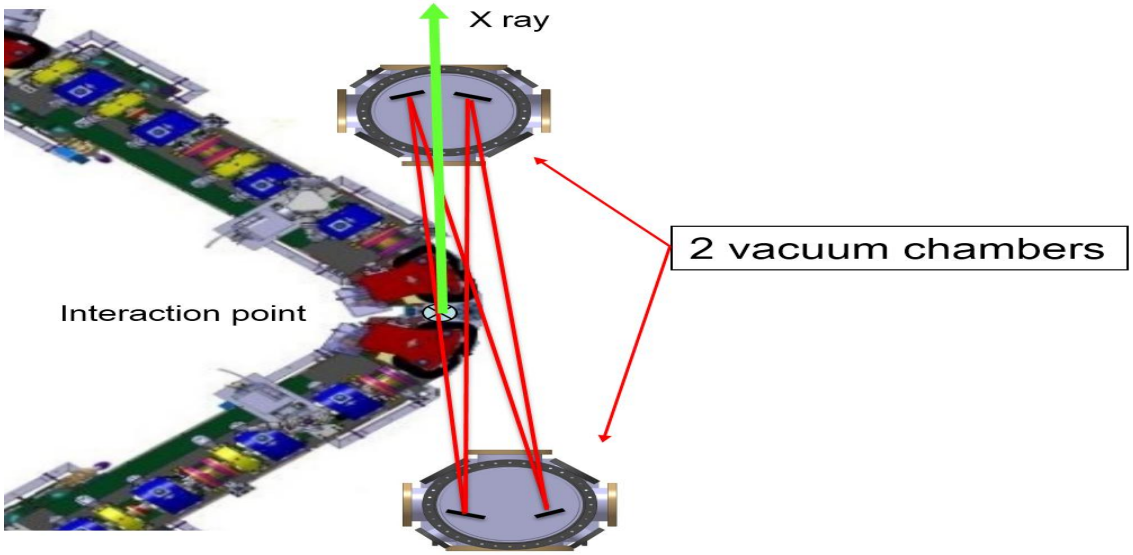

Figure 4.13 Schematic illustration of the mechanical design of ThomX. The four cavity mirrors are separated into two vacuum chambers outside the dipoles.

which provides the necessary connections between the two mirror vacuum chambers and the electron ring. The octagonal section is for the electron beam, and the rectangular section is for the laser beam. The two sections are connected by two slits.

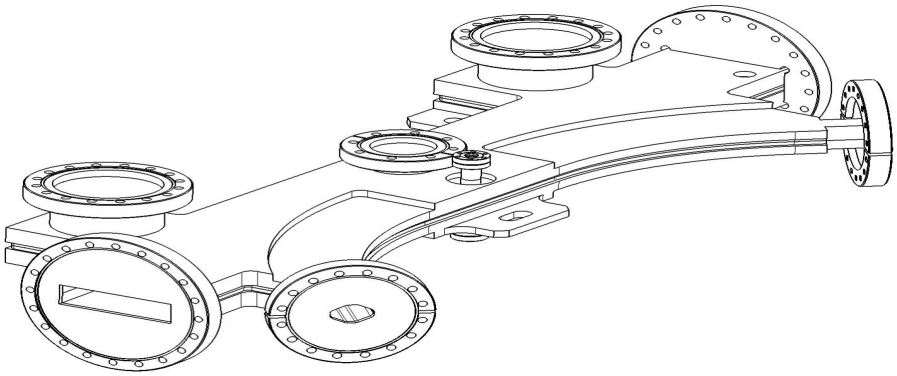

Figure 4.14 The IP chamber is used to provide connections between the two mirror cavities and the electron ring. It consists of two sections: an octagonal section for the electron beam and a rectangular section for the laser beam.

The Fabry-Pérot cavity is installed on a large granite table with a weight of approximately 6 tons, as shown in Figure 4.15. It was specially ordered from a French company named SYMETRIE to match the electron beam. A hexapod moving system is used to adjust the position of the laser beam around the interaction point. Three feet are used for rotation, and three feet are used for translation. The position is adjustable at a very high resolution of approximately 1 mm for translation and 2 mrad for rotation.

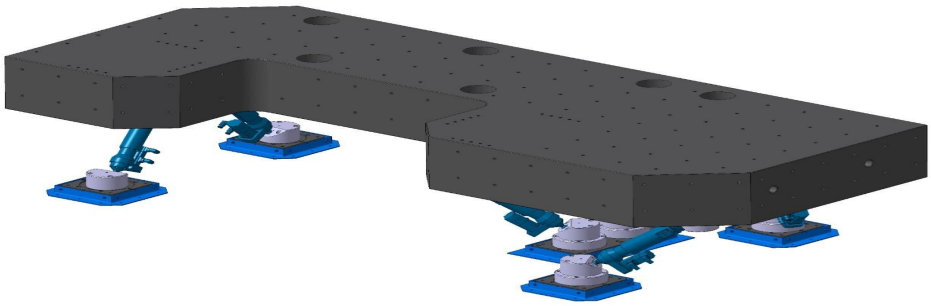

Figure 4.15 The hexapod movers for ThomX: three feet enable rotations, and three feet enable translations.

The table and all of the optical elements on it are isolated by housing to ensure laser safety and to avoid temperature fluctuations, as shown in Figure 4.16. It is necessary to ensure that the air flow inside the housing remains clean. The installation of the vacuum chambers for ThomX is shown in Figure 4.17.

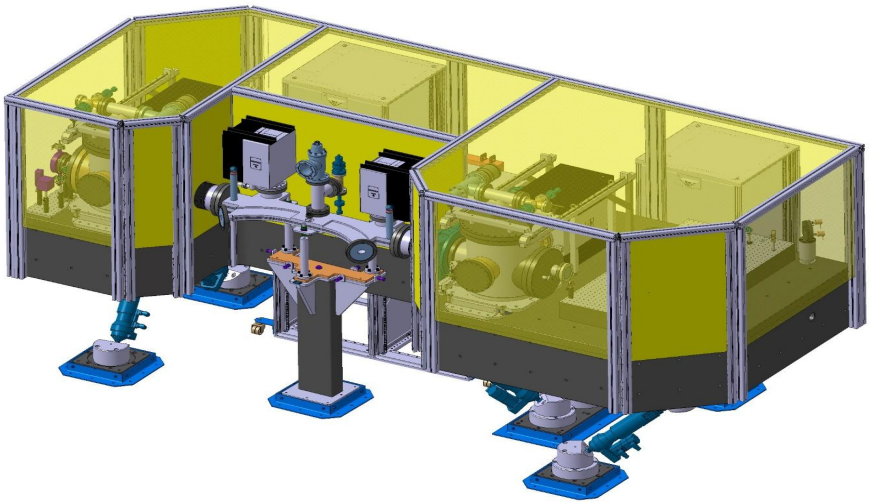

Figure 4.16 Schematic illustration of the housing used to isolate the table and the optical elements.

4.2 Mode Matching and Coupling

The coupling of a laser frequency comb to an optical cavity depends on many factors, including beam alignment, mode matching, and impedance matching. After tuning the alignment of the cavity mirrors, we need to close the cavity and begin the evacuation of the vacuum chamber. Hence, the cavity mode is fixed, and we need to design a telescope

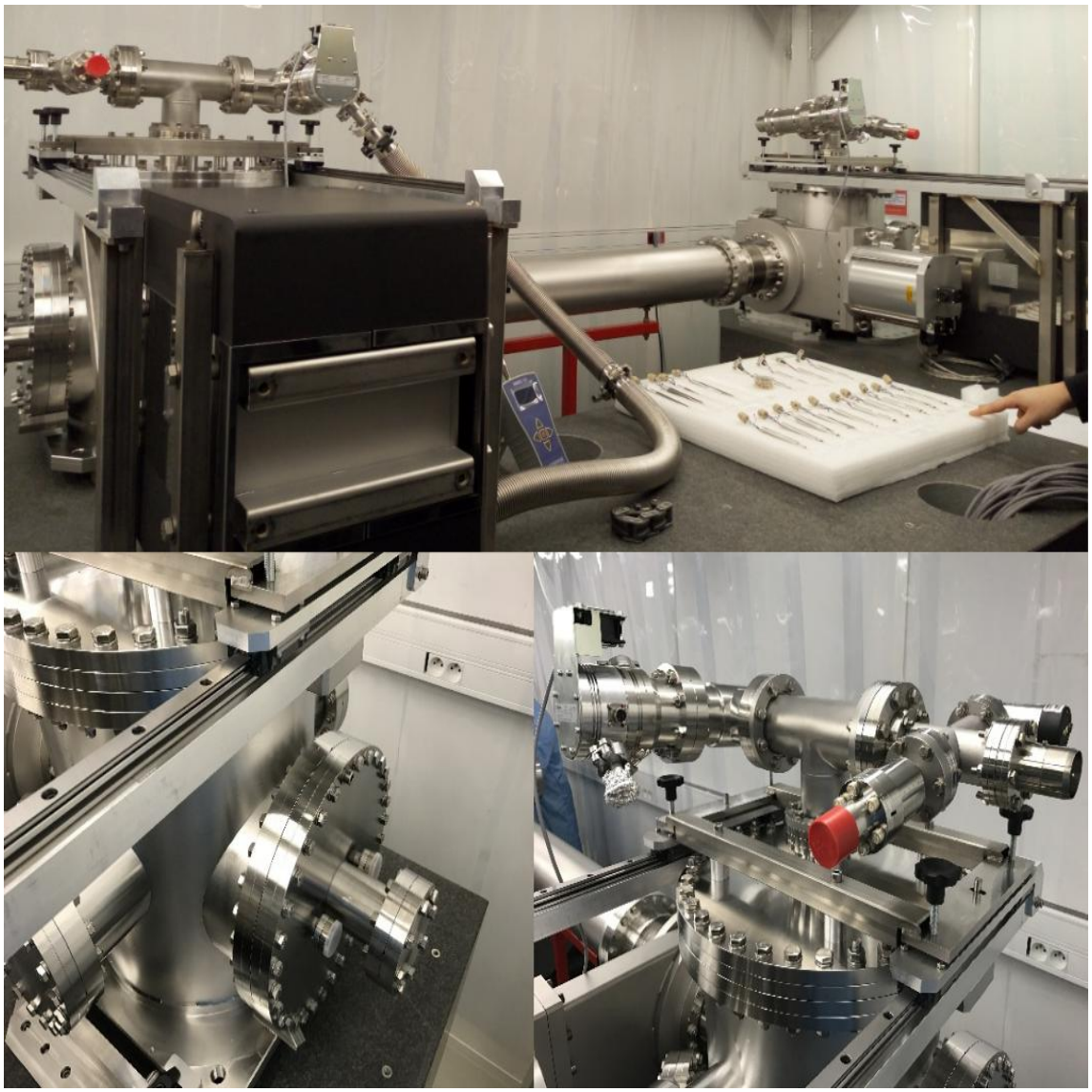

Figure 4.17 Installation of the vacuum system for ThomX.

consisting of several lenses to match the mode in the cavity.

4.2.1 Telescope Design

In Section 4.1.4, the cavity parameters of Cavity P178a are reported. In addition, we measured the waist size and position of the input beam after the amplifier as described in Section 4.1.2. Our goal is to design a telescope consisting of four cylindrical lenses to match the beam size and divergence in the cavity. As shown in Figure 4.10, the beam size varies little except while propagating between the two spherical mirrors. Hence, the telescope is designed to match the input beam to the beam size and divergence at the center of the two planar mirrors. Cylindrical lenses are used for high-efficiency mode adaption. Four cylindrical lenses with different focal lengths and located at different positions are designed as shown in Figure 4.18.

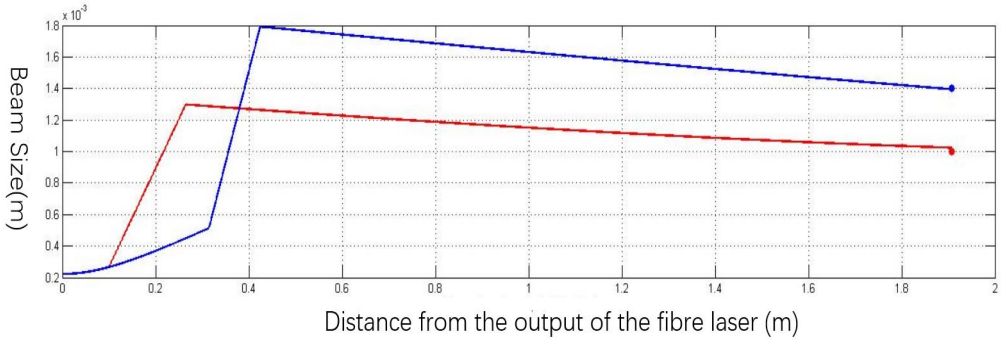

Figure 4.18 Telescope design consisting of four cylindrical lenses. The red and blue points correspond to the tangential and sagittal targets, respectively.

4.2.2 Coupling Measurement

In this subsection, the Menlo Orange pulse laser is used to inject into Cavity P178a. The coupling of the S-Box cavity P178a, with a finesse of $F = 3,000$, was measured at a laser output of 25 W. The coupling can reach as high as 80%, as shown in Figure 4.19, with the use of the telescope designed above. When the laser is not locked to the cavity, the pink curve (corresponding to the reflected beam from the cavity) remains maximal, which means that almost all of the input laser beam is reflected. After the laser is locked to the cavity, the reflected beam decreases to 20% of its former intensity. The power stored in the cavity is high, approximately $25 \times 0.8 \times 1000 = 20$ kW. Once the cavity has

been locked at high power, it is necessary to perform the alignment again to improve the coupling.

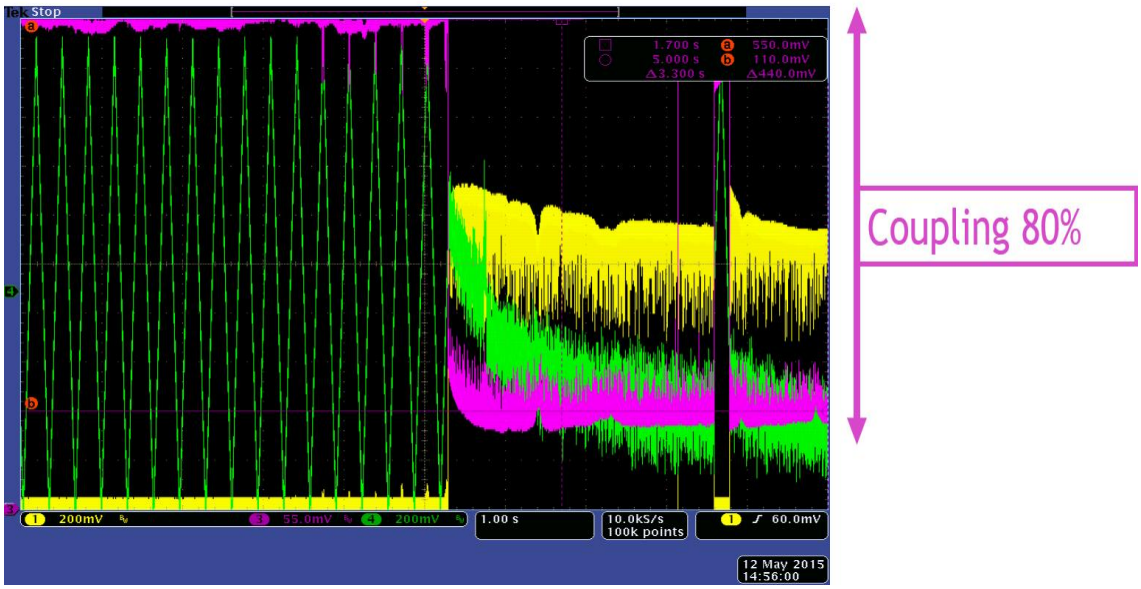

Figure 4.19 Coupling measurement. The left side of this figure corresponds to the unlocked case, and the right side corresponds to the locked case. The pink curve is the reflected beam from the cavity. The green curve represents the piezo voltage that is used to tune the laser cavity length. The yellow curve shows the cavity transmission.

4.3 Finesse Measurements

The finesse of the cavity was measured using several methods to compare the experimental and theoretical values. These two values may differ because particles may have been deposited on the surfaces of the cavity mirrors during transit or installation in the clean room. Such deposited dust will tend to increase the diffusion and absorption coefficients of the cavity mirrors. As a result, the theoretical value is an upper limit, and the experimentally measured finesse will always be lower. During our tests, we used four different measurement methods[139–143]. The use of multiple methods helps to ensure a correct measurement result.

We used the low-phase-noise NKT Koheras CW laser oscillator introduced in Section 4.1.1 in order to achieve better repeatability of our results than would have been possible with the Menlo Orange pulse laser oscillator. The prototype S-Box Cavity P178b used for these tests had a theoretical finesse of $F = 28,000$ and was constructed using the cavity mirrors manufactured for the ThomX project. The first two measurement methods

were performed in closed-loop mode, that is, with the laser oscillator locked to the cavity, whereas the other two methods were performed in open-loop mode.

4.3.1 Decay Time Method

The decay time method[139] is performed in closed-loop mode. Power is first accumulated in the cavity; then, the incident laser beam is shut off, and the cavity is allowed to empty of photons. This measurement is thus directly related to the losses of the cavity. If we use t to denote the time at which we shut off the incident power, then the intracavity field after one round trip can be written as follows in accordance with the losses of the mirrors:

$$e(t + \tau_{FP}) = \rho e(t) \tag{4-1}$$

where ρ denotes the product of the reflection coefficients of the cavity mirrors in the field. We can rewrite Equation 4-1 in the form of a differential equation:

$$\begin{aligned} e(t) + \tau_{FP}\frac{\partial e(t)}{\partial t} &= \rho e(t) \\ e(t) &= \exp\left(-(1-\rho)\frac{t}{\tau_{FP}} \right) \end{aligned} \tag{4-2}$$

However, the quantity that is experimentally measured by the photodiode will be the intensity, or power, of the beam. Thus, we have

$$P(t) = \exp(-t/\tau) \tag{4-3}$$

where $\tau = \tau_{FP}/2/(1-\rho)$ is the cavity decay time. Once we obtain the decay time, the finesse can be calculated.

To allow us to measure the time required for the cavity to empty, the CW laser beam must be shut off very quickly. An AOM (acousto-optic modulator) do the trick. This device consists of a crystal excited by an acoustic wave, which causes a frequency shift of the laser. The cut-off time of this device is very short, on the order of nanoseconds, which makes it possible to measure the emptying time. The result is presented in Figure 4.20. The incident signal is shown in black. The transmitted signal is shown in blue, and the fit curve is plotted in red. The emptying time measured here is 22 μs, corresponding to $F = 24,700$.

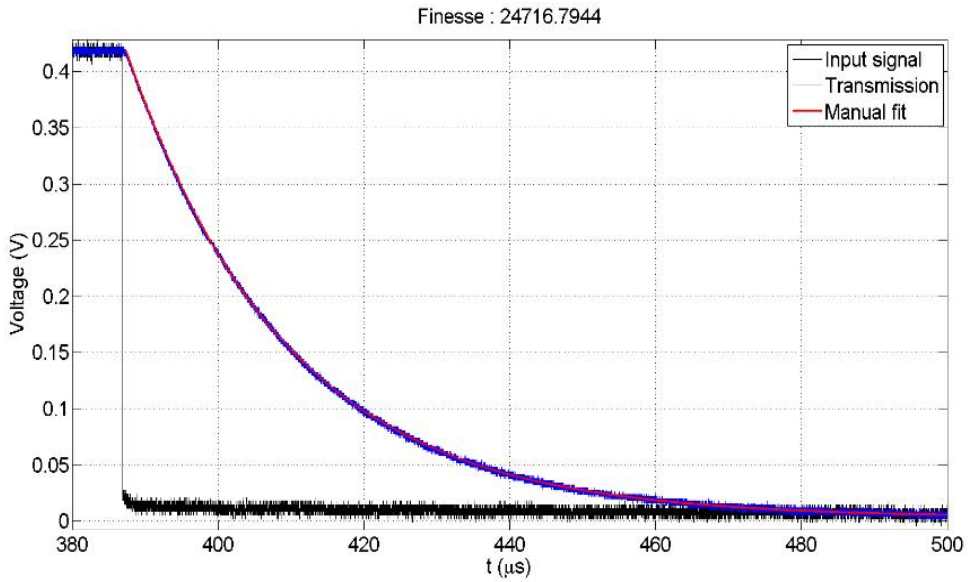

Figure 4.20 Measurement of the decay time of the optical cavity. The curve in black is the incident signal. The curve in blue corresponds to the signal transmitted through the cavity. The transmission fit curve, in red, coincides with the blue curve.

4.3.2 Electro-Optic Modulator (EOM)-Based Frequency Modulation Method

This method is based on Reference[141]. The idea is to determine the free space range and the bandwidth of the cavity and divide one by the other, as in the definition of the finesse. This technique uses the property that the interval of the cavity resonance frequency is equal to FSR. When the optical frequency is shifted by FSR, the resonance condition is still met. In this method, the laser oscillator is locked to the cavity, and the laser beam is modulated in phase at a frequency close to FSR.

Through an EOM (electro-optic modulator) frequency modulation of $\Omega = FSR$, each lateral sideband Ω, $2\Omega, \cdots$, can also be accumulated in the Airy peak of the cavity, and the resonance will be maximal. However, when the modulation is varied around FSR, some lateral bands will no longer be coupled to the Airy peak, and the stored power will decrease. Thus, by sweeping the resonance, one can reconstruct the Airy function. This makes it possible to precisely measure FSR and the cavity linewidth.

Figure 4.21 shows the experimental setup. EOM1 is used to generate the error signal. EOM2, modulated around FSR, is used to sweep the resonance in order to reconstruct the Airy function. The speed of the frequency sweep is approximately 100 Hz per 50 ms. This scan gives the conversion ratio from the oscilloscope timebase to the frequency domain of the cavity. Finally, we obtain the curve shown in Figure 4.22, which gives the Airy

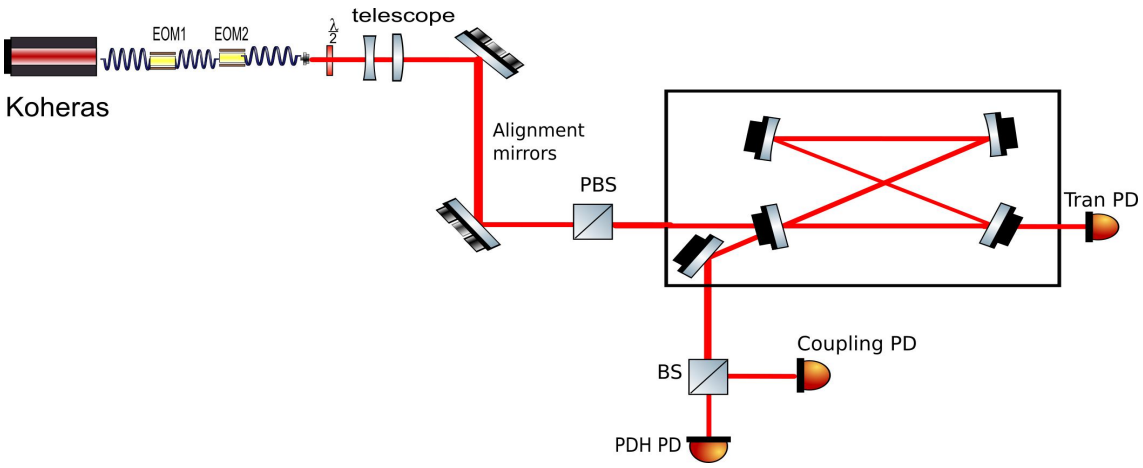

Figure 4.21 Schematic illustration of the experimental setup for measuring the finesse using the EOM-based method. EOM1 is used to generate the PDH error signal. EOM2 is used to modulate the laser beam in phase at a frequency close to FSR.

function of the cavity as detected by the transmission photodiode. This measurement method yields an FSR of 178.38 MHz and a linewidth of $\delta\nu$ = 7.1 kHz. Hence, the finesse is 25,100.

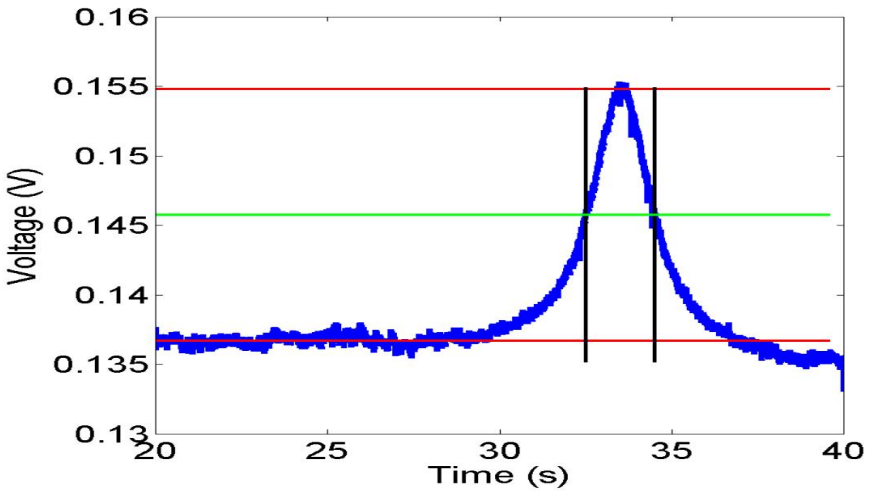

Figure 4.22 Finesse measurement results. The obtained cavity Airy function corresponds to FSR = 178.38 MHz and a linewidth of 7.1 kHz.

4.3.3 Cavity Ring-Down Method

In this method, the finesse is measured by rapidly varying the optical frequency of the laser beam and measuring the emptying time of the cavity[140]. The PZT (piezo-electric transducer) of the oscillator thus plays the role of an on/off switch. The goal is not to

observe the Airy function but rather to fill and empty the cavity. Consequently, the scan speed of the PZT is crucial. The scan speed must be much faster than the emptying time of the cavity. This method has the advantage of not requiring costly optical elements, such as EOMs or AOMs. The experimental setup is shown in Figure 4.23.

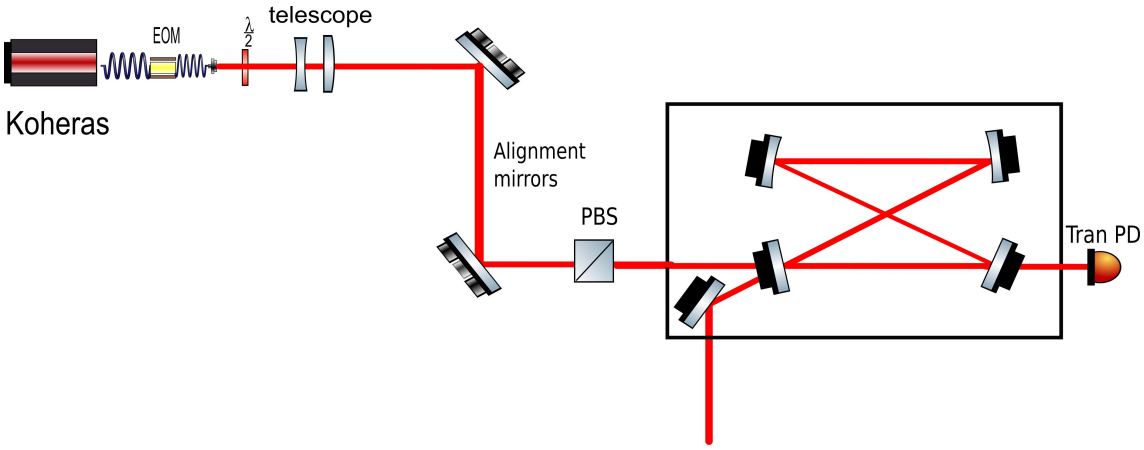

Figure 4.23 Experimental setup for measuring the finesse using the ring-down method. The cavity is operating in open-loop mode.

However, this method requires a very fast scan speed. Hence, the filling time of the cavity should be very short to ensure a sufficient signal during the emptying process. This method is therefore more effective for a low-finesse cavity. Nevertheless, we applied it to our high-finesse cavity here to obtain the results shown in Figure 4.24, from which we ultimately obtained a finesse of 26,600.

4.3.4 Ringing Effect Method

When the cavity resonance is swept by the oscillator PZT with a period τ_{PZT} on the order of the time spent by a photon in the cavity, $\tau_{cav} \simeq FL_{cav}/(2\pi c)$, a ringing effect can be observed in the cavity transmission[142,143]. This is a purely dynamic effect, stemming from the fact that the cavity does not have sufficient time to reach a steady state at each position of the PZT. The intracavity field thus interferes with the incident laser field and causes oscillations, as shown in Figure 4.25.

A semianalytical expression describing this phenomenon was derived in Refer-

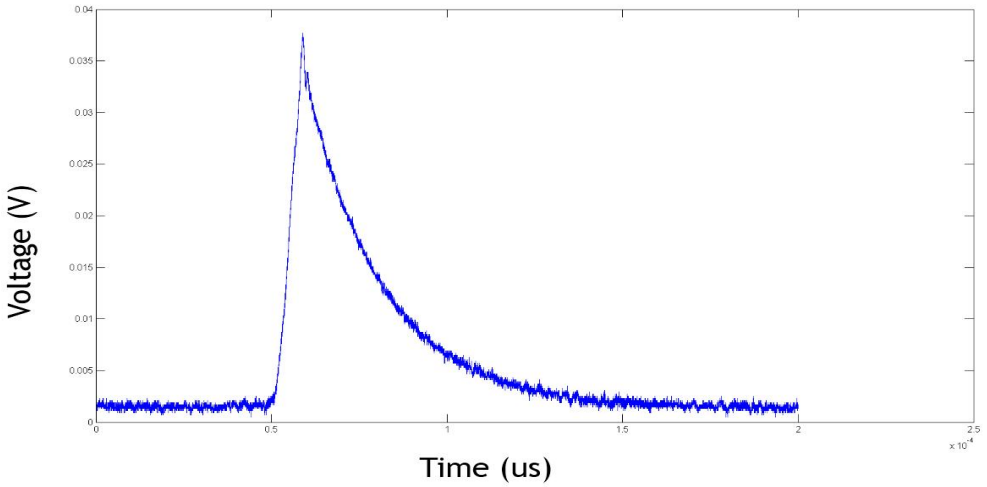

Figure 4.24 Experimental result of the ring-down finesse measurement.

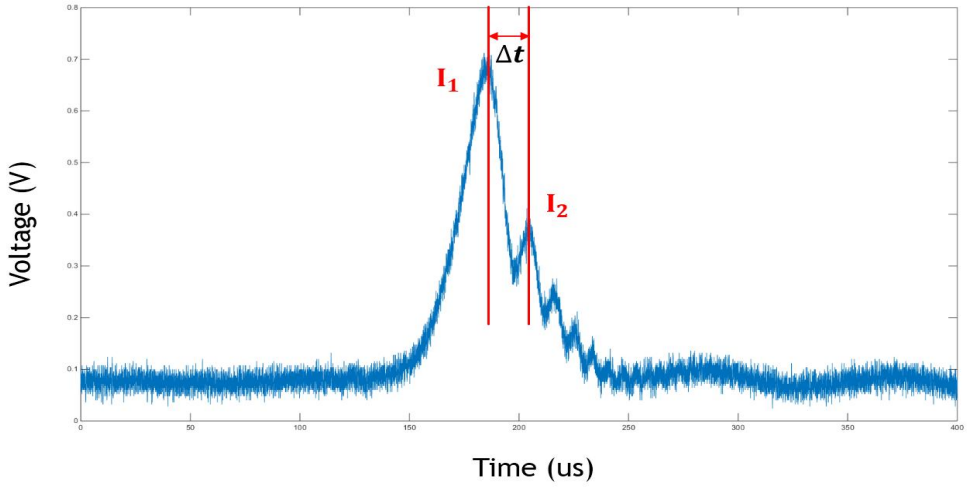

Figure 4.25 Cavity ringing effect used to measure the finesse.

Table 4.3 Values of finesse measurement

Theoritical value	28,000
Decay time method	24,700
EOM-Based frequency modulation method	25,100
Ring-down method	26,600
Ringing effect method	27,700

ence[142]:

$$\frac{2\pi c}{L_{cav}\triangle t} = \frac{F}{2}\left(\frac{I_1}{I_2} + 2 - e\right) \tag{4-4}$$

where I_1 and I_2 are the intensities of the first and second peaks, respectively, due to the ringing effect and $\triangle t$ is the time interval between the two peaks. We obtained a finesse of 27,700 using this method. This method is appropriate for high-finesse cavities ($> 1,000$) with a good signal-to-noise ratio.

4.3.5 Comparison of the four methods

Table 4.3 summarizes the finesse values obtained by each method. We also reminds that the theoretical finesse of the cavity is 28,000.

The measurement with decay time method seems to be the most reliable. It implies a very rapid extinction of the incident signal, which is the case on our experiment shown in Figure 4.20. Because the losses of the cavity are observed directly without external intervention. The EOM-Based freqency modulation method is also reliable because we scan exactly the Airy function of resonance. This technique also makes it possible to go back to optical length of the cavity. The ring-down method requires very fast sweeping speeds, which does not leave the cavity time to fill up. However the noise introduced by the PZT on the measure is unknown to us. The ringing effect method seems to be the least reliable. We face the same noise problem as the ring-down measurement. In addition, the semi-analytical model limits the space of usable signals.

In conclusion, the decay time method and EOM-Based freqency modulation method are more reliable.

4.4 Influence of Dust on Finesse

Dust deposited on the cavity mirror surfaces has a great effect on the cavity finesse, which can lead to an enormous decrease in the cavity gain. The experimental setup in Figure 4.26 is used to image the surfaces of cavity mirrors. Two lens are used to match the laser beam size to the sizes of test mirrors. The scattering laser caused by the scattering of dust on the test mirrors can be accumulated by the camera. The whole experiment was done in a dark room. We measured the surfaces of the cavity mirrors of ThomX and another cavity named Mightylaser, as shown in Figure 4.27. The ULE mirrors of ThomX are new, and we can see that the mirror surfaces are very clean. The luminous regions near the edges of each mirror in Figure 4.27 correspond to reflection from the mirror mounts. By contrast, the surfaces of the Mightylaser cavity mirrors are somewhat dirty because they have been in use for a long time, and some small amount of dust has been deposited in the centers of these mirrors. We attempted to clean the Mightylaser mirrors by wiping them with lens cleaning tissues and using First Contact cleaner[144], which is specially designed for cleaning precision optics, mirrors and surfaces in use. Unfortunately, it was impossible to clean the Mightylaser cavity mirrors to the level of those of ThomX. It is possible that these mirrors were damaged under high laser power.

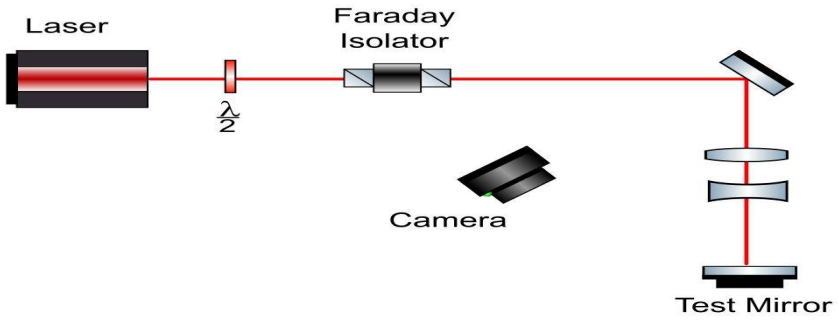

Figure 4.26 Experimental setup for imaging the surface of the test mirrors.

The finesse measurements using the ThomX cavity mirrors are described in Section 4.3. The experimental finesse is approximately 26,000, very close to the theoretical finesse of 28,000. By contrast, the finesse of the Mightylaser cavity is approximately 9,000, which is much lower than its theoretical value of 40,000. These findings provide an intuitive understanding of the effect of dust on the cavity finesse.

To keep the optical setup clean and avoid the deposition of dust on the cavity mirrors, it is necessary to take several steps. In addition to using an ultra-clean vacuum chamber,

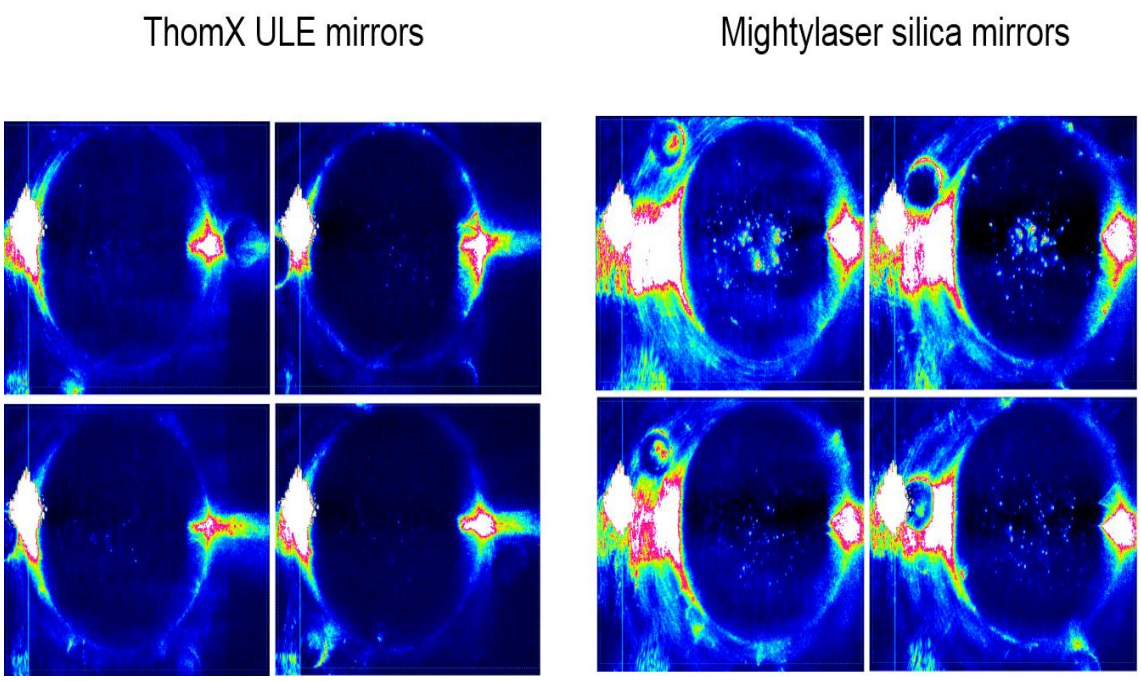

Figure 4.27 The surfaces of the cavity mirrors of ThomX are shown on the left. The surfaces of the cavity mirrors of Mightylaser are shown on the right.

we also assemble all parts and perform all experiments in a clean room. Before bringing any element into the clean room, we clean it with acetone and alcohol. In addition, we use a nitrogen-based ionizing pistol to remove residual particles. A full clean suit, including hat, gloves and body suit, is necessary for all personnel working in the clean room, as shown in Figure 4.28.

Figure 4.28 During experimental work, one must wear a hat, gloves and a clean body suit in order to keep clean.

4.5 High-Power Experiments on the S-Box Prototype

Our group performed several high-power experiments on the prototype S-Box Cavity P133 shown in Table 4.2. The experimental setup is shown in Figure 4.29. Before entering the amplifier, the laser pulse duration is stretched from 200 fs to 250 ps by a CVBG in order to limit nonlinear effects. After reflected by the CVBG, the laser beam is injected into an optical fiber. The output power of the amplifier can reach as high as 40 W. The injected laser beam is coupled to the cavity after passing through the four-cylindrical-mirror telescope. A PDH error signal is used to lock the laser to the cavity. The cavity finesse is approximately 26,000. The repetition frequency of the Onefive oscillator is 133 MHz.

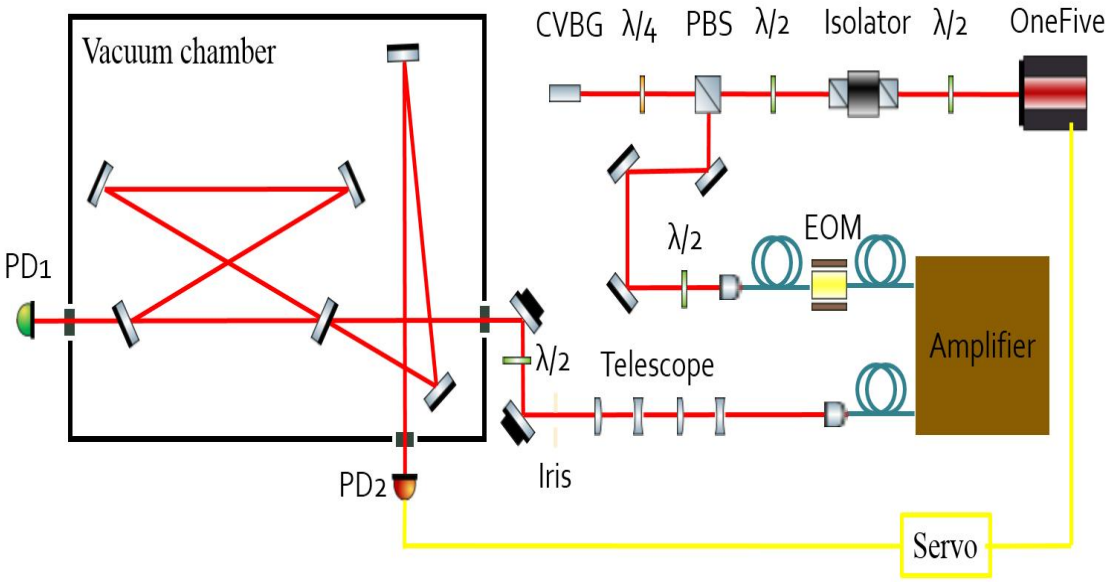

Figure 4.29 Schematic illustration of the setup for the high-power experiments. The red line represents the light path. The yellow line represents the electrical signal.

The transmission coefficients of cavity mirrors were measured to determine the stored power in the cavity. After removing the coupling mirror M1 shown in Figure 4.29, the transmission of M4 was obtained by performing the ratio between the transmitted power and the incident power. Since the reflectivity of the coating also depends on the incidence angle, the alignment of cavity mirrors makes it possible to measure the transmission in its final position. Finally we have: T_4=2.85 ppm.

We locked the oscillator to the cavity and observed some strange mode shapes at different powers, as shown in Figure 4.30. When a low amount of power is stored in the cavity, the mode seems to be TEM_{00}, and it is very pure. At higher powers (50 kW and

70 kW), it seems that the TEM_{00} mode overlaps with higher-order modes. It seems to be a superposition of Hermite-Gaussian HG_{00} and HG_{mn} modes (m,n≠0). The modal instabilities[145,146] restricts the stacked power in the cavity to approximately 70 kW and strongly limits the coupling.

We believe that this effect originates from cavity modal frequency degeneracy induced by thermal effect[147,148]. Thermoelastic deformation in mirror curvature changes the resonance frequency of all cavity modes[52]. In addition, the mirror deformation and the heating of mirror mounts from the scattering at high power would lead to the misalignments and a change in the distance between spherical mirrors. These lead to the cavity high-order mode resonating in the bandwidth of the optical cavity, which is extremely narrow in our experiments. Cavities of higher finesse should be less sensitive to this effect since their bandwidth is smaller.

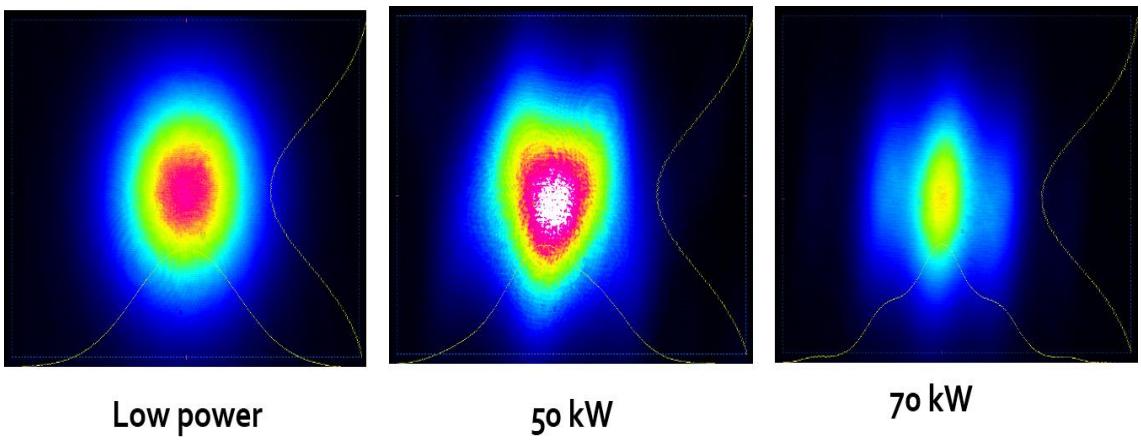

Figure 4.30 Beating of transverse modes at different powers.

Possible strategies were studied to avoid the mode instabilities in Reference[149,150]. A detailed model was developed to explain the high-order modes generations caused by mirror surface defects and their resonance inside an optical cavity. Reference[149] showed that it is sufficient to correct for the high-order modes which are close to resonance by using a reduced number of mirror maps. Based on the maps, an algorithm of the optimal corrections was developed and this method only used the laser beam powers without any knowledge of the cavity mirrors surfaces[149]. In addition, the quality of the reflected beam from the optical cavity with realistic mirror surface maps has been tested by optical simulations in Reference[150]. The injected beam mode is Laguerre-Gauss $LG_{3,3}$ and the purity of reflected beam recovered from below 90% to 99.96%.

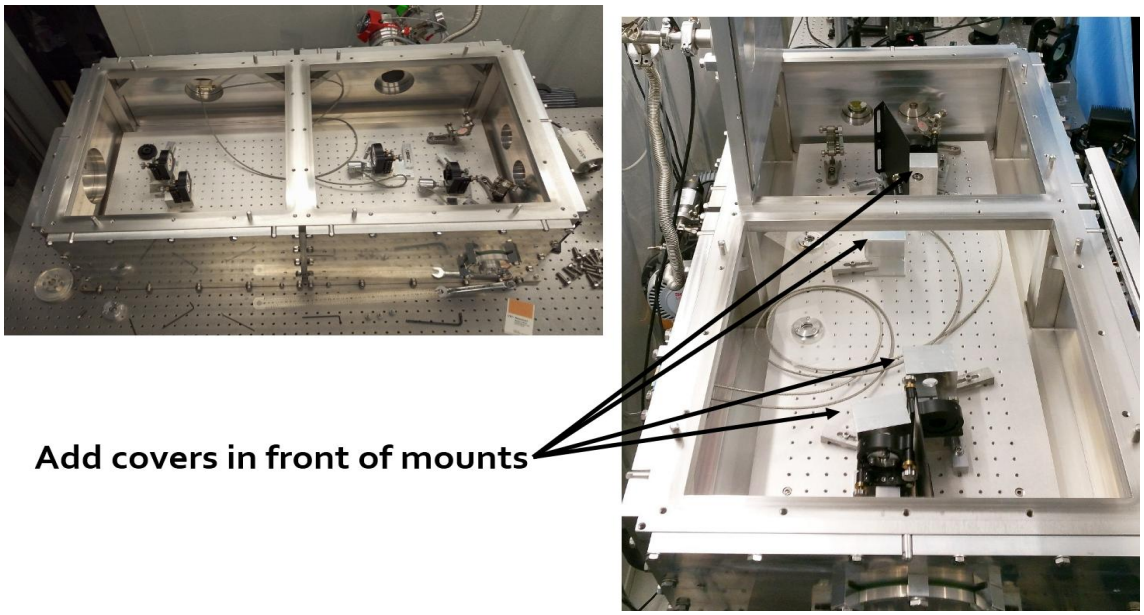

Figure 4.31 S-Box cavity after the addition of covers in front of the mirror mounts.

We also have tried to reduce this effect experimentally. To prevent the scattered light reaching the mounts, we placed aluminum covers in front of the mirror mounts, as shown in Figure 4.31. All these covers proved very useful, and made it possible to repel the arrival of thermal effects and increase considerably the stored power. After the placement of the covers, we achieved a stable power as high as 383 kW and reached a maximum power of 400 kW for several seconds, with a cavity gain of 10,000. The power stored in the cavity is plotted as a function of the input power in Figure 4.32.

To achieve such performance, it is necessary to realign at every step. This is because under high power, the cavity loses alignment very quickly. At some point in the measurements represented in Figure 4.32, we could no longer correct for the misalignment to continue increasing the power. In fact, we were not limited by the amplifier, but we nevertheless could not stack more power in the cavity. It is still an open question.

Another group at the Max Planck Institute in Germany[151] achieved 670 kW in their cavity, but they used a low-finesse cavity and a high input laser power. Their system is much more expensive than ours. Ours is more complex and difficult to operate, mainly because of the feedback loop.

In brief, we obtained 400 kW power stored in the cavity in pulsed regime by using a cavity with finesse 26,000 and modal instabilities which limit this power were observed.

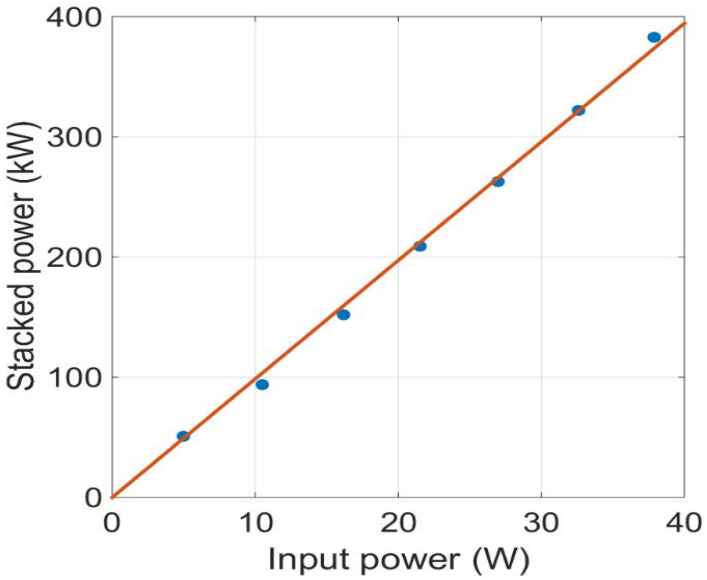

Figure 4.32 Measured power stored in the cavity as a function of the injected laser power.

Chapter 5 Design of a Prototype Cavity for TTX2

Tsinghua University hosts a compact low-repetition-frequency X-ray source called TTX, which is based on a linac system and a terawatt femtosecond laser system. X-ray flux reached 1.2×10^5 per collision during experiments. However, this machine must operate at a low repetition frequency . For some applications, high-repetition-rate X-ray machine are prefered.

Hence, the next step of the project will be to upgrade TTX to a high-repetition-frequency X-ray machine named TTX2, consisting of an optical cavity and an electron storage ring. In this chapter, we present a prototype optical cavity for TTX2 that was designed at Tsinghua University in order to gain the necessary experience for this upgrade. The pulse laser and the amplifier used for the prototype cavity will be introduced briefly, the mechnical design and the cavity parameters are also presented here.

For the final TTX2, it is full of challenges. First of all, we should overcome the difficulty of thermal effect discussed in Chapter 4 in order to obtain a high-average-power optical cavity. Modal instabilities must be studied in details and we should optimize the geometrical design of optical cavity. In addition, the mechanical vacuum design after intergrating the electron ring will also be challenging. These aspects will not be discussed in this dissertation.

5.1 Pulse Laser and Amplifier

The pulse laser used for injection into the cavity and its amplifier were manufactured by the Chinese Academy of Engineering Physics. A schematic diagram is shown in Figure 5.1, and the system is very compact, as shown in Figure 5.2. In addition, two actuators are used to tune the repetition frequency. One is a motorized stage used for wide-range tuning, and the other is a high-speed PZT (piezo-electric transducer) for fine tuning to lock the laser to the cavity.

The oscillator is used to generate the laser pulses, and its repetition frequency is 79.3 MHz, corresponding to an optical cavity length of 3.78 m. Its performance indicators have been measured as follows. The power after the oscillator is approximately 85.1 mW, and the power after the amplifier can reach a maximum of 10.9 W. The central wavelength after the oscillator is 1063.90 nm, with a FWHM (full width at half maximum) of 2.97

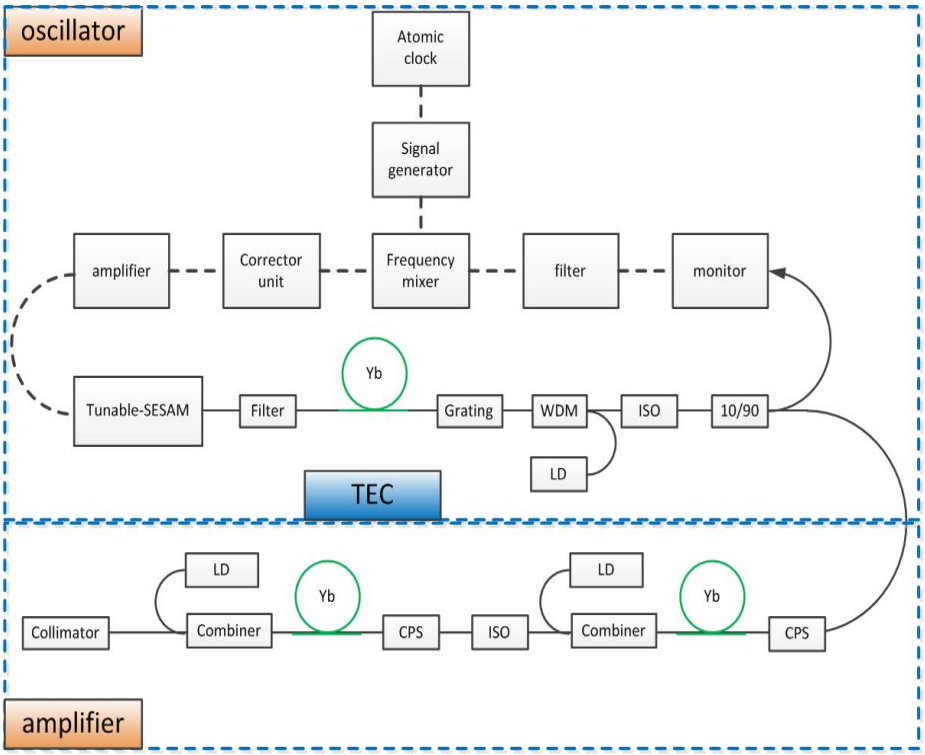

Figure 5.1 Schematic diagram of the oscillator and amplifier.

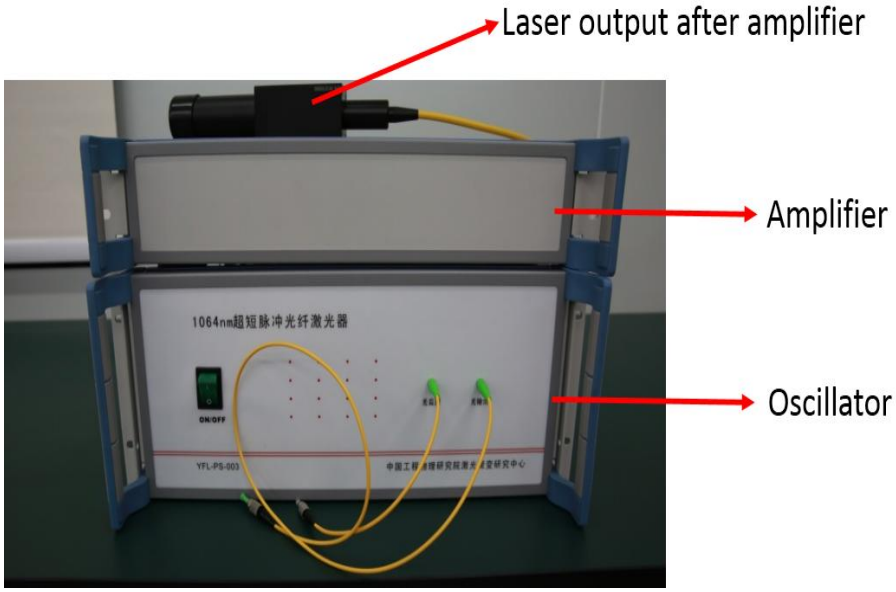

Figure 5.2 Photograph of the oscillator and amplifier.

Table 5.1 Parameters of the pulse laser

Wavelength (nm)	Pulse duration (ps)	Output power (W)	Repetition rate (MHz)
1064	9.7	~ 10	~ 79.3

nm. The laser pulse duration is approximately 9.7 ps. The beam quality is still acceptable after the amplifier, with M^2 values of 1.382 in the horizontal direction and 1.18 in the vertical direction. The parameters are summarized in Table 5.1.

5.2 Design of the Prototype Cavity

The optical cavity is a key part of the prototype cavity system. The system has many performance requirements, such as a small transverse waist at the interaction point, cavity mirrors with high reflectivity but low internal losses, a strong and robust feedback system, and sufficient compactness for integration into an accelerator environment. In the following subsections, we describe the cavity parameters, the vacuum vessel system and other requirements.

5.2.1 Cavity Parameters

For our design, we chose the 4M (four-mirror) 2D (two-dimensional) bow-tie optical cavity shown in Figure 5.3. A two-mirror concentric cavity is simple, but it is known to be mechanically unstable compared with a 4M cavity. In addition, the 4M 2D cavity is more compact and easier to integrate with the electron storage ring than a three-dimensional cavity would be.

In Figure 5.3, M1, which acts as the coupling mirror, and M2 are planar mirrors. Two spherical mirrors M3 and M4 have the same radius of curvature ρ. The design parameters are presented in Table 5.2. Figure 5.4 shows the schematic drawing of the designed cavity.

Commercial cavity mirrors from LAYERTEC were chosen for the first step of the prototyping process. Because precise mirror reflectivities cannot be guaranteed for commercial products and we estimated the finesse to be approximately 2,000, we designed the cavity to operate in the overcoupling regime as shown in Figure 5.5. This figure shows the cavity finesse and gain as functions of the transmission of M1. To the left of the impedance matching point, the gain drops much more rapidly than it does in the overcoupling regime.

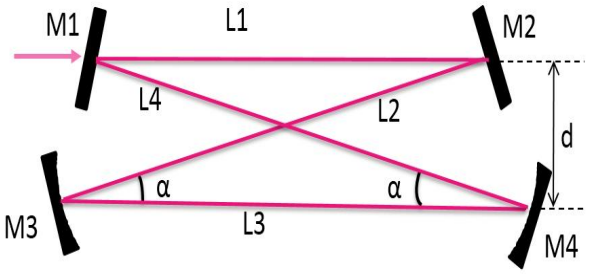

Figure 5.3 Schematic diagram of a 4M 2D bow-tie cavity.

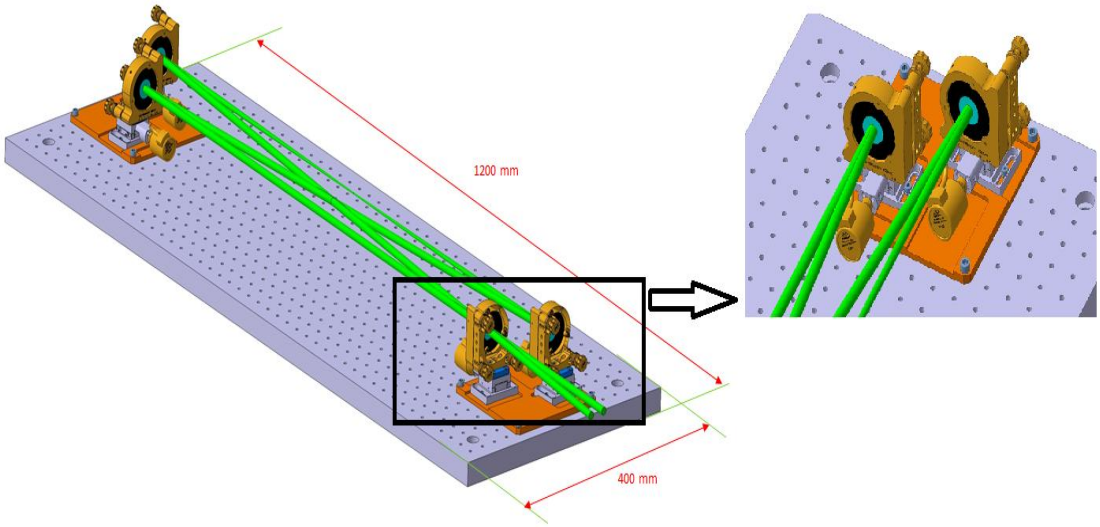

Figure 5.4 Schematic drawing of the prototype cavity for TTX2. The cavity is mounted on a 1200 mm × 400 mm breadboard, and a zoomed view of one cavity mirror section is shown on the right.

Table 5.2 Design parameters of the prototype cavity

L1 (mm)	L2 (mm)	L3 (mm)	L4 (mm)	d (mm)	ρ (mm)	α (degree)
882.12	947.44	1006.0	947.44	80	1000	4.844

Hence, it is preferable for the cavity to operate in the overcoupling regime because of the inaccuracy of the mirror reflectivity.

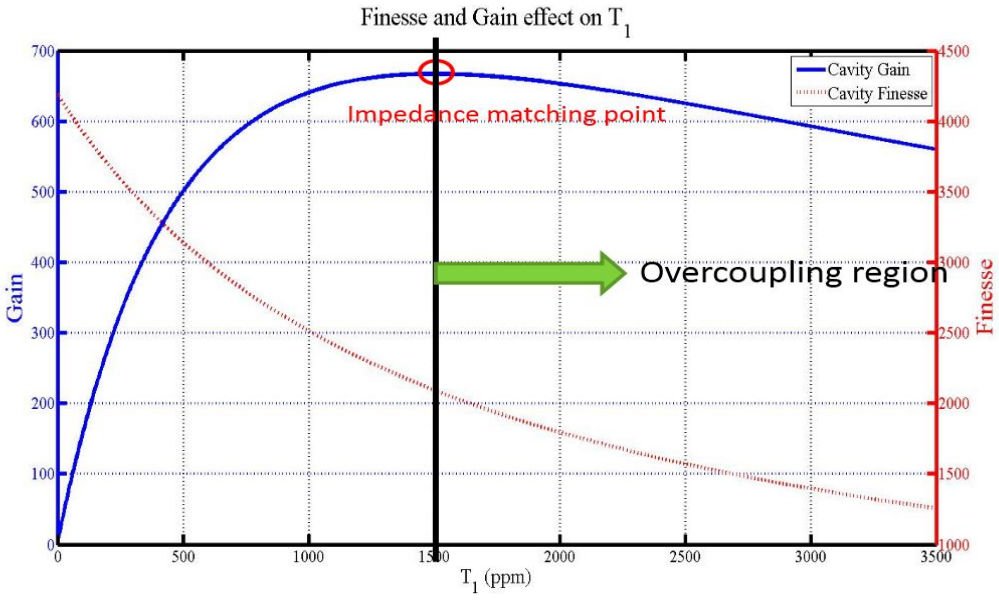

Figure 5.5 Cavity finesse and gain as functions of T1.

The beam size and wavefront radius of curvature along the propagation direction are presented in Figure 5.6. The small waist, with sizes of approximately 100 μm in both directions, is located in the center of the two spherical mirrors, corresponding to an infinite wavefront. The sagittal and tangential beam sizes on M1 are w_s = 1.8 mm and w_t = 1.65 mm. The cavity must be operated very close to the unstable region to achieve such a small waist.

5.2.2 Feedback System

To lock the laser to the cavity, a strong and robust feedback system is needed. We use the conventional PDH technique to lock the repetition frequency of the laser to the FSR of the cavity. For this purpose, we chose the commercial product Digital LaseLock from TEM Messtechnik. LaseLock is a universal and compact laser stabilization electronics (lock-box) that allows to stabilize tunable lasers (e.g. diode lasers, Ti:Sapphire or dye lasers)

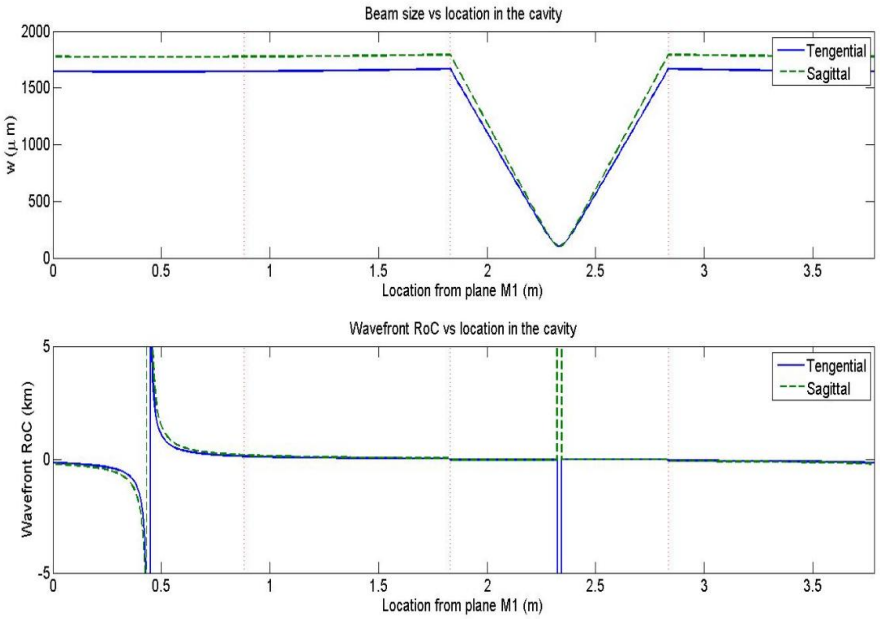

Figure 5.6 The beam size and wavefront radius of curvature along the propagation direction.

in their frequency. For this, particularly optical resonators (Fabry-Perot cavities) and atomic absorption or fluorescence lines are serving as references. Vice versa, also optical resonators can be stabilized towards a given laser frequency by means of mechanical actuators (e.g. piezo actuators). Good performance has been achieved during testing at LAL (Laboratoire de l'Accélérateur Linéaire), University of Paris-Saclay. This product satisfies the requirements for the prototype cavity for TTX2.

5.2.3 Mechanical Design of the Prototype Cavity

The prototype cavity must be installed in vacuum. Its vacuum vessel, presented in Figure 5.7, is similar to that of S-Box. The vessel consists of aluminum panels with seals and stainless steel frames. Four two-inch laser windows are used to measure the coupling and transmission. The top of the vacuum vessel hosts a pumping port, a gauge port and two viewports. The motor feedthroughs are on the side.

5.2.4 Other Requirements

Because the energy that can be stored in this cavity is not sufficiently high, the thermal effect may not be evident. However, the final goal is to achieve high finesse and high gain. Hence, it is necessary to consider the thermal effect. To avoid heating of the cavity mounts

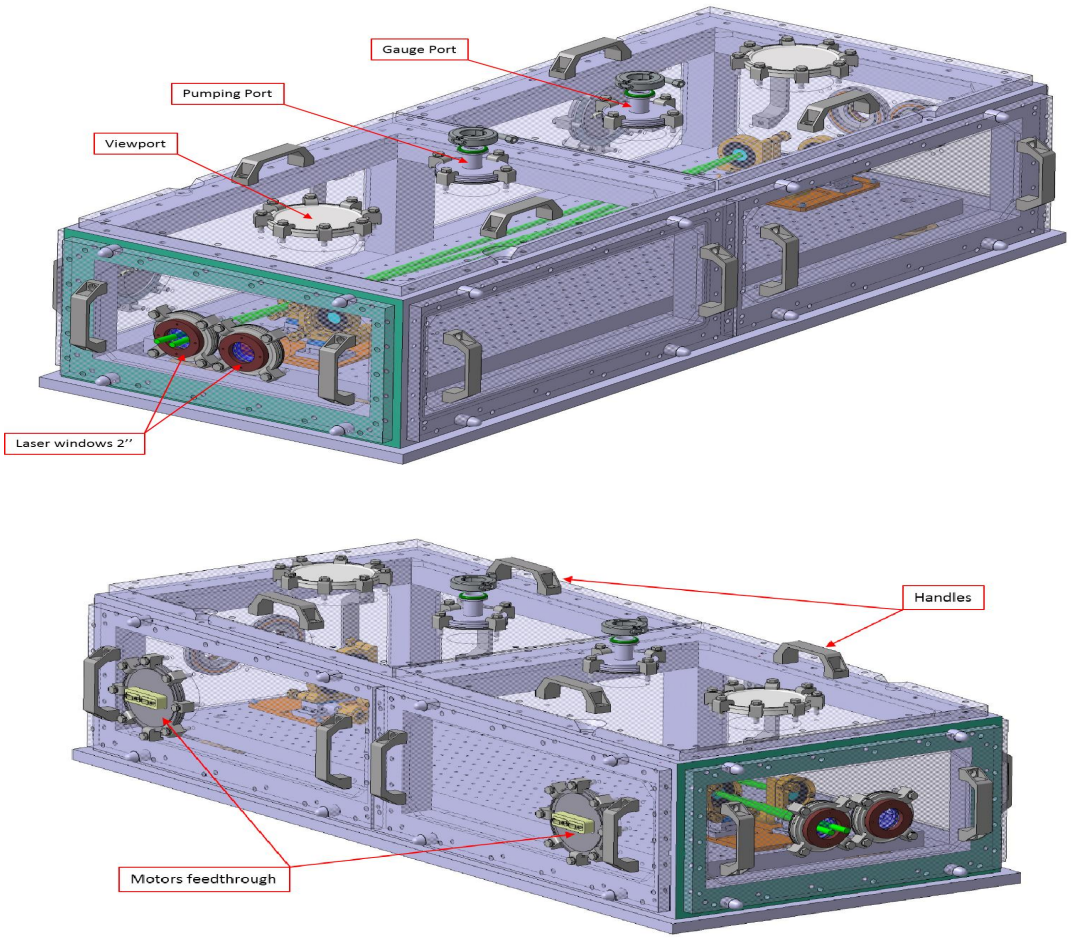

Figure 5.7 Vacuum vessel for the prototype cavity for TTX2 from two different points of view.

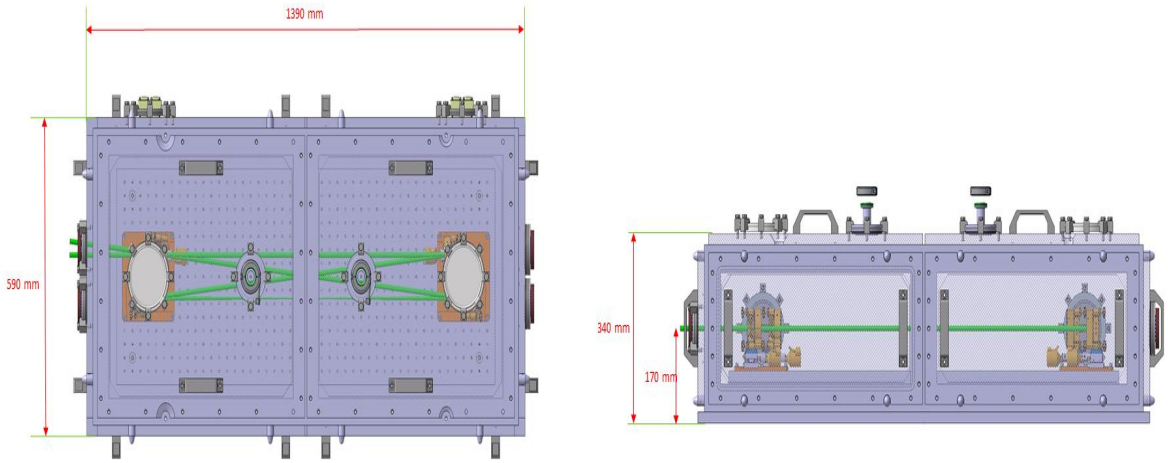

Figure 5.8 Top view (left) and side view (right) of the vacuum vessel.

due to scattering, we use thermal-drift-compensating mounts. These mounts feature a combination of zero-drift thermal drift compensation and low-wavefront-distortion mirror mounting[152]. Because the thermal deflections of the optical mounts can be characterized and these deflections can then be controlled through thermal expansion compensation, the thermal deflection of the optical mounts can be nearly eliminated.

Cleaning is another extremely important factor. The cavity should be assembled in a class 100 clean room, corresponding to ISO class 5. We have discussed the effect of dust on cavity finesse in Chapter 4.

Chapter 6 Concluding Remarks

In this dissertation, we described a compact laser-electron interaction apparatus which is expected to produce a higher flux of better-quality X-rays compared with traditional X-ray sources. It can bridge the gap between conventional X-ray sources and synchrotrons or free-electron lasers, thereby lower the barrier to entry for X-ray-based research. As the core component of such a laser-electron X-ray source, a high-average-power optical enhancement cavity for Thomson scattering experiments is studied.

The laser pulse stacking technique plays an important role in our compact X-ray source. We developed a precise model to describe the transient stacking process considering time detuning and the carrier-envelope phase effect. We found that for the same cavity gain, a higher-finesse but detuned cavity has a wider linewidth than a lower-finesse cavity without any detuning, meaning that it is easier to lock a laser to the former.

General astigmatic beams may occur in misaligned four-mirror planar cavities. Astigmatic cavity is described and explicit expression for the second order correction was derived by solving Lax perturbation series of the wave equation for general elliptic Gaussian beams. Remarkably S-shaped beam modes appear as the beam propagates away from the cavity symmetry point. This feature agrees qualitatively with observations made on a highly divergent non-planar four-mirror cavity.

Various locking methods are summarized in this dissertation in order to compensate all the noise. We propose a new laser frequency stabilization technique that relies on the polarization property of the cavity and tuning of the cavity mirror reflectivity. A specialized design of the coating layers of the cavity mirrors and a non-nominal laser incidence angle result in sufficient s- and p-wave phase detuning to generate two resonance peaks in the cavity, which give rise to an error signal that can be used for locking. Compared to the traditional PDH method, this technique is simpler without need for frequency modulation and demodulation.

To achieve the final goal of a high X-ray flux, an extremely high level of power must be stored in the cavity. The deformation of the cavity mirrors induced by the high laser power causes changes to the mirror surfaces. We find that the gain is extremely sensitive to this deformation. Hence, a strong feedback and ultra-low expansion mirrors to minimize this deformation are really necessary.

High-power experiments were performed on a prototype cavity for ThomX. A cavity finesse of approximately 26,000 was measured using four different methods, and the deposition of dust on the cavity mirrors was found to considerably reduce the finesse. We obtained 400 kW power stored in the cavity in pulsed regime by using a cavity with finesse 26,000 and modal instabilities which limits this power were observed. We believe that this effect originates from cavity modal frequency degeneracy induced by thermal effect.

Tsinghua University hosts a compact low-repetition-frequency X-ray source called TTX, which is based on a linac system and a terawatt femtosecond laser system. The next step of the project will be to upgrade TTX to a high-repetition-frequency X-ray machine named TTX2, consisting of an optical cavity and an electron storage ring. Similar to the prototype cavity for ThomX, a prototype cavity for TTX2 was also designed.

We succeeded to store 400 kW power for the first time inside a high finesse (26,000) cavity, which demonstrated that a high finesse cavity can be used for Compton X-ray machine. However, we faced modal instabilities in our experiments which must be studied in order to reach 600 kW even 1 MW level. The future research work for ThomX and TTX2 cavities may be recommended as follows:

1. Modal instabilities were observed and this is a phenomenom that must be studied in details in the near future. In addition, we need to pay attention to the optimization of geometrical design of optical cavity for the sake of reducing modal instabilities.

2. We need to lower the coating absorption of cavity mirrors which is responsible of thermal effects. For ThomX and TTX2, the absorption of the coatings will be five times smaller and the thermal effect will be much reduced.

References

[1] Röntgen W C. Ueber eine neue art von strahlen. Annalen der Physik, 1898, 300(1):1–11.

[2] Karlsson E B. The nobel prize in physics. The Nobel Prize: The First 100 Years. 2001: 31–69.

[3] Nobel prizes for research with X-rays. http://www.ammrf.org.au/myscope/xrd/introduction/facts/prizes.php.

[4] Winick H. Synchrotron radiation sources: Past, present and future. Röntgen Centennial, X-rays in Natural and Life Sciences. World Scientific, 1997. 45–64.

[5] Bessonov E, Gorbunkov M, Kostryukov P, et al. Design study of compact laser-electron X-ray generator for material and life sciences applications. Journal of Instrumentation, 2009, 4(07):P07017.

[6] Cullity B D, Weymouth J W. Elements of X-ray diffraction. American Journal of Physics, 1957, 25(6):394–395.

[7] Honkimäki V, Sleight J, Suortti P. Characteristic X-ray flux from sealed Cr, Cu, Mo, Ag and W tubes. Journal of Applied Crystallography, 1990, 23(5):412–417.

[8] Sources et accélérateurs of SOLEIL. https://www.synchrotron-soleil.fr/fr/recherche/sources-et-accelerateurs.

[9] Advanced light source, BERKELEY LAB. https://als.lbl.gov/.

[10] Advanced photon source. https://www1.aps.anl.gov/.

[11] European synchrontron radiation facility. http://www.esrf.eu/.

[12] Sping 8. http://www.spring8.or.jp/en/.

[13] Gibson D J. A high-energy, ultrashort-pulse X-ray system for the dynamic study of heavy, dense materials. Technical report, Lawrence Livermore National Lab., Livermore, CA (US), 2004.

[14] Madey J M. Stimulated emission of bremsstrahlung in a periodic magnetic field. Journal of Applied Physics, 1971, 42(5):1906–1913.

[15] Deacon D A, Elias L, Madey J M, et al. First operation of a free-electron laser. Physical Review Letters, 1977, 38(16):892.

[16] Huang Z, Kim K J. Review of X-ray free-electron laser theory. Physical Review Special Topics-Accelerators and Beams, 2007, 10(3):034801.

[17] Tremaine A, Wang X, Babzien M, et al. Experimental characterization of nonlinear harmonic radiation from a visible self-amplified spontaneous emission free-electron laser at saturation. Physical review letters, 2002, 88(20):204801.

[18] Ayvazyan V, Baboi N, Bähr J, et al. First operation of a free-electron laser generating GW power radiation at 32 nm wavelength. The European Physical Journal D-Atomic, Molecular, Optical and Plasma Physics, 2006, 37(2):297–303.

[19] Ayvazyan V, Baboi N, Bohnet I, et al. Generation of GW radiation pulses from a VUV free-electron laser operating in the femtosecond regime. Physical review letters, 2002, 88(10):104802.

[20] Arthur J, et al. {Linac Coherent Light Source (LCLS)} conceptual design report. SLAC-R-593, 2002..

[21] Brinkmann R, Trines D, Schneider J, et al. TESLA XFEL: First stage of the X-ray laser laboratory. technical design report, supplement. Technical report, 2003.

[22] Tanaka T, Shintake T. Spring-8 compact SASE source conceptual design report. RIKEN Harima Institute: Hyogo, Japan, 2005..

[23] Brinkmann R. The European XFEL project. FEL, volume 6, 2006. 24.

[24] European cooperation in science and technology. http://www.cost.eu/COST_Actions/mpns/MP0601.

[25] Feenberg E, Primakoff H. Interaction of cosmic-ray primaries with sunlight and starlight. Physical Review, 1948, 73(5):449.

[26] Milburn R H. Electron scattering by an intense polarized photon field. Physical Review Letters, 1963, 10(3):75.

[27] Fiocco G, Thompson E. Thomson scattering of optical radiation from an electron beam. Physical Review Letters, 1963, 10(3):89.

[28] Jorda J, Burtin E, Cavata C, et al. A Fabry–Pérot cavity for Compton polarimetry. Nuclear Instruments and Methods in Physics Research Section A: Accelerators, Spectrometers, Detectors and Associated Equipment, 1998, 412(1):1–18.

[29] Asakawa E, Kamoshita J i, Sugamoto A, et al. Production of scalar Higgs and pseudoscalar Higgs in multi-Higgs doublet models at γ γ colliders. The European Physical Journal C-Particles and Fields, 2000, 14(2):335–345.

[30] Sakai H, Honda Y, Sasao N, et al. Measurement of an electron beam size with a laser wire beam profile monitor. Physical Review Special Topics-Accelerators and Beams, 2001, 4(2):022801.

[31] Moortgat-Pick G, Abe T, Alexander G, et al. Polarized positrons and electrons at the linear collider. Physics Reports, 2008, 460(4–5):131–243.

[32] Suortti P, Thomlinson W. Medical applications of synchrotron radiation. Physics in medicine and biology, 2003, 48(13):R1.

[33] Sprawls P. Physical principles of medical imaging. Aspen Publishers, 1987.

[34] 阿特伍德D, 张杰. 软x射线与极紫外辐射的原理和应用, 2003.

[35] Momose A. Phase-contrast X-ray imaging based on interferometry. Journal of synchrotron radiation, 2002, 9(3):136–142.

[36] Wilkins S, Gureyev T E, Gao D, et al. Phase-contrast imaging using polychromatic hard X-rays. Nature, 1996, 384(6607):335.

[37] Takeda T, Momose A, Wu J, et al. Vessel imaging by interferometric phase-contrast X-ray technique. Circulation, 2002, 105(14):1708–1712.

[38] Chapman D, Thomlinson W, Johnston R, et al. Diffraction enhanced X-ray imaging. Physics in medicine and biology, 1997, 42(11):2015.

[39] Wiebe S, Rhoades G, Wei Z, et al. Understanding refraction contrast using a comparison of absorption and refraction computed tomographic techniques. Journal of Instrumentation, 2013, 8(05):C05004.

[40] Fitzgerald R. Phase-sensitive X-ray imaging. Phys. Today, 2000, 53(7):23–26.

[41] Slatkin D, Spanne P, Dilmanian F, et al. Subacute neuropathological effects of microplanar beams of X-rays from a synchrotron wiggler. Proceedings of the National Academy of Sciences, 1995, 92(19):8783–8787.

[42] Laissue J A, Lyubimova N, Wagner H P, et al. Microbeam radiation therapy. SPIE's International Symposium on Optical Science, Engineering, and Instrumentation. International Society for Optics and Photonics, 1999. 38–45.

[43] Laissue J A, Blattmann H, Di Michiel M, et al. Weanling piglet cerebellum: a surrogate for tolerance to MRT (microbeam radiation therapy) in pediatric neuro-oncology. International Symposium on Optical Science and Technology. International Society for Optics and Photonics, 2001. 65–73.

[44] Choi G H, Seo S J, Kim K H, et al. Photon activated therapy (PAT) using monochromatic synchrotron X-rays and iron oxide nanoparticles in a mouse tumor model: feasibility study of PAT for the treatment of superficial malignancy. Radiation Oncology, 2012, 7(1):184.

[45] Rose J H, Norman A, Ingram M, et al. First radiotherapy of human metastatic brain tumors delivered by a computerized tomography scanner (CTRx). International Journal of Radiation Oncology* Biology* Physics, 1999, 45(5):1127–1132.

[46] O Klein Y N. Über die streuung von strahlung durch freie elektronen nach der neuen relativistischen quantendynamik von dirac. Zeitschrift für Physik, 1929, 52(11-12):853.

[47] Suzuki T. General formulas of luminosity for various types of colliding beam machines. Technical report, 1976.

[48] Matone G, Picozza P, Prosperi D, et al. A monochromatic and polarized photon beam for photonuclear reactions. the ladon project at Frascati. Photonuclear Reactions II. Springer, 1977: 149–164.

[49] Federici L, Giordano G, Matone G, et al. Backward Compton scattering of laser light against high-energy electrons: the LADON photon beam at Frascati. Il Nuovo Cimento B (1971-1996), 1980, 59(2):247–256.

[50] Chaikovska I, Cassou K, Chiche R, et al. High flux circularly polarized gamma beam factory: coupling a Fabry-Perot optical cavity with an electron storage ring. Scientific reports, 2016, 6:36569.

[51] Akagi T, Araki S, Bonis J, et al. Production of gamma rays by pulsed laser beam compton scattering off GeV-electrons using a non-planar four-mirror optical cavity. Journal of Instrumentation, 2012, 7(01):P01021.

[52] Favier P. Etude et conception d'une cavité Fabry-Perot de haute finesse pour la source compacte de rayons X ThomX[D]. Paris Saclay, 2017.

[53] Eggl E, Dierolf M, Achterhold K, et al. The munich compact light source: initial performance measures. Journal of synchrotron radiation, 2016, 23(5):1137–1142.

[54] Tang C, Huang W, Li R, et al. Tsinghua Thomson scattering X-ray source. Nuclear Instruments and Methods in Physics Research Section A: Accelerators, Spectrometers, Detectors and Associated Equipment, 2009, 608(1):S70–S74.

[55] Li-Xm Y, Ying-Chao D, Qiang D, et al. TW laser system for Thomson scattering X-ray light source at Tsinghua University. Chinese physics C, 2009, 33(S2):154.

[56] Maroli C, Petrillo V, Tomassini P, et al. Nonlinear effects in Thomson backscattering. Physical Review Special Topics-Accelerators and Beams, 2013, 16(3):030706.

[57] Variola A, Haissinski J, Loulergue A, et al. Thomx technical design report. 2014..

[58] Sources et accélérateurs of SOLEIL. http://www.synchrotron-soleil.fr/SourceAccelerateur/Brillance.

[59] Teets R, Eckstein J, Hänsch T W. Coherent two-photon excitation by multiple light pulses. Physical Review Letters, 1977, 38(14):760–764.

[60] Okeefe A, Deacon D A G. Cavity ring-down optical spectrometer for absorption measurements using pulsed laser sources. Review of Scientific Instruments, 1988, 59(12):2544–2551.

[61] Persaud M A, Tolchard J M, Ferguson A I. Efficient generation of picosecond pulses at 243 nm. IEEE Journal of Quantum Electronics, 1990, 26(7):1253–1258.

[62] Crosson E R, Haar P, Marcus G A, et al. Pulse-stacked cavity ring-down spectroscopy. Review of Scientific Instruments, 1999, 70(1):4–10.

[63] Thorpe M J, Ye J. Cavity-enhanced direct frequency comb spectroscopy. Applied Physics B, 2008, 91(3-4):397–414.

[64] Gohle C, Udem T, Rauschenberger J, et al. A frequency comb in the extreme ultraviolet. Nature, 2005, 436(7048):234–7.

[65] Ozawa A, Vernaleken A, Schneider W, et al. Non-collinear high harmonic generation: a promising outcoupling method for cavity-assisted XUV generation. Optics Express, 2008, 16(9):6233.

[66] Drever R, Hough J, Munley A, et al. Optical cavity laser interferometers for gravitational wave detection. Laser Spectroscopy V. Springer, 1981: 33–40.

[67] Webster S A, Oxborrow M, Gill P. Subhertz-linewidth Nd: YAG laser. Optics Letters, 2004, 29(13):1497–1499.

[68] Notcutt M, Ma L S, Ye J, et al. Simple and compact 1-Hz laser system via an improved mounting configuration of a reference cavity. Optics letters, 2005, 30(14):1815–1817.

[69] Sakai H, Honda Y, Sasao N, et al. Performance studies of a laser wire beam profile monitor. Japanese Journal of Applied Physics, 2002, 41(41):6398–6408.

[70] Carter W H. Spot size and divergence for Hermite Gaussian beams of any order. Applied optics, 1980, 19(7):1027–1029.

[71] Novotny L, Sánchez E J, Xie X S. Near-field optical imaging using metal tips illuminated by higher-order Hermite–Gaussian beams. Ultramicroscopy, 1998, 71(1):21–29.

[72] Siegman A E. Lasers university science books. Mill Valley, CA, 1986, 37:462–466.

[73] Cundiff S T, Ye J. Colloquium: Femtosecond optical frequency combs. Reviews of Modern Physics, 2003, 75(1):325.

[74] Ye J, Cundiff S T. Femtosecond optical frequency comb: principle, operation and applications. Springer Science & Business Media, 2005.

[75] Udem T, Reichert J, Holzwarth R, et al. Accurate measurement of large optical frequency differences with a mode-locked laser. Optics letters, 1999, 24(13):881–883.

[76] Udem T, Holzwarth R, Hänsch T W. Optical frequency metrology. Nature, 2002, 416(6877):233–237.

[77] Goodman J W. Introduction to Fourier optics. Roberts and Company Publishers, 2005.

[78] Chiche R, Jehanno D, Soskov V, et al. Les cavités Fabry-Perot en mode pulsé et leurs récentes applications. 2009..

[79] Kogelnik H, Li T. Laser beams and resonators. Proceedings of the IEEE, 1966, 54(10):1312–1329.

[80] Petersen J, Luiten A. Short pulses in optical resonators. Optics express, 2003, 11(22):2975–2981.

[81] Börzsönyi A, Chiche R, Cormier E, et al. External cavity enhancement of picosecond pulses with 28,000 cavity finesse. Applied optics, 2013, 52(34):8376–8380.

[82] Jojart P, Börzsönyi Á, Soskov V, et al. Carrier-envelope phase drift measurement of picosecond pulses by an all-linear-optical means. Optics letters, 2014, 39(20):5913–5916.

[83] Mcmanus J B, Kebabian P L, Zahniser M S. Astigmatic mirror multipass absorption cells for long-path-length spectroscopy. Applied Optics, 1995, 34(18):3336–48.

[84] McManus J B, Nelson D D, Shorter J H, et al. A high precision pulsed quantum cascade laser spectrometer for measurements of stable isotopes of carbon dioxide. Journal of Modern Optics, 2005, 52(16):2309–2321.

[85] Blows J, Forbes G. Mode characteristics of twisted resonators composed of two cylindrical mirrors. Optics Express, 1998, 2(5):184–90.

[86] Kogelnik H, Arnaud J A. Gaussian light beams with general astigmatism. Applied Optics, 1969, 8(8):1687.

[87] Habraken S J M, Nienhuis G. Modes of a twisted optical cavity. Physical Review A, 2007, 75(75):723–727.

[88] Zomer F, Fedala Y, Pavloff N, et al. Polarization induced instabilities in external four-mirror Fabry-Perot cavities. Applied Optics, 2009, 48(35):6651–61.

[89] Bonis J, Chiche R, Cizeron R, et al. Non-planar four-mirror optical cavity for high intensity gamma ray flux production by pulsed laser beam Compton scattering off GeV-electrons. Journal of Instrumentation, 2012, 7(1):30–32.

[90] Petrillo V, Dattoli G, Drebot I, et al. Compton scattered X-gamma rays with orbital momentum. Physical Review Letters, 2016, 117(12):123903.

[91] Labaye F. Amplification passive d'un laser à fibre optique dans une cavité Fabry-Perot : application à la production de rayonnement gamma par diffusion Compton inverse[D]. Université Paris-sud, 2012.

[92] Arnaud J A. Nonorthogonal optical waveguides and resonators. Bell System Technical Journal, 1970, 49(9):2311–2348.

[93] Janner D, Galzerano G, Valle G D, et al. Slow light in periodic superstructure Bragg gratings. Physical Review E Statistical Nonlinear and Soft Matter Physics, 2005, 72(2):056605.

[94] Habraken S J M, Nienhuis G. Modes of a twisted optical cavity. Physical Review A, 2007, 75(75):723–727.

[95] Visser J, Nienhuis G. Orbital angular momentum of general astigmatic modes. Physical Review A, 2004, 70(1):235–238.

[96] Kiselev A P, Plachenov A B, Chamorro-Posada P. Nonparaxial wave beams and packets with general astigmatism. Phys. Rev. A, 2012, 85:043835.

[97] Liu X, Cassou K, Dupraz K, et al. S-shaped non-paraxial corrections to general astigmatic beams. Journal of the Optical Society of America A Optics Image Science and Vision, 2017, 34(4):576.

[98] Variola A, Martens A, Zomer F, et al. Direct electron acceleration with tightly focused TM0,1 beams: boundary conditions and non-paraxial corrections. Optics Letters, 2014, 39(4):981–984.

[99] Lax M, Louisell W H, McKnight W B. From maxwell to paraxial wave optics. Phys. Rev. A, 1975, 11:1365–1370.

[100] Davis L W. Theory of electromagnetic beams. Phys. Rev. A, 1979, 19:1177–1179.

[101] Couture M, Belanger P A. From gaussian beam to complex-source-point spherical wave. Phys. Rev. A, 1981, 24:355–359.

[102] Marceau V, Varin C, Piché M. Validity of the paraxial approximation for electron acceleration with radially polarized laser beams. Optics Letters, 2013, 38(6):821–3.

[103] April A. Ultrashort, strongly focused laser pulses in free space. INTECH Open Access Publisher, 2010.

[104] Patsakos G, Davis L W. TM and TE electromagnetic beams in free space. Optics Letters, 1981, 6(1):22–3.

[105] Wong L J, Kärtner F X. Direct acceleration of an electron in infinite vacuum by a pulsed radially-polarized laser beam. Optics Express, 2010, 18(24):25035–51.

[106] Visser J, Nienhuis G. Orbital angular momentum of general astigmatic modes. Phys. Rev. A, 2004, 70:013809.

[107] Wünsche A. Transition from the paraxial approximation to exact solutions of the wave equation and application to gaussian beams. Journal of the Optical Society of America A, 1992, 9(9):765–774.

[108] Courtois J, Mohamed A, Romanini D. Degenerate astigmatic cavities. Phys. Rev. A, 2013, 88:043844.

[109] Mondin L. Stabilisation de fréquence de laser Nd: YAG pour applications spatiales[D]. Université Nice Sophia Antipolis, 2005.

[110] Drever R W P, Hall J L, Kowalski F V, et al. Laser phase and frequency stabilization using an optical resonator. Applied Physics B, 1983, 31(2):97–105.

[111] Black E D. An introduction to Pound–Drever–Hall laser frequency stabilization. American Journal of Physics, 2001, 69(1):79–87.

[112] Shaddock D A, Gray M B, Mcclelland D E. Frequency locking a laser to an optical cavity by use of spatial mode interference. Optics Letters, 1999, 24(21):1499–501.

[113] Shaddock D, et al. Advanced interferometry for gravitational wave detection. 2000..

[114] You Y. Pulsed laser injected enhancement cavity for laser-electron interaction. Paris, 2014..

[115] Hansch T W, Couillaud B. Laser frequency stabilization by polarization spectroscopy of a reflecting reference cavity ☆. Optics Communications, 1980, 35(3):441–444.

[116] Libson A, Brown N, Buikema A, et al. Simple method for locking birefringent resonators. Optics Express, 2015, 23(3):3809–17.

[117] Miller J, Evans M. Length control of an optical resonator using second-order transverse modes. Optics Letters, 2014, 39(8):2495–8.

[118] Honda Y, Shimizu H, Fukuda M, et al. Stabilization of a non-planar optical cavity using its polarization property. Optics Communications, 2009, 282(15):3108–3112.

[119] Liu X, Cassou K, Chiche R, et al. Laser frequency stabilization using folded cavity and mirror reflectivity tuning. Optics Communications, 2016, 369:84–88.

[120] Macleod H A. Thin-film optical filters, Chaper 2. CRC Press, 2010.

[121] Bielsa F, Dupays A, Fouché M, et al. Birefringence of interferential mirrors at normal incidence. Applied Physics B, 2009, 97(2):457–463.

[122] Born M, Wolf E. Principles of optics: electromagnetic theory of propagation, interference and diffraction of light. Cambridge university press, 1999.

[123] Asenbaum P, Arndt M. Cavity stabilization using the weak intrinsic birefringence of dielectric mirrors. Optics letters, 2011, 36(19):3720–3722.

[124] Brandi F, Della Valle F, De Riva A, et al. Measurement of the phase anisotropy of very high reflectivity interferential mirrors. Applied Physics B: Lasers and Optics, 1997, 65(3):351–355.

[125] Akagi T, Kosuge A, Araki S, et al. Narrow-band photon beam via laser Compton scattering in an energy recovery linac. Physical Review Accelerators and Beams, 2016, 19(11):114701.

[126] Winkler W, Danzmann K, Rüdiger A, et al. Heating by optical absorption and the performance of interferometric gravitational-wave detectors. Physical Review A, 1991, 44(11):7022.

[127] Hello P, Vinet J Y. Analytical models of thermal aberrations in massive mirrors heated by high power laser beams. Journal de Physique, 1990, 51(12):1267–1282.

[128] Hello P, Vinet J Y. Analytical models of transient thermoelastic deformations of mirrors heated by high power CW laser beams. Journal de Physique, 1990, 51(20):2243–2261.

[129] Corning products. https://www.corning.com/in/en/products/advanced-optics/product-materials/semiconductor-laser-optic-components/ultra-low-expansion-glass.html.

[130] Feng S, Winful H G. Physical origin of the Gouy phase shift. Optics letters, 2001, 26(8):485–487.

[131] Kaddour Z D, Taleb A, Ait-Ameur K, et al. Revisiting Gouy phase. Optics Communications, 2007, 280(2):256–263.

[132] Erden M F, Ozaktas H M. Accumulated Gouy phase shift in Gaussian beam propagation through first-order optical systems. JOSA A, 1997, 14(9):2190–2194.

[133] You Y, Urakawa J, Rawankar A, et al. Measurement of beam waist for an optical cavity based on Gouy phase. Nuclear Instruments and Methods in Physics Research Section A: Accelerators, Spectrometers, Detectors and Associated Equipment, 2012, 694:6–10.

[134] CELIA. CELIA laboratory. http://www.celia.u-bordeaux1.fr/?lang=fr.

[135] Thorlabs. DET36A photodiode. https://www.thorlabs.com/thorproduct.cfm?partnumber=DET36A.

[136] Alphanov. Centre technologique optique et lasers. http://www.alphanov.com/.

[137] Wikipedia. M squared. https://en.wikipedia.org/wiki/M_squared.

[138] Optic I. HASO 3 FAST. https://www.imagine-optic.com/product/haso3-fast/.

[139] Rempe G, Lalezari R, Thompson R, et al. Measurement of ultralow losses in an optical interferometer. Optics letters, 1992, 17(5):363–365.

[140] An K, Yang C, Dasari R R, et al. Cavity ring-down technique and its application to the measurement of ultraslow velocities. Optics letters, 1995, 20(9):1068–1070.

[141] Locke C, Stuart D, Ivanov E, et al. A simple technique for accurate and complete characterisation of a Fabry-Perot cavity. Optics express, 2009, 17(24):21935–21943.

[142] Poirson J, Bretenaker F, Vallet M, et al. Analytical and experimental study of ringing effects in a Fabry–Perot cavity: Application to the measurement of high finesses. JOSA B, 1997, 14(11):2811–2817.

[143] Matone L, Barsuglia M, Bondu F, et al. Finesse and mirror speed measurement for a suspended Fabry–Perot cavity using the ringing effect. Physics Letters A, 2000, 271(5):314–318.

[144] Polymer F C. First contact cleaner. https://www.photoniccleaning.com/.

[145] Benedikter J, Hümmer T, Mader M, et al. Transverse-mode coupling and diffraction loss in tunable Fabry–Pérot microcavities. New Journal of Physics, 2015, 17(5):053051.

[146] Wang H, Dovale-Álvarez M, Collins C, et al. Feasibility of near-unstable cavities for future gravitational wave detectors. Physical Review D, 2018, 97(2):022001.

[147] Bullington A L, Lantz B T, Fejer M M, et al. Modal frequency degeneracy in thermally loaded optical resonators. Applied optics, 2008, 47(15):2840–2851.

[148] Bond C, Fulda P, Carbone L, et al. Higher order Laguerre-Gauss mode degeneracy in realistic, high finesse cavities. Physical Review D, 2011, 84(10):102002.

[149] Vajente G. In situ correction of mirror surface to reduce round-trip losses in Fabry–Perot cavities. Applied optics, 2014, 53(7):1459–1465.

[150] Vajente G, Day R. Adaptive optics sensing and control technique to optimize the resonance of the Laguerre-Gauss 33 mode in Fabry-Perot cavities. Physical Review D, 2013, 87(12):122005.

[151] Carstens H, Lilienfein N, Holzberger S, et al. Cavity-enhanced 196 kW average-power infrared pulses. Mid-Infrared Coherent Sources. Optical Society of America, 2013. JTh5A–3.

[152] Newport. zero-drift mirror mounts. https://www.newport.com.cn/f/zero-drift-mirror-mounts.

Acknowledgement

Time flies. Five-year doctoral career went in a flash. I still remembered the exciting moment when I received the admission letter of Tsinghua University five years ago. I was very happy because of realizing my "Tsinghua" dream.

I was lucky enough to meet my supervisor Pr. TANG Chuanxiang, a gentle and cultivated scholar. I take this opportunity to express my sincere thanks and pay high respect to Pr. Tang. He taught me how to do research patiently, educated me in how to behave, and was always encouraging me when I hesitated to move forward. I wish I could be somebody like Pr.Tang.

I also thank my supervisor Pr. Fabian ZOMER in University of Paris-Saclay. I was fortunate that I had an opportunity to study for two years at LAL. I was deeply infected by his passionate love and serious attitude towards scientific research and his personal charisma. He taught me the basic laser knowledge patiently, led me how to do research independently, and helped me modify my poor English writing. I will never forget the precious time in France.

Throughout my time at Accelerator Lab of Tsinghua, I recieved too many fruitful help. I thank Pr. HUANG Wenhui, Pr. YAN Lixin, Pr. CHEN Huaibi, Pr. LU Wei, Pr. DU Yingchao, Dr. YANG Jin, Dr YOU Yan, Dr. WANG Dan, Dr XU Yilun, Miss WANG Huan and all the teachers and classmates for their selfless help and deep friendship over the past five years.

During the period at LAL of University of Paris-Saclay, I am deeply grateful to my colleges Pr. Kevin CASSOU, Pr. Aurelien MARTENS, and Pr. Kevin DUPRAZ in sharing their knowledge. In addition, I acknowledge the experimental aid of Engineer Ronic CHICHE, Dr. Viktor SOSKOV and Dr. Pierre FAVIER with whom I worked on S-Box for two years. Besides, many thanks for my classmates Themis WILLIAMS and Cheikh NDIAYE who offered me lots of help in research and life. I will never forget the happiest two-year time and the impressive experience in France.

At last, I want to thank my parents and my two sisters. You keep me going forward and I love you all.

Personal Statement

本人郑重声明：所呈交的学位论文，是本人在导师指导下，独立进行研究工作所取得的成果。尽我所知，除文中已经注明引用的内容外，本学位论文的研究成果不包含任何他人享有著作权的内容。对本论文所涉及的研究工作做出贡献的其他个人和集体，均已在文中以明确方式标明。

The author asseverates: this thesis was prepared solely by myself under instruction of my thesis advisor. To my knowledge, except for documents cited in the thesis, the research results do not contain any achievements of any others who have claimed copyrights. To contributions made by relevant individuals and organizations in the completion of the thesis, I have clearly acknowledged all their efforts.

签　名/ Signature：_____ 日　期/ Date：_____

Resume and Publication List

个人简历

1990年3月26日出生于山西省代县。

2009年9月考入四川大学物理学院核工程与核技术专业，后被选拔至吴玉章荣誉学院学习， 2013年7月本科毕业并获得工学学士学位。

2013年9月免试进入清华大学工程物理系攻读核科学与技术博士学位至今。

2015年3月至2017年6月获国家留学基金委和法国政府Eiffel奖学金“联合培养博士生”项目资助，赴巴黎第十一大学物理系，联合指导导师为Fabian ZOMER教授。

I was born in Daixian, Shanxi Province, in March, 1990.

I entered School of Physics, Sichuan University in September, 2009, majored in Nuclear Engineering and Nuclear Technology, and was selected to Wuyuzhang Honor college of Sichuan University. I got the bacholer degree of engineering in July, 2013.

In September, 2013, I passed into Department of Enegineering Physics, Tsinghua University, under the supervision of Professor TANG Chuanxiang.

In March, 2015, I got the Eiffel Scholarship and CSC funding, and studied in University of Paris Saclay, under the supervision of Professor Fabian ZOMER.

Publications List

[1] **LIU, X.**, CASSOU, K., CHICHE, R., et al. Laser frequency stabilization using folded cavity and mirror reflectivity tuning. Optics Communications, 2016, vol. 369, p. 84-88. (SCI收录, WOS检索号:000372154400013)

[2] **LIU, X.**, CASSOU, K., DUPRAZ, K., et al. S-shaped non-paraxial corrections to general astigmatic beams. JOSA A, 2017, vol. 34, no 4, p. 576-582. (SCI收录, WOS检索号:000399321700014)

[3] **LIU, X.**, YAN,L.X., HUANG W.H., et al. Optical cavity R & D for laser-electron interaction applications. IPAC'18, Canada, 2018

[4] **LIU, X.**, HUANG, W., YAN, L., TANG, C., YOU, Y. Mechanical Stablitity Analysis on Optical Cavity Used for TTX. 2015, WEPH30.

[5] WILLIAMS, T., N'DIAYE, C., BRETON, D., CASSOU, K., FAVIER, P., JE-

HANNO. D., KUBYTSKYI, V., **LIU, X.**, et al. Operation of a fast diamond γ -ray detector at the HI γ S facility. Nuclear Instruments and Methods in Physics Research Section A: Accelerators, Spectrometers, Detectors and Associated Equipment, 2016, vol. 830, p. 391-396.

[6] FAVIER, Pierre, DUPRAZ, Kevin, CASSOU, Kevin, **LIU, Xing**, et al. Short pulse laser beam beyond paraxial approximation. JOSA A, 2017, vol. 34, no 8, p. 1351-1359.

[7] Favier, Pierre, Cassou, Kevin, Chiche, Ronic, Jehanno, Didier, **Liu, Xing**, et al. "Development of an optical resonator for X-ray production." Progress in Electromagnetic Research Symposium (PIERS). IEEE, 2016.

université PARIS-SACLAY | ÉCOLE DOCTORALE PHENIICS

Doctorant : LIU Xing

Titre : Développement d'une cavité Fabry-Pérot à haute puissance moyenne pour des expériences de diffusion Compton

Résumé :

L'imagerie effectuée avec des rayons X est largement utilisée de nos jours dans de nombreuses disciplines telles que la physique du solide, les sciences du vivant et la médecine. Les sources de rayons X basées sur la diffusion Thomson d'un faisceau laser par des paquets d'électrons permettent d'obtenir des faisceaux de bonnes qualités pour un faible coût et un faible encombrement. Plusieurs instituts de recherche académiques se sont récemment lancés dans la construction de telles sources qui sont constituées d'un anneau des stockage d'électrons et d'un résonateur optique. Le résonateur optique permet de stocker des impulsions laser focalisées au point d'interaction laser-électron à des fréquences de plusieurs dizaines de méga Hertz. Des flux de rayons X dépassants 10^{11} ph/s peuvent ainsi être obtenus.

Dans ce travail de thèse un modèle de stockage d'impulsion a été développé. Ce modèle prend en compte les effets de la phase CEP (carrier-envelope phase) et des décalages temporels permettant d'obtenir des résonances secondaires. Ces résonances sont observées couramment et

nous avons pu calculer les gains et finesses équivalentes. Nous avons aussi calculé les corrections non-paraxiales des modes propres d'une cavité non-planaires. Nous avons résolu les équations perturbatives de Lax pour des faisceaux gaussiens elliptiques généralisés. Nous avons pu ainsi décrire qualitativement des résultats expérimentaux obtenus avec une cavité non-planaire constituée de quatre miroirs. Nous avons aussi modélisé l'effet des déformations thermoélastiques des miroirs de cavité en utilisant le modèle simplifié de Winkler.

Sur le plan expérimental, nous avons effectué des études sur le résonateur optique prototype du projet EQUIPEX THOMX. Nous avons tout d'abord proposé une nouvelle méthode d'asservissement laser-cavité basée sur l'utilisation d'une possible différence de phase induite par la réflexion des ondes s et p. Comparée à la méthode de Pound-Drever-Hall, notre méthode ne nécessite pas de modulation et démodulation de fréquence. Nous avons effectué les calculs de modélisation ainsi qu'une démonstration expérimentale. En parallèle, nous avons effectué des expériences de stockage de puissance dans la cavité prototype de finesse 26000 et nous avons obtenu une puissance moyenne de 383 kW correspondant à un gain de 10000. Nous avons atteint un niveau de puissance pour laquelle des instabilités modales induites par les déformations thermoélastiques des miroirs de notre cavité deviennent dominantes et perturbent l'asservissement laser-cavité.

Une machine à rayon X Thomson, TTX, existe aussi à l'université de Tsinghua. Celle-ci est basée sur un accélérateur linéaire et une source laser femtoseconde terawatt. Un nouveau projet basé sur un anneau de stockage compact d'électrons, TTX2, voit actuellement le jour à l'université de Tsinghua. Nous présentons le design du système optique de ce futur projet.

université PARIS-SACLAY | ÉCOLE DOCTORALE PHENIICS

Titre : Développement d'une cavité Fabry-Pérot à haute puissance moyenne pour des expériences de diffusion Compton

Mots clés : Cavité optique; Verrouillage de polarisation; Diffusion Thomson; Résonateur à puissance moyenne élevée; Effet thermique

Résumé : L'imagerie effectuée avec des rayons X est largement utilisée de nos jours dans de nombreuses disciplines telles que la physique du solide, les sciences du vivant et la médecine. Les sources de rayons X basées sur la diffusion Thomson d'un faisceau laser par des paquets d'électrons permettent d'obtenir des faisceaux de bonnes qualités pour un faible coût et un faible encombrement. Plusieurs instituts de recherche académiques se sont récemment lancés dans la construction de telles sources qui sont constituées d'un anneau des stockage d'électrons et d'un résonateur optique. Le résonateur optique permet de stocker des impulsions laser focalisées au point d'interaction laser-électron à des fréquences de plusieurs dizaines de méga Hertz. Des flux de rayons X dépassants 10^{11} ph/s peuvent ainsi être obtenus.

Dans ce travail de thèse un modèle de stockage d'impulsion a été développé. Ce modèle prend en compte les effets de la phase CEP (carrier-envelope phase) et des décalages temporels permettant d'obtenir des résonances secondaires. Ces résonances sont observées couramment et nous avons pu calculer les gains et finesses équivalentes. Nous avons aussi calculé les corrections non-paraxiales des modes propres d'une cavité non-planaires. Nous avons résolu les équations perturbatives de Lax pour des faisceaux gaussiens elliptiques généralisés. Nous avons pu ainsi décrire qualitativement des résultats expérimentaux obtenus avec une cavité non-planaire constituée de quatre miroirs. Nous avons aussi modélisé l'effet des déformations thermoélastiques des miroirs de cavité en utilisant le modèle simplifié de Winkler.

Sur le plan expérimental, nous avons effectué des études sur le résonateur optique prototype du projet EQUIPEX THOMX. Nous avons tout d'abord proposé une nouvelle méthode d'asservissement laser-cavité basée sur l'utilisation d'une possible différence de phase induite par la réflexion des ondes s et p. Comparée à la méthode de Pound-Drever-Hall, notre méthode ne nécessite pas de modulation et démodulation de fréquence. Nous avons effectué les calculs de modélisation ainsi qu'une démonstration expérimentale. En parallèle, nous avons effectué des expériences de stockage de puissance dans la cavité prototype de finesse 26000 et nous avons obtenu une puissance moyenne de 383 kW correspondant à un gain de 10000. Nous avons atteint un niveau de puissance pour laquelle des instabilités modales induites par les déformations thermoélastiques des miroirs de notre cavité deviennent dominantes et perturbent l'asservissement laser-cavité.

Une machine à rayon X Thomson, TTX, existe aussi à l'université de Tsinghua. Celle-ci est basée sur un accélérateur linéaire et une source laser femtoseconde terawatt. Un nouveau projet basé sur un anneau de stockage compact d'électrons, TTX2, voit actuellement le jour à l'université de Tsinghua. Nous présentons le design du système optique de ce futur projet.

Université Paris-Saclay
Espace Technologique / Immeuble Discovery
Route de l'Orme aux Merisiers RD 128 / 91190 Saint-Aubin, France

université PARIS-SACLAY | ÉCOLE DOCTORALE PHENIICS

Title : R & D of a High-Average-Power Fabry-Pérot Resonator for Thomson Scattering Experiments

Keywords : Optical cavity ; Polarization lock; Thomson scattering; High-average-power resonator; Thermal effect

Abstract : At present, X-rays imaging is widely applied in solid-state physics, in the life sciences, in medical applications and in other disciplines. An X-ray source based on laser-electron interaction, that is, a Thomson scattering X-ray source, can be used to produce high-quality X-rays at a low cost and small footprint. The construction of compact laser electron sources, consisting of an electron storage ring and an optical enhancement cavity, has recently attracted the interest of many institutions. The optical enhancement cavity is mainly used to amplify the injected power, circulate the pulses at a high repetition frequency (tens of megahertz) and produce a beam with a small waist at the interaction point. When introduced into the electron storage ring, the laser pulses produced in the high-average-power cavity scatter off high-energy electrons at a high repetition frequency. Thus, a high X-ray flux of more than 10^{11} ph/s can be obtained.

In order to study the physical process inside a high-power resonator a model has been developed. As a first step, we establish a precise transient model of the laser pulse stacking technique considering the CEP (carrier-envelope phase) effect and time detuning. The results of this model in the time and frequency domains match very well. A cavity with a given finesse and no detuning has a narrower linewidth than a detuned cavity with a higher finesse if both cavities have the same gain; consequently, it is easier to lock a laser to the latter cavity. Next, for the first time, we derived the non-paraxial corrections for general astigmatic beams so as to explain the S-shaped cavity mode observed in a non-planar four-mirror cavity. We solved Lax perturbation series of the wave equation for general elliptic Gaussian beams and S-shaped beam modes appear as the beam propagates away from the cavity symmetry point. This feature agrees qualitatively with observations made on a highly divergent non-planar four-mirror cavity. In addition, we study the thermal effect by using Winkler's deformation model. The cavity gain is very sensitive to the mirror deformation in open loop. A strong feedback and ultra-low expansion mirrors are indispensable to reach a high power stored in the cavity.

Several significant experiments were performed on a prototype cavity of the EQUIPEX project THOMX. Firstly, we proposed a new frequency stabilization method based on the polarization of a folded cavity and tuning of the cavity mirror reflectivity. Sufficient s- and p-wave phase detuning can be obtained by special design of the cavity mirrors' coatings, which give rise to an error signal that can be used for locking. Compared to the traditional PDH method, this technique is simpler without need for frequency modulation and demodulation. Theoretical calculations and experimental results demonstrate the feasibility of the proposed method. Meanwhile, high-power experiments on the prototype cavity for ThomX were demonstrated. A cavity finesse of approximately 26,000 is measured using four different methods, and the deposition of dust on the cavity mirrors is found to have an enormous effect on the finesse. We achieved a stable average power as high as 383 kW with a cavity gain of 10,000. In addition, modal instabilities which limits this power were observed. We believe that this effect originates from cavity modal frequency degeneracy induced by thermal effect.

Tsinghua University hosts a compact, low-repetition-frequency X-ray source known as TTX, which is based on a linac system and a terawatt femtosecond laser system. The next step is to upgrade TTX to a high-repetition-frequency X-ray machine called TTX2, consisting of an optical cavity and an electron storage ring. We present the complete design of a prototype optical cavity for TTX2.

Université Paris-Saclay
Espace Technologique / Immeuble Discovery
Route de l'Orme aux Merisiers RD 128 / 91190 Saint-Aubin, France